MINISTRY OF EDUCATION AND SCIENCE OF UKRAINE
VASYL' STUS DONETSK NATIONAL UNIVERSITY
KYIV ACADEMIC UNIVERSITY

NOVEL FRONTIERS IN MATERIALS SCIENCE: INNOVATIVE COMPONENTS FOR NEXT-GENERATION SUPERCONDUCTOR TECHNOLOGIES

Monograph

Mikhail Belogolovskii, *Editor*

Vinnytsia
Vasyl' Stus Donetsk National University
2023

*Рекомендовано до друку Вченою радою ДонНУ імені Василя Стуса
(протокол № 1 від 02.12.2022 р.)*

Рецензенти:

О. Л. Касаткін, д-р фіз.-мат. наук, провідний науковий співробітник Інституту металофізики імені Г. В. Курдюмова Національної академії наук України, Київ;

В. Г. Крижановський, д-р техн. наук, проф., професор кафедри інформаційних технологій Донецького національного університету імені Василя Стуса, Вінниця;

В. І. Шнирков, д-р фіз.-мат. наук, проф., старший науковий співробітник ДНУ «Київський академічний університет», Київ.

Визнаючи зростаючу важливість матеріалознавства для майбутніх шляхів створення нових пристроїв, два українських ЗВО, Донецький національний університет імені Василя Стуса та Київський академічний університет, ініціювали серію щорічних збірників оглядів та оригінальних статей, які мають відображати сучасний стан розуміння та моніторингу властивостей деяких важливих класів матеріалів. Ці монографії охоплюватимуть повний спектр відповідних досліджень, включно з фундаментальними принципами, теоретичними та експериментальними відкриттями, розробкою та застосуванням нових компонентів для реалізації пристроїв наступного покоління. Метою цієї монографії є представлення концепцій, теоретичних і практичних аспектів щодо нових компонентів, важливих для прогресу надпровідної електроніки, зокрема, аморфних і високотемпературних надпровідників і гібридних композитів, утворених матеріалами з різним електронним упорядкуванням. Обговорюються як оригінальні результати авторів, так і літературні дані, що дає змогу з'ясувати ситуацію у розглянутих галузях матеріалознавства.

Монографія призначена для співробітників, які працюють в галузі фізики та хімії твердих тіл, аспірантів і магістрантів фізичних факультетів університетів та науково-дослідних інститутів.

*Recommended for publication by the Academic Council
of the Vasyl' Stus Donetsk National University
(protocol on December 02, 2022, No. 1)*

N 89   Novel frontiers in materials science: Innovative components for next-generation superconductor technologies, monograph. 2nd edition / under the general editorship of Professor M. O. Belogolovskii. Vinnytsia: Vasyl' Stus DonNU, 2023. 158 p.

Recognizing the increasing importance of materials science in future device technologies, two Ukrainian universities, Vasyl' Stus Donetsk National University and Kyiv Academic University initiated a series of annual collections of reviews and original papers reflecting the state of the art in understanding and monitoring the properties of some important materials classes. The monographs will cover a complete spectrum of related research, including fundamental principles, theoretical and experimental breakthroughs, design and applications of novel components for next-generation hardware. The goal of this monograph is to present the concepts, theoretical and practical aspects of the components important for the superconductor electronics progress, in particular, amorphous and high-temperature superconductors and hybrid composites formed by materials with different electronic orderings. Both the original results obtained by the authors and the literature data are discussed, which makes it possible to obtain quite a complete picture of the state of affairs in the discussed areas of materials science.

For researchers working in the field of solid-state physics, PhD and master's students at physical faculties of universities and academic institutions.

PREFACE

Functional materials are generally characterized as those that themselves have specially focused natural properties and functions as magnetism, super-conductivity, ferroelectricity, piezoelectricity, or energy storage. Their innovation is a multi-stage process of transforming ideas into new / improved products, service or processes. Today, innovative functional materials that underlie many applications are critical for information and communication technology, healthcare, energy production and storage, transportation, defense and civil security, consumer goods, *etc*. Unlike many materials that are used in large quantities as, for example, building or packaging ones, the value of most innovative functional materials lies in their enabling capabilities. Their economic impact comes from the utility of the devices and systems based on them, rather than an economic value of the materials themselves. Vasyl' Stus Donetsk National University and Kyiv Academic University have decided to start a joint publication of a series of collective monographs under a common title *Frontiers in innovative functional materials*, which will be published annually and cover the current state of a certain important direction in the development of the materials. This year's edition will focus on applied superconductivity.

Superconducting materials are a separate class of electrical conductors which exhibit zero (in some cases, near zero) electrical losses and a number of quantum mechanical properties resulting in a lot of novel and unique electrical and electronic devices and systems. The field rapidly grew after the discovery of the phenomenon in 1911 with important milestones being the 1957 publication of the Bardeen–Cooper–Schrieffer (BCS) theory, the 1962 prediction and observation of Josephson effects, and the discovery at that time of new superconducting alloys capable of carrying high currents in high magnetic fields. After unexpected finding in the late 1980s of cuprates with transition temperatures above the boiling point of liquid nitrogen, superconductivity began to be observed in simple benchtop experiments. This discovery caused renewed interest to the field of superconductivity and an unprecedented amount of relative worldwide research. Just superconductivity has brought quantum physics to the scale of the everyday world where a single superconducting quantum state may extend over a distance of kilometers and even more. Superconducting technologies such as magnets, motors, classical and

quantum computing, power cables, and so on strongly accelerate the progress of science and technology. This progress leading to new unanticipated results has been accompanied and supported by advances in fabrication and nanoscale patterning technologies

This book presents four overviews of recent results obtained by their authors, as well as our current knowledge in a particular applied superconductivity area. An effect of disorder on superconductor characteristics is reviewed in Chapter 1. In Chapter 2, the focus is on mixing energies and critical decomposition temperatures of iron-based solid solutions whose properties in the superconducting state are very different from those of cuprates, the most studied high-temperature superconducting compounds. Chapter 3 presents experimental and theoretical investigations of proximitized nanocomposites based on half-metallic manganites – singlet *s*- or *d*-wave superconductors. Finally, within the framework of a self-consistent effective field approximation of the time dependent perturbation theory, unusual behavior of a hybrid structure formed by normal and superconducting proximitized films is discussed in Chapter 4.

Vinnytsia–Kyiv   Mikhail BELOGOLOVSKII
November 2022

CONTENTS

1. DISORDER-ENHANCED SUPERCONDUCTIVITY

M. Belogolovskii[1, 2, 3], A. Shapovalov[1], E. Zhitlukhina[2, 4], P. Seidel[3]

Abstract

Correlation between superconductivity and disorder remains an intriguing and challenging puzzle in condensed matter physics. According to the Bardeen–Cooper–Schrieffer (BCS) theory, the superconducting phenomenon emerges due to the binding of mobile electrons into Cooper pairs that forms a macroscopic quantum coherent state. For a weakly disordered system, the well-known Anderson theorem states that superconductivity is insensitive to disorder factors, such as elastic scattering centers, not affecting the time-reversal symmetry. Nevertheless, this statement is valid only for initially isotropic, homogeneous, and weak-coupling materials. It was shown that for a variety of non-uniform superconducting structures, the homogenization of the superconducting pair potential should result in the degradation of superconducting properties. Later, it was found that the naive expectations of unaffected or suppressed superconductivity in disordered materials, in general, are inappropriate. Due to these findings, nowadays attention is mainly focused on measuring and explaining *disorder-enhanced superconductivity.* This chapter updates the research status of such activities and presents some original results in this field obtained by the authors. The materials discussed below are classified according to their structural order. Two extreme cases are crystalline binary alloys with a periodic translation of a single unit cell (long-range order) and amorphous compounds with the appreciable degree of short-range or even medium-range order and the lack of inherent periodicity. Concerning solid-solution crystalline binary alloys, we focus on an enhancement of properties unexpected for a simple mixture of constituent elements. We argue that the amorphous structure made the requirement of substrate-film lattice matching, typical for crystalline layers, unnecessary thus providing good adhesion of amorphous films to different substrates. An intermediate case between the two extremes is high-entropy alloys, multi-component materials in which five or more elements randomly occupy a certain crystallographic site. Such highly atomic-disordered state produces many superior mechanical and / or thermal

characteristics (in particular, superconducting electrical properties), which are robust against atomic disorder or extremely high pressure. We are also discussing an effect of the structural disorder on the vibrational spectrum of superconducting materials and discuss possible explanation of disorder-enhanced superconducting properties in the framework of traditional phonon-mediated strong-coupling superconductivity.

✉ Mikhail Belogolovskii
belogolovskii@ukr.net

[1] Kyiv Academic University, Academician Vernadsky Blvd. 36, 03142 Kyiv, Ukraine

[2] Vasyl' Stus Donetsk National University, 600-richchia vul. 21, 21021 Vinnytsia, Ukraine

[3] Institut für Festkörperphysik, Friedrich-Schiller-Universität Jena, Helmholtzweg 3, 07743 Jena, Germany

[4] O. O. Galkin Donetsk Institute for Physics and Engineering, National Academy of Sciences of Ukraine, Nauki Ave. 46, 03028 Kyiv, Ukraine

1.1 Introduction

First study of the disorder effect on superconductivity was carried out in the 1930s by Shalnikov [1.1]. This activity was revived again in the late 1950s by Anderson [1.2] and Abrikosov and Gor'kov [1.3]. According to Anderson, dilute elastic scattering centers (impurities, dislocations, etc.), which could not affect the time-reversal symmetry, have no significant effect on thermodynamic properties and pair potential of three-dimensional *s*-wave BCS superconductor with a good crystalline structure (this statement is known in the literature as Anderson theorem). In contrast, as shown by Abrikosov and Gor'kov, magnetic impurities of arbitrary concentration may destroy superconductivity. However, when disorder reaches a critical level that can induce the localization of the electron wave function, a quantum phase transition, usually termed a superconductor-insulator transition, is emerging [1.4, 1.5]. Therefore, study of dirty superconductors gives a unique possibility to analyze competition between Cooper pairing of electrons and their Anderson localization arising due to intensive scattering processes from dopant centers.

How does superconductivity behave when the amount of disorder in the studied material is increasing? The answer to this question has been discussed in a number of reviews [1.6, 1.7, 1.8]. It was found that similar to many physical and chemical characteristics such as mechanical, electrical, magnetic, thermal, *etc.* superconducting properties reveal marked changes with disorder, as well. New aspects of this problem include, for example. quasi-1D systems which can exhibit long-range order at low temperature, but are heavily influenced by disorder [1.9, 1.10] and quasi-2D monolayers where the unusual enhancement of T_c was attributed to the multifractality of electron wavefunctions [1.11]. Some important conclusions can be drawn by analyzing experiments with strongly correlated superconductors, in particular, with high-T_c cuprates. A sharp increase in the critical temperature was found to be accompanied by the suppression of charge density waves, which indicates a strong competition between them and a still unknown mechanism of the high-temperature phenomenon [1.12]. On the other hand, the Van Hove scenario for HTSC [1.13, 1.14] was shown to be valid even for weak disorder [1.15].

As a result of joint efforts, our understanding of dirty superconductors has changed a lot over the past few decades. In particular, it became evident that

the Anderson theorem is applied only to initially isotropic, homogeneous, and weak-coupling materials. A specific case of a system without translational symmetry where the Anderson theorem is not satisfied is a normal-metal (N) film proximitized to a superconductor [1.16]. Its inapplicability shows up, first, in the homogenization of pair potentials over the N and S layers that becomes evidently lower than that in a pure S material. This conclusion, in fact, is valid not only for N/S bilayers but also for a variety of inhomogeneous weakly disordered superconducting structures. It is remarkable that the results by Arnold [1.16] for very thin N and S layers bear a striking resemblance to the McMillan tunneling model [1.17] of the proximity effect for two N and S layers separated by a tunnel barrier. The correspondence arises from a similar treatment of lifetime effects. It is also not surprising that analogous expressions are appropriate for multiband superconductors with nonmagnetic impurity scattering treated within the Born approximation [1.18, 1.19]. As in the common case of an anisotropic superconductor [1.20], interband scattering reduces the critical temperature T_c and finally leads to a *single* order parameter, in overall agreement with previous studies [1.21].

In general, the effect of impurities and / or defects on the properties of a primary superconductor is strongly material-dependent, compare the data for ferro-pnictides [1.22], amorphous molybdenum silicon these films [1.23], niobium titanium nitride films [1.24], oxide interfaces [1.25], or nanostructured Sn samples [1.26]. In most cases, the traditional design of novel superconductors started from a primary or host substance, to which a new component or components were added for improving the material performance. The above naive expectations that in this case T_c should remain unaffected or can only decrease, was found inappropriate, and nowadays a lot of attention is focused just on measuring and explaining ***disorder-enhanced superconductivity***. For example, many of actual transition-metal alloys with attractive superconducting properties have been found to be located in the centers of the phase diagrams rather than close to its corners. The second subsection of the overview illustrates this observation with an example of binary Mo-based alloys. Another case of extreme disorder is an amorphous (structurally disordered, i. e., disordered in the spatial arrangement of atoms) superconducting phase stabilized in the form of thin films by some metals and metallic alloys.

The discovery of superconductivity in the amorphous phase dates back to early 1950's when quench condensed films of amorphous Bi were reported to be superconducting with $T_c = 6.1$ K [1.27] in contrast to crystalline Bi that is a superconductor with the critical temperature of 0.53 mK [1.28]. It was claimed that the superconductivity in amorphous Bi results from its higher packing density than crystalline Bi [1.29] but convincing experimental evidence was absent. Later it was found that some elements which are non-superconducting at all, such as Be [1.30], become superconducting in the amorphous state [1.29, 1.31]. At the same time, other elements like Pb are good superconductors in the crystalline phase while disorder lowers T_c. We present some results for amorphous superconducting compounds including original ones and discuss them in the third subsection of the chapter.

From the fundamental point of view, the most important task in the study of disorder-enhanced superconductivity remains to answer the question – why T_c's of highly disordered superconductors quite often exceed those of the crystalline counterparts. In the paper [1.32], the authors proposed two possible mechanisms for increasing the superconducting transition temperature T_c by nonmagnetic disordering factors in both conventional and unconventional (sign-changing gaps) superconductors. In the first scenario, relevant to multi-band systems, the origin of the T_c growth is the density-of-states enhancement driven by resonant states in near-Fermi-level bands while the second one applicable to systems close to localization it is related to random disorder-generated local density-of-states modulations. In the third subsection of the overview, we argue that superconductivity in such materials is usually strongly (or at least moderately) coupled, with the electron-phonon coupling parameter $\lambda \geq 1$ and the superconducting gap Δ much larger than its value predicted by the BCS theory: $\Delta = 1.76 k_B T_c$. It means that we should look for the fundamental explanation of these findings within the framework of the Eliashberg theory of strong-coupling phonon-mediated superconductivity [1.31], using details depending on the nature of the disorder and superconductor pairing symmetry. This issue is discussed at the end of the third subsection.

The novel tendency in studying disorder-enhanced properties is concentrated not on the materials formed by a single host and an additional component as those discussed in the second subsection but rather on compounds with

multiple elements which crystallize as solid solutions. In such systems known as high-entropy alloys (HEA), the structural order / disorder can be characterized through the entropy, a measure of the randomness. Such alloys composed typically of four or more components are usualy characterized by simple structures with extremely high chemical disorder and high entropy of mixing stabilizing the crystal structure and resulting in highly tunable properties [1.33−1.36]. The highly atomic-disordered HEA state produces many superior mechanical and / or thermal characteristics. Superconductivity has become one of the most important topics in this field since the discovery of a bcc HEA superconductor in 2014 [1.37]. Our fourth subsection is dealing with superconducting high-entropy alloys, which are expected to be useful for realizing the relationship between crystalline and amorphous superconductors.

1.2 Solid-solution crystalline binary alloys: is the rigid band approximation adequate?

A binary superconducting alloy is a mixture of two chemical elements of which at least one is a metal element forming a substance with conducting characteristics. The most common and oldest alloying process is performed by heating the base metal beyond its melting point and then dissolving the solutes into the molten liquid even if the melting point of the solute is far greater than that of the base. By adding another element to a metal, differences in the size of the atoms create internal stresses in the lattice of the metallic crystals, which sometimes enhance its properties.

Understanding electronic characteristics of binary random alloys has become a topic of considerable interest in solid-state physics. The first two approximations used in the study of these compounds were rigid band and virtual crystal approximations, which are valid for the case when a periodic crystal structure of the materials discussed is well defined. Even oversimplified, they can nevertheless suggest a way allowing the development of alloys with properties tuned for specific applications, in particular, when they depend on variations in Fermi surface topology induced just by alloying. The rigid band model, in which the band structure and density of states of the solvent metal remain unchanged upon alloying with a solute allows predict these

variations [1.38]. Although the rigid band behavior has been confirmed for many nearly free electrons and some systems with transition metals [1.39–1.41], its applicability remains questionable, especially when the solute strongly perturbs the local electronic structure of the solvent [1.42]. From this viewpoint, understanding the physical properties of simple binary random alloys is very useful for facilitating a detailed picture of the development of conduction states in complex alloys containing transition metals. As an example, we will discuss below the evolution of a band structure and the Fermi surface of $Mo_{1-x}Re_x$ alloy in normal and superconducting states as functions of its composition.

As for the normal state, we refer to the work [1.43] where the authors presented detailed experimental and theoretical study of the electronic structure of $Mo_{1-x}Re_x$ random alloys. They measured electronic band dispersions for clean and hydrogen-covered $Mo_{1-x}Re_x$ alloys with $x = 0 – 0.25$ using angle-resolved photoemission spectroscopy and performed numerical calculations by the Korringa–Kohn–Rostoker coherent-potential-approximation method, a simplest self-consistent approximation. In the latter approach, one regards the total scattered wave as composed of contributions from each atom while the effective wave incident on a given atom excludes its own effect. The result is a product of the atomic t-matrix and the effective wave [1.43]. As for the superconducting state, its analysis is based on our previous publications [1.44–1.45].

Re ($5d^5 6s^2$) has one more electron per atom than Mo ($4d^5 5s^1$), which in the rigid band approximation would be shared with the molybdenum host. The authors [1.43] found that with increasing Re concentration, bulk and surface electronic bands are shifting away from the Fermi energy E_F due to two factors: (i) the aforementioned charge donation and (ii) increase in the occupied bandwidth, most notably for bands more than 2 eV below E_F, see Fig. 1.1. However, this effect is not uniform, with larger shifts observed at higher binding energy. Two other deviations from rigid band behavior were as follows: (i) a surface-localized state shifted in a notably non-rigid way and (ii) spin-orbit interaction impact increased with growing rhenium concentration, again leading to non-rigid modifications of some bands.
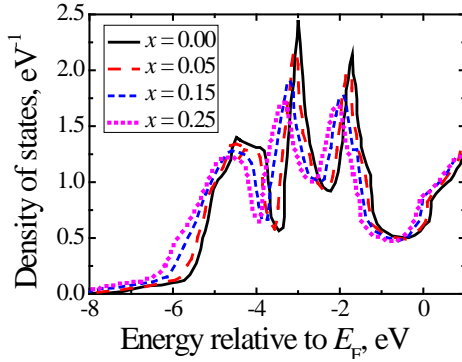
Fig. 1.1 – Configurationally averaged density of electronic states of $Mo_{1-x}Re_x$ random alloys ($x = 0.00$, 0.05, 0.15, and 0.25) calculated using the Korringa–Kohn–Rostoker coherent-potential-approximation method. Adapted from Fig. 1 in Ref. [1.43]

The authors [1.43] also revealed an electronic topological transition which may impact many physical properties of alloys. It occurs when the Fermi surface changes its topology as E_F is moving through a van Hove singularity in the density of states $N(E_F)$. This idea is traced back to the work by Ilya Lifshitz who related a change in the topology of the Fermi surface $E(\mathbf{p}) = E_F$ of a pure metal subjected to elastic strains to anomalies in thermodynamic quantities of metals [1.46−1.48]. The effect is arising due to the continuous variation of some parameter (*e. g.*, pressure or impurity concentration), due to which the difference $z = E_F − E_c$ between the Fermi energy E_F and the critical energy E_c, at which the topology of the constant energy surface is changing, passes through zero continuously. This leads to the modification in the Fermi-surface connectivity, for example, an appearance of a new cavity or the rupture of a connecting neck with varying external parameter. At the temperature $T = 0$ K, the grand thermodynamic potential Ω acquires an irregular correction $\delta\Omega = −\alpha|z|^{5/2}$ and that is why this effect was also called the phase transition of the 2.5-order [1.47], referring in this case to the Ehrenfest terminology. At $k_B T \ll E_F$, related anomalies manifest themselves not only in thermodynamic characteristics of metals, but also in superconducting parameter-versus-z dependencies, as was evidenced by Brandt *et al*. in the paper [1.49] just by analyzing pressure induced changes in the properties of superconducting Tl–Hg alloys.

In fact, topology and alloying are often closely intertwined in condensed matter physics. In both cases, one seeks to characterize not the details of a

particular band structure or disorder configuration, but the basic physics of the phenomenon. Returning to the $Mo_{1-x}Re_x$ alloys, we are referring to detailed first-principles calculations of their bulk electronic structure by Skorodumova *et al.* [1.41] who predicted two Lifshitz topological transitions at 2 % and 6 % Re concentrations occurring near the middle of the N–H line in the bulk Brillouin zone. Comparison of Fermi surfaces for pure Mo and $Mo_{0.75}Re_{0.25}$ in Ref. [1.43] confirmed it by revealing the van Hove singularity at 5 % rhenium concentration, i. e., very close to the theoretical predictions [1.41]. Recent results of resonant photoemission spectroscopy experiments [1.50] proved the existence of two electronic topological transitions at critical Re concentrations of $x_{c1} = 0.05$ and $x_{c2} = 0.11$.

It is known that the addition of rhenium to molybdenum improve the ductility of the material. The stress required to produce a fixed amount of strain higher than 3 % is minimal around $x = 0.07$ [1.51]. Smith et al. [1.52] found phonon softening along the N–H direction of the Brillouin zone when Mo-Re alloys undergo the Lifshitz transition and it is just the location of a Fermi surface pocket that appears when more than 5 at. % of rhenium is added to molybdenum [1.43]. Electronic states of the small group of carriers are localized due to the random potential introduced in the system when the composition is changed [1.53]. This effect is expected to be very small and its detection should require extremely sensitive techniques. Nevertheless, Ignat'eva [1.53] revealed large oscillations in the pressure dependence of T_c and in temperature derivatives of the normal-state thermoelectric power and resistivity. She argued that the localization of electrons filling the new states arising due to the topological changes of the Fermi surface causes the observed oscillations in related characteristics. The localized states against a background continuum give rise to Fano resonance in photoemission spectroscopy measurements detected in the $Mo_{1-x}Re_x$ system for $x > x_{c1} = 0.05$ [1.50]. This observation was interpreted as the result of the electron-like states localization in the newly appeared Fermi pocket. Next, let us discuss how the changes in the topology influence superconducting properties of the Mo-Re alloys and why it may considerably enhance the transition temperature to the superconducting state.

From the superconductivity viewpoint, it is important that the proximity of the Fermi surface to van Hove singularities drastically enhances interaction effects and can lead to the emergence of a flat band, where all the states have

the same energy. Since the flat band has a huge density of electronic states, this may considerably increase the transition temperature T_c. Notice that in ordinary superconductors, the singular density of electronic states emerging at the transition point generates non-analytical behavior of superconducting parameters as a function of the external factor modifying the shape of the Fermi surface [1.47]. In the paper [1.54], the authors presented a detailed study of temperature and magnetic field dependences of the magnetization M and heat capacity C in $Mo_{1-x}Re_x$ alloys with $x = 0.25$ and 0.4, *i. e.*, above two topological transitions in the Fermi surface. Notice that the $Mo_{0.6}Re_{0.4}$ alloy was identified as a strong coupling superconductor with the ratio of an energy gap $\Delta_0 = \Delta(T = 0)$ to the critical temperature $2\Delta_0/k_B T_c = 5.0$, that is well above the value of 3.52 predicted by the BCS theory of a weakly coupled superconductor (Fig. 1.2). The normalized values $\Delta C_S/\gamma T_c$ of the heat capacity ΔC_S jump at T_c (γT is an electronic contribution to the normal-state heat capacity) are about 1.7 and 2.0 for the $Mo_{0.75}Re_{0.25}$ and $Mo_{0.60}Re_{0.40}$ samples studied in the work [1.54], respectively. These values are also substantially higher than the BCS value of 1.43 pointing out again that superconductivity in the binary random $Mo_{1-x}Re_x$ alloys with $x > x_{c2}$ is at least nontrivial as it follows from the electron-phonon coupling constant-vs-Re concentration dependence, see Fig. 1.2.

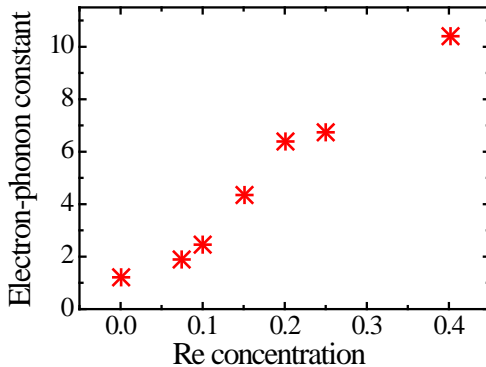Fig. 1.2 – Variation of the electron-phonon coupling constant λ as a function of Re concentration x in $Mo_{1-x}Re_x$ alloys. Adapted from Fig. 5 in Ref. [1.55]

Fig. 1.1 demonstrates the fundamental possibility of using the rigid band model for a qualitative description of changes in the electronic structure of random binary alloys with increasing the solute concentration, while Fig. 1.2

shows a strong enhancement of the electron-phonon interaction coupling for large Re concentration. The question arising is if it is possible to predict minor details in the electronic structure, such as relatively small changes in the Fermi surface topology. For example, do predicted two Lifshitz topological transitions at small Re concentration [1.41] really exist? As was explained above, the opening of a new cavity in the Fermi surface can lead to the appearance of an additional energy gap in the spectrum of single-particle excitations of a superconductor studied. Can we detect it?

Unfortunately, the identification of a second gap can be extremely problematic. Fig. 1.3 exhibits the temperature dependence of the ratio $\Delta C_S / \gamma T_c$ for two Mo-Re compounds studied in Ref. [1.54]. Dotted lines in Figs. 1.3a and 1.3b represent $C_S(T)$ behavior in the superconducting state with a single isotropic superconducting gap $\Delta_0 / k_B = 19.0 \pm 0.5$ K for the $Mo_{0.75}Re_{0.25}$ alloy and $\Delta_0 / k_B = 26.5 \pm 0.6$ K for the $Mo_{0.60}Re_{0.40}$ alloy.
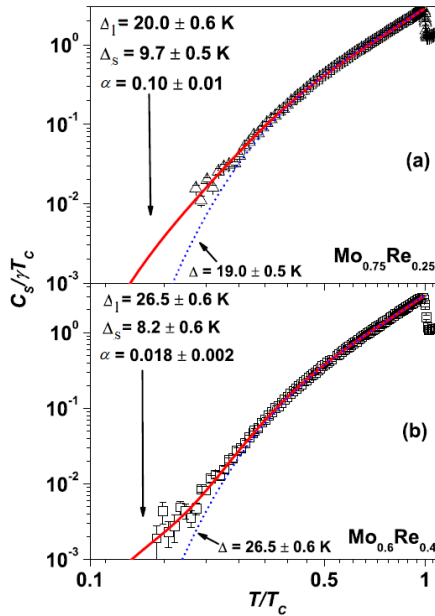

Fig. 1.3 – Temperature dependences of the electronic heat capacity in the superconducting state plotted as a function of the ratio T/Tc for Mo0.75Re0.25 (a) and Mo0.60Re0.40 (b) samples. The lines are fits to the experimental data (open symbols) within single-gap (dotted lines) and two-gap (solid lines) theoretical approaches. Adapted from Fig. 7 in Ref. [1.54]

We can see that experimental values of $C_S(T)/\gamma T_c$ at low temperatures are systematically higher than calculated ones. Realizing this, the authors of Ref. [1.54] tried to fit the experimental data using an equation for a two-band superconductor

$$\frac{C_S(T)}{\gamma T_c} = \alpha \frac{C_{Ss}(T)}{\gamma_s T_c} + (1-\alpha) \frac{C_{Sl}(T)}{\gamma_l T_c} \qquad (1.1)$$

with $C_{Ss}(T)$ and $C_{Sl}(T)$, contributions to heat capacity from a small Δ_s and a large Δ_l superconducting gaps, $\alpha = \gamma_s/(\gamma_{s+}\gamma_l)$ defines the fraction of the small gap, $\gamma_{s,l}$ are related normal-state coefficients. They found that the resulting lines are perfectly consistent with the measured $C_S(T)$ data, see solid lines in Fig. 1.3 where the values of Δ_s, Δ_l, and α are specified. Notice that a clear deviation from the single-gap behavior was observed already in an earlier study of the temperature dependence of electronic heat capacity in $Mo_{0.60}Re_{0.40}$ alloy [1.56] but was ignored. Now it is evident that the discrepancy between theory and experiment can be removed by taking into account the presence of *two superconducting gaps*.

Magnetization-vs-external magnetic field measurements at various temperatures made it possible to estimate the upper critical field $H_{c2}(T)$ dependencies as the field in the isothermal *M-H* curves at which the irreversible (giving rise to a hysteresis loop) magnetization M reduces to zero. It was found that the temperature impact on H_{c2} estimated using the Werthamer–Helfand–Hohenberg model matches with the experimental curves only at temperatures close to T_c. The lower critical field H_{c1}, below which a type-II superconductor is in the Meissner state, was found analyzing *dM(H)/dH* dependencies. For a superconductor in the local limit with $\xi(0) << \lambda$, $\xi(0)$ and λ are coherence length and London penetration depth, the normalized superfluid density $\rho_s(T)$ reads as [1.54]

$$\rho_s(T) = \frac{\lambda^2(0)}{\lambda^2(T)} = \frac{H_{c1}(T)}{H_{c1}(0)}. \qquad (1.2)$$

For a single gap superconductor, $\rho_s(T)$ is given by [1.57]

$$\rho_s(T) = 1 + 2\int_0^\infty N_S(\varepsilon,T)(df(\varepsilon,T)/d\varepsilon)d\varepsilon \qquad (1.3)$$

with the Fermi-Dirac distribution function $f(\varepsilon)$ and the normalized density of single-particle states in a superconductor [1.58]

$$N_S(\varepsilon,T) = \mathrm{Re}\left(\varepsilon / \sqrt{\varepsilon^2 - \Delta(T)^2}\right), \qquad (1.4)$$

$\varepsilon = E - E_F$. Dotted lines in Figs. 1.4a and 1.4b show the temperature dependence of normalized superfluid density calculated using Eq. (1.3) for an isotropic single-gap superconductor with $\Delta_0/k_B = 15.5 \pm 0.5$ K for the $Mo_{0.75}Re_{0.25}$ alloy and $\Delta_0/k_B = 20.5 \pm 0.4$ K for the $Mo_{0.60}Re_{0.40}$ alloy. Similar to Fig. 1.3, the estimated theoretical curve matches well with the experimental data at high temperatures while a marked deviation observed at low temperatures indicates possibility of the two-gap superconductivity. Acting like above for the heat capacity exhibiting an anomalous feature in its temperature dependence, see Eq. (1.1), the authors [1.54] got an excellent agreement between the measured and calculated curves with the parameters Δ_s, Δ_l, and α indicated in Fig. 1.4. These values noticeably differ from those in Fig. 1.3. Possibly, this is caused by the fact that the superfluid density estimated from H_{c1} is a local property whereas heat capacity is a bulk (that is, averaged) characteristic [1.54].

Nevertheless, the above arguments supporting a two-band / two-gap scenario in superconducting random Mo-Re alloys (Figs 1.3 and 1.4) can only hint at the presence of two superconducting order parameters while it would be desirable to get the related information from the experiments that could provide direct evidence of the two gaps presence without additional calculations. Let us emphasize, that tunneling and point-contact spectroscopies schematically shown in Fig. 1.5 are exactly such techniques allowing one to interpret the measured differential conductance characteristics qualitatively without resorting to complicated model concepts [1.58]. As well known, related spectroscopic setups usually consist of two metallic electrodes (at least, one of them is in the superconducting state) divided by resistive nanometer-scale region. Its task is to take over the entire voltage drop V applied to the setup creating thus a difference $\Delta\mu = \mu_L - \mu_R$ in chemical potentials of the left (L) and right (R) electrodes. Modifying the drop V value, we are changing the difference $\Delta\mu = eV$ and thereby are able to probe unoccupied and occupied states in the excitation spectra of the conducting electrodes.
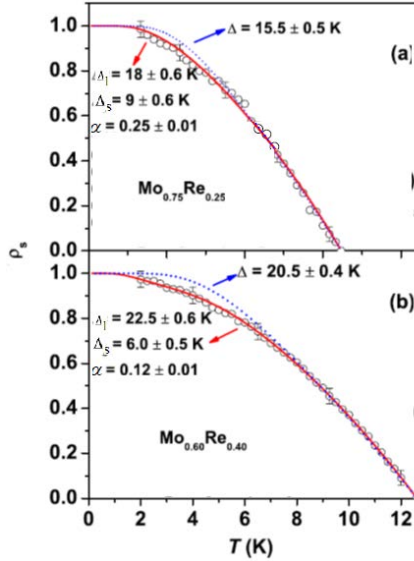
Fig. 1.4 – Temperature dependences of the superfluid density of states plotted
as a temperature function for Mo0.75Re0.25 (a) and Mo0.60Re0.40 (b) samples.
The lines are fits to the experimental data (open symbols) within single-gap (dotted
lines) and two-gap (solid lines) theoretical approaches. Adapted from Fig. 6 in Ref. [1.54]
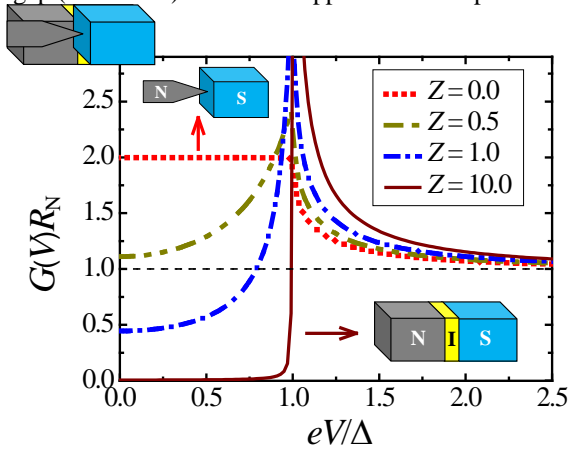
Fig. 1.5 – Simulated differential conductance–versus–voltage curves
for zero-temperature coherent quantum transport across a one-dimensional normal
metal-barrier-superconductor trilayer with various barrier transparences.
Their shapes are controlled by the parameter Z. Two extreme limits, corresponding
to a point contact (Z = 0) and a tunnel junction (Z >> 1), are illustrated schematically

Applying this idea, two extreme junction-spectroscopy techniques (tunneling and point-contact) differ only in the ways of creating the interlayer between two metals often called a weak link. A simplest, from the realization viewpoint, version of the high-resistive interlayer is a narrow constriction between two wide electrically conducting regions, whose width is comparable to the electronic wavelength λ_F, see the inset in Fig. 1.5. The conductance G of such device known as a quantum point contact can be as small as $G_0 = 2e^2/h \approx$ 77.5 μS, the universal conductance quantum [1.59]. This relation is valid for truly atomic dimensions when two bulk metals, reservoirs of electrons in local equilibrium, are connected by a quasi-one-dimensional single-atom constriction [1.60]. The G value grows with increasing the width w of the electron waveguide through which a small integer number of transverse modes $N \approx 2w/\lambda_F$ can propagate at the Fermi level E_F.

Tunneling spectroscopy that played a central role in the experimental verification of the microscopic theory of superconductivity in traditional superconductors represents an opposite case of the interface transparency. Conventional tunnel junction shown schematically as an inset in Fig. 1.5 is planar with a several nm-thick oxide interlayer, an area prohibited by classical mechanics for electrons at the Fermi level of electrodes and for this reason often named a barrier. Hence, the difference between two main techniques is to a great extent quantitative, namely, transition probabilities for charges to be transferred between junction electrodes in a certain quantum channel is near unity for the point-contact spectroscopy while it is much less than unity in the tunneling approach [1.61].

The most popular model to calculate the differential conductivity $G(V) = dI(V)/dV$ (the derivative of the current I across the contact with respect to the voltage V applied to it) of the normal metal-barrier-superconductor contact with a barrier of arbitrary transparency is that proposed by Blonder, Tinkham, and Klapwijk (BTK) [1.61]. The model assumes ballistic and one-dimensional character of the charge transport through the contact of N and S metals with a nanometer-thin scattering potential localized at the N-S interface. Its effect is usually considered by introducing a potential barrier with a thickness d_B and the decay length l_B inside it. For a strong inequality $d_B \ll l_B$, transmission t and reflection r amplitudes read $t = i/(i - Z)$ and $r = Z/(i - Z)$, where i is the imaginary unit, see the details in the papers [1.62, 1.63].

Ultimately, the parameter Z determines the probability of electron transmission through the barrier $D = 1/(1+Z^2)$ in the normal state as well as its probability to be reflected back $R = 1 - D = Z^2/(1+Z^2)$. The way of further calculations aimed to find the ratio of differential conductance in superconducting $G_S(V)$ and normal G_N states is described in detail in the work [1.63]. Possible effect of inelastic-scattering processes in the superconductor is taken into account by introducing a constant imaginary part in the electronic energy $E \rightarrow E + i\Gamma$, where Γ is known as the Dynes parameter [1.64]. As a result, we have three adjustable parameters for a single-band superconductor, the energy gap Δ, the interface scattering efficiency Z, and the Dynes parameter Γ. In the case of a two-band superconductor, this number increases to seven: Δ_l, Δ_s, Z_l, Z_s, Γ_l, Γ_s and, finally, the weighting factor $w_l < 1$ ($w_s = 1 - w_l$), which specifies the relative contribution of the two bands to the measured curve $G(V) = w_l G_l(V) + w_s G_s(V)$ [1.64].

In point contacts, the channels with the highest transmission probability determine the current along the device and, as a result, the scattering strength Z is nearly zero. In this case, for an electron (hole) incident on the interface from the N side at energies less than the superconductor energy gap Δ, the ballistic throughput across an N/c/S point contact (c is the constriction) is dominated by a quantum process called Andreev reflection. Its details are as follows. Electron (hole), arriving from the N side, forms a Cooper pair in the S electrode reflecting back a hole (electron) from the electron band with opposite spin and group velocity to the incident electron (hole) but with almost equal momentum. It is clear that this effect causes an enhancement of the conductance below the superconducting energy gap Δ, and the ratio of below-gap and above-gap conductance values equals 2 for an ideal point contact with a conventional superconductor (Fig. 1.5).

With increasing Z, the shape of the differential conductance $G(V)$ for an N/I/S trilayer transforms from a flat section at $|V| < \Delta/e$ to peaks at $|V| = \Delta/e$. From Fig. 1.5 illustrating these changes at very low temperatures, it is clear that the Andreev-reflection mechanism, that defines the shape of the conductance spectrum for a point contact with $Z \approx 0$, as well as the tunneling transport allow us to interpret measured $G(V)$ curves and to reveal qualitatively the energy gap value without involving complex model concepts.

$\Delta_l = 0.8\,\mathrm{mV}$ $\quad \Delta_s = 0.22\,\mathrm{mV}$

$\Gamma_l = 0.4\,\mathrm{mV}$ $\quad \Gamma_s = 0.001\,\mathrm{mV}$

$Z_l = 0.5\,\mathrm{mV}$ $\quad Z_s = 0\,\mathrm{mV}$
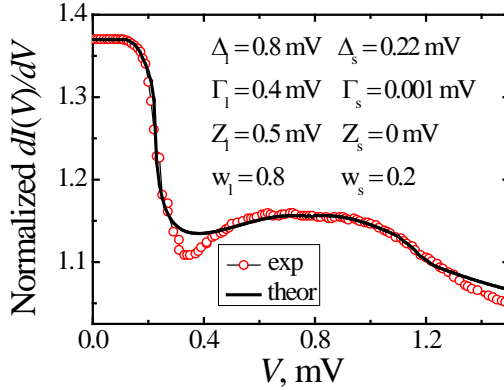
$w_l = 0.8$ $\quad w_s = 0.2$

Fig. 1.6 – Normalized differential conductance–versus–voltage curve measured for a representative point-contact sample formed by a silver tip and a random Mo0.52Re0.48 alloy film (dots) compared with a fitting curve (solid line). The two energy gaps differ markedly: $\Delta_s = 0.22$ meV and $\Delta_l = 0.8$ meV, the contribution of the band with a larger gap Δ_l is dominant, the measurement temperature was 4.2 K

We have performed two different kinds of the junction-spectroscopy experiments using Mo-Re based tunneling trilayers [1.44] and point-contacts [1.45]. In the latter case, the N electrode was made of silver, its point contacts with the studied Mo-Re alloy were created both on film and bulk samples. Thin alloy layers with an approximately equal concentration of components, thicknesses ranging from 90 to 150 nm, and critical temperatures about 9 K were obtained by magnetron sputtering of a $Mo_{0.52}Re_{0.48}$ target. Structure and phase composition of the films were controlled by electron microscopy and electron diffraction, as well as by X-ray diffraction. The concentration of alloy components in the films determined using X-ray photoelectron spectroscopy with an accuracy of 5–6 at. % well corresponded to the target composition. Grain size spread was tiny. This uniformity revealed itself in high films resistance to structural transformations and stable electrophysical properties during thermal cycling. The measured differential conductance spectra d$I(V)$/dV of contacts based on Mo-Re alloys with approximately equal component contents demonstrated the presence of two energy gaps, larger Δ_l and smaller Δ_s ones. Typical $G(V)$ curve shown in Fig. 1.6 represents a sum of two similar characteristics of N/S contacts with an almost ideal interface. The fitted parameters are indicated in Fig. 1.6. Notice that due to the

small area of contacts, we got an information only from individual micro-sized crystallites with different crystallographic directions, while, say, measurements of the electronic heat capacity for a molybdenum-rhenium alloy [1.54] provide characteristics averaged over all directions. Local changes in superconducting properties in the near-surface region may be a source of the differences between surface-sensitive techniques and those dealing with the bulk.
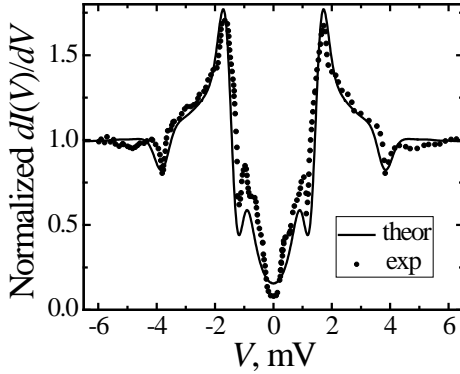
Fig. 1.7 – Normalized differential conductance–versus–voltage curve measured for a representative Pb/Al oxide/Al/Mo0.60Re0.40 tunnel junction (dotted curve) compared with a fitting curve (solid line). The energy gaps $\Delta s = 0.5$ meV and $\Delta l = 2.5$ meV reasonably agree with the values extracted from point-contact experiments, see Fig. 1.6, the contribution of the smaller-gap band was dominant, the measurement temperature was 4.2 K. Adapted from Fig. 2 in Ref. [1.44]

In Ref. [1.44], we presented our results for tunneling junctions based on $Mo_{0.60}Re_{0.40}$ polycrystalline films. The authors of Ref. [1.65] found that the native oxide of the Mo-Re alloy is grown up to thicknesses not more than 0.5 nm and are thinner that the oxides on Mo and Re surfaces. Therefore, in order to form a low-leakage tunnel junction on the Mo-Re film, they had to cover it with an Al overlayer, oxidized after that. Following the work [1.65], we have used artificial Al-oxide tunnel barriers and a 100 nm-thick lead counter-electrode to form low-leakage tunnel junctions for measurements in the gap region not carefully analyzed in the previous tunneling experiments [1.65]. If we are dealing with a two-gap superconducting electrode, $G(V)$ dependence for a tunnel junction should exhibit a two-peak structure. Fig. 1.7 demonstrates representative conductance spectrum of the Pb/Al oxide/Al/$Mo_{0.60}Re_{0.40}$ junctions exhibiting reach fine structure with a prominent peak at 1.7 mV, a small local

maximum on a steep slope at 1.0 mV, and a distinct dip at 3.8 mV shown by related arrows. An analysis of the measured data based on a complex inner-gap structure in transport characteristics of superconducting junctions with degraded interfaces [1.44] permitted to extract the values of the energy gaps $\Delta_s = 0.5$ meV and $\Delta_l = 2.5$ meV. The presence of the two superconducting gaps in the Mo-Re alloy probed by tunneling spectroscopy indicates that one of the most probable scenarios explaining the significant increase in T_c upon alloying Mo with Re may be interband interaction.

1.3 Amorphous versus crystalline superconductors: two structural extremes

Solids are characterized by a rigid structure of molecules, ions, or atoms arranged in an orderly or non-orderly manner. The major difference between crystalline (discussed above) and amorphous (to be discussed below) compounds lies just in the long-range structural order that can be always accurately defined by periodically translating unit cells. The lack of inherent periodicity with an appreciable degree of short-range and / or medium-range orders are distinct features of the amorphous phase.

Three-dimensional (3D) crystal is a solid material in which the constituents are organized in a highly ordered microscopic structure forming a lattice extending in all directions. The crystalline materials retain their original shape and consistency, their mechanical strength, thermal conductivity, refractive index, and electrical conductivity differ in diverse directions. Fast cooling such substances may lead to an amorphous structure with irregular geometrical shapes. For example, quartz is a hard crystalline mineral composed of silicon and oxygen atoms in a strict order, while it can turn into amorphous glass when cooled rapidly. Other examples of amorphous materials largely used due to their huge benefits and unique isotropic properties are rubber and polymers. Amorphous state has usually an internal structure comprising interconnected structural blocks that can be similar to the basic structural units in the corresponding crystalline phase of the same compound. Therefore, the type of a solid depends primarily on the connectivity between its elementary building blocks, namely, crystals are characterized by a high degree of connectivity while the structural blocks in amorphous materials have lower connectivity.

As was indicated above, some elements that are poor superconductors in the crystalline phase (such as Ga and Bi) or do not exhibit superconductivity at all (as Be [1.66]) become superconductive in the amorphous state [1.67, 1.68]. Early work [1.67] explained such finding by the lack of a densely packed structure in the crystalline phase and promotion of superconductivity by effectively compacting it. Other elements, such as Pb, have densely packed structure and are good superconductors already in the crystalline phase, but in this case, the disorder, if it is introduced, only reduces the critical temperature of the superconducting transition. Unfortunately, such explanation turned out to be insufficient and understanding the effect of structural disorder on super-conductivity remains a long-standing problem waiting for its solution, see the reviews [1.4, 1.69, 1.70].

Because of the lack of a theoretical framework able to describe, in a re-ductionism way, the effect of structural disorder as well as limited experi-mental characterization, amorphous materials are used quite rarely comparing to crystal counterparts. Nevertheless, there are some important fields as dis-plays, solar cells, optical fibers, and others where non-crystalline samples found their niches. The most important amorphous thin-film application is a few nm thin SiO_2 layer serving as an isolator above the conducting channel of a metal-oxide semiconductor field-effect transistor. Also, in some cases, the transition between amorphous and crystalline phases determines the device operation, for example, in phase-change memory setups.

Main applications need thin solid films of a few nanometers to some tens of micrometers thickness deposited upon a substrate with the goal of forming amorphous phases. Necessary (but not sufficient) condition for their occurrence is that the deposition temperature must be below 30 % of the melting tem-perature (for higher values of the deposition temperature, the surface diffusion of deposited atoms would allow for the formation of crystallites with a long-range atomic order) [1.71]. Emergence of separate building blocks when the system is crossing a continuous phase transition in finite time can be explained by the formation of topological defects described by the Kibble-Zurek mecha-nism valid in the limit of slow quenches. This approach predicts an universal power-law scaling of the density with the quench time in which the transition is crossed. While Kibble-Zurek scaling holds below a critical quench rate, for

faster quenches, the defect density and the freeze-out time become independent of them, exhibiting universal power-law scaling with the final value of the control parameter. Such amorphous metallic layers played a decisive role in the discovery of superconductivity in amorphous metals.

Historically, two different paradigms concerning the structure of amorphous solids were formulated in the 1950s, namely, the rigid band approximation and the random network approach which evolved into a modern structural theory of amorphous solids [1.72]. The modern interpretation considers structurally similar building blocks connected in a network, where intermediate-range order, that is, order on a scale larger than that of the individual building blocks, may persist up to a certain extent. However, even now some fundamental questions remain without answers. What is the extent of intermediate and long-range orders in the amorphous structure or what is the amount of randomness in the system? Second, how close is the relationship between the fundamental building blocks in amorphous materials and the corresponding crystals? Ref. [1.73] showed that it is possible to quantify the extent of structural similarity between amorphous and crystalline phases, thus shedding light on a problem debated for more than half a century. The authors of this work argued that there is no definite answer, valid for all amorphous materials but individual systems can show a degree of similarity toward certain crystalline polymorphs, which is not necessarily limited to short-range order. For some amorphous systems, the network building units might be very similar to those of a crystalline polymorph, while other systems may show distorted network building units but with more intermediate-range order.

Due to the very short mean free path of electrons, amorphous materials provide a good model platform for analyzing the correlation between superconductivity and disorder [1.4]. The appearance of novel vortex phases in such samples was another subject of interest [1.74, 1.75]. Finally, the extraordinary phase homogeneity, little dependent on the crystal structure of the seed layer, has led to the fact that homogeneously disordered (amorphous) superconducting thin films are promising materials for use in superconducting micro- and nanoscale devices as superconducting detectors [1.76, 1.77] and vortex memory devices [1.78].

Below we will take as an example our results for silicon- and germanium-based amorphous superconducting films, α-MoGe and α-MoSi, with critical

temperatures T_c up to about 7.5 K, which have been previously used in high-performance integrated quantum photonic circuits (see the reviews [1.79–1.81] and references therein). Recent novel applications for α-MoGe and α-MoSi superconductors include quantum phase slip nanowire devices [1.82, 1.83], superconducting memory [1.84], hybrid superconductor-ferromagnet spin valves [1.85], *etc*. High normal-state resistivity and low superfluid density of amorphous superconductors can be exploited for the design of SQUIDs with tunable characteristics [1.86] as well as may be useful for building protected qubits [1.87].

Below we present our point-contact data for a MoSi thin layer stabilized in an amorphous phase and main characteristics of α-MoGe based Josephson junctions, which were fabricated and studied for the first time in Ref. [1.88]. Concerning the α-MoSi-Ag point contacts, we have followed the methodology described above. Measuring differential conductance–versus–voltage characteristics and comparing them with theoretical expectations [1.61] we have found the energy gap value equal to 0.35 meV, see Fig. 1.8.
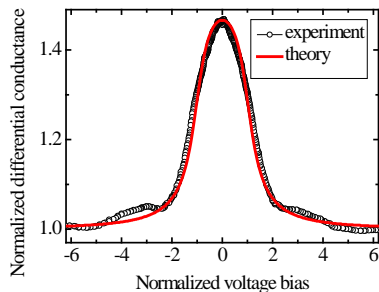
Fig. 1.8 – Normalized differential conductance $G(V)R_N$ versus normalized voltage bias eV/Δ characteristic measured for a representative point-contact sample formed by a silver tip and an amorphous α-MoSi sample (dots) compared with a fitting curve (solid line). The energy gap $\Delta = 1.18$ meV, the effective interface scattering parameter $Z = 0.11$ meV, the Dynes parameter $\Gamma = 0.28$ meV, the normal-state resistance $R_N = 17.2$ Ohm

Our next step was the fabrication of Josephson junctions based on amorphous superconducting films [1.88]. Up to now, the main technological approach in this field remains the whole-wafer Nb/Al/AlO$_x$/Nb trilayer process [1.89], when the junctions are fabricated *in situ* and the tunnel barrier is formed by thermal oxidation of an Al overlayer deposited on the bottom Nb

layer. The barrier transparency in such trilayer is mainly controlled by the oxygen exposure, the product of oxygen pressure and oxidation time [1.90]. An advantage of the Nb/Al methodology is that it yields junctions with uniform properties over a large wafer area and good reproducibility from one fabrication batch to another. A standard deviation of the mean resistance values for a 5 mm × 5 mm test chip of 1 μm junctions is currently about 1 % [1.91]. This means that superconducting circuits have already reached the density of very large-scale integration, previously achieved only by semiconductor technology.

In spite of this progress, further improvement in the Josephson-junction tunneling quality remains an important task. In particular, this can be attained by reducing the Al overlayer thickness. At the same time, the drawback of the Nb/Al/AlO$_x$/Nb technology is that thin Nb films are granular. Then an unoxidized part of the Al overlayer tends to diffuse through the grain boundaries inside the Nb film [1.92] leading to degradation of the junction quality, especially in high-transparency junctions [1.93], and the need to use rather thick overlayers [1.94]. The solution to this problem can be the use of amorphous superconducting electrodes instead Nb ones. In the paper [1.88], related technique for obtaining such trilayer setups was described in detail. Obtained in such way sandwich-type Josephson tunnel junctions with α-MoGe electrodes demonstrated the potential of the technology for superconducting electronics.

The Josephson multilayers were deposited *in situ* on oxidized Si substrates at room temperature using DC magnetron sputtering from Mo$_{75}$Ge$_{25}$ and Al targets while the tunnel barrier was formed by thermal oxidation of an Al overlayer exploiting the well-known ability of aluminum to form spontaneously a self-healing surface oxide. For some devices, a thin (1.3 nm) Al layer was deposited on top of the bottom oxidized Al overlayer prior to the deposition of a top MoGe layer. It is known that such procedure can considerably improve the tunneling quality of the junctions, specifically, the characteristic voltage. The superconducting transition temperature T_c of the α-MoGe films was in the range of 6.5 K to 7.0 K, the surface roughness of a typical 160 nm thick α-MoGe layer used for the junction fabrication was 0.27 nm. For comparison, the surface roughness of a 120-nm thick Nb film, used as a base electrode in Nb/Al/AlO$_x$/Nb junctions, was 0.66 nm [1.88]. Therefore, in

amorphous films, the surface uniformity was better than that in Nb counterparts, see Fig. 1.9.
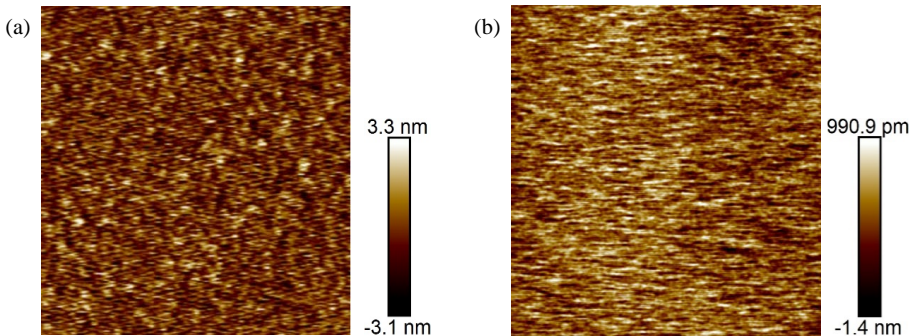

Fig. 1.9 – AFM images of a 120 nm thick Nb film (a) and 160 nm thick MoGe film (b) deposited onto oxidized Si substrates at room temperature. In both cases, the scanned area was 1.5 µm × 1.5 µm. Adapted from Fig. 1 in Ref. [1.88]

Below we present main results obtained for one of two types of devices studied in Ref. [1.88], namely, MoGe(160)/Al/AlO$_x$/(1.3)/Al(1.3)MoGe(80) where the numbers in parentheses are thicknesses of respective films in nm (that after Al/AlO$_x$ is the initial thickness of the Al overlayer before oxidation). The oxidation exposure dose was 31 mTor × min. Josephson devices with lateral dimensions of 10 µm × 10 µm and 5 µm × 5 µm were formed using optical lithography and reactive ion etching, They were characterized in a liquid He transport Dewar for measurements at 4.2 K, and in a Quantum Design MPMS cryostat at various temperatures. Typical current-voltage characteristics (*I–V* curves) are shown in Fig. 1.10. For comparison, we demonstrate also typical *I–V* curve taken at 4.2 K for a Nb(120)/Al/AlO$_x$/(8.4)/Al(1.3)Nb(70) junction that was fabricated with an oxidation dosage of 326 mTorr × min. Let us turn attention to the fact that in the Nb-based junctions, a considerably thicker Al overlayer was needed for obtaining appreciable tunneling quality.

Notice also that, even at lower oxidation dosages, resistance of the MoGe-based junctions is much higher than that in Nb-based junctions. For example, the resistance of the Nb/Al/AlO$_x$/Al/Nb junction fabricated with ten times the oxidation dosage (its *I–V* characteristic is shown in Fig. 1.10 as an inset) has almost half the resistance of the MoGe junction (the main panel in Fig. 1.10).
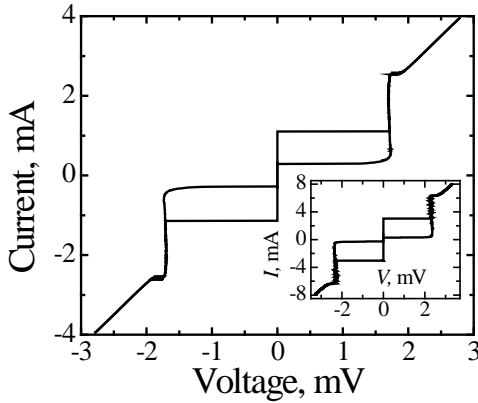
Fig. 1.10 – Main panel: Typical current-voltage characteristic
of the MoGe(160)/Al/AlO$_x$/(1.3)/Al(1.3)MoGe(80) junction. Inset: *I–V* curve
for a Nb(120)/Al/AlO$_x$/(8.4)/Al(1.3)Nb(70) junction. Critical temperature of the MoGe
films was 7.0 K, the temperature of the transport measurements was 4.2 K.
Adapted from Fig. 3 in Ref. [1.88]

The 'knee' structure seen slightly above the sum of the two energy gaps indicates the presence of an underoxidized aluminum interlayer between Nb and AlO$_x$ in the heterostructure and is the result of the proximity effect [1.95, 1.96]. It was obtained that the relative standard deviation of the 4.2 K resistance at 3 mV for seven Nb-based junctions on the same substrate was 0.008, which is slightly larger than that for the MoGe junctions. For the same thin Al overlayer in Nb junctions as in MoGe junctions, the spread of the junction resistances would be considerably larger. This is an indirect evidence that the uniformity of the tunnel barrier in the MoGe junctions surpasses that in Nb-based junctions. The latter statement is supported by recent progress in apprehending the process of the Al surface oxidation that was previously poorly understood [1.97–1.100]. Nguyen *et al.* [1.97] studied the mechanism of aluminum oxide formation using atomic resolution imaging in an environmental transmission electron microscope. The authors found that the oxidation occurs via island growth and proceeds atomic layer-by-layer into the aluminum. After sufficient time, a continuous ~1.5 nm thick semi-crystalline layer of the oxide covers the surface up to the saturation thickness, depending on the oxygen pressure (higher pressures result in faster initial oxidation rates and higher

critical oxide thicknesses) [1.99]. The aluminum oxide phase has been identi-
fied in many previous studies as spinel (γ) Al_2O_3 oxide which is known to
exhibit large structural differences due to variations in stoichiometry, tempera-
ture, pressure, and film thickness, see Ref. [1.97] and references therein. The
fully thickened film is amorphous and shows no long-range crystallinity [1.97].
These experimental findings were confirmed by fully *ab-initio* simula-
tions [1.98] aimed at understanding the thermodynamic driving force behind
the initial choice to grow in an amorphous phase or a crystalline phase (either
the corundum (α) or spinel (γ) structures) for the aluminum oxide surface layer
growing on a crystalline Al substrate.

For the Josephson multilayered junctions with higher barrier transparency
comparing to that shown in Fig. 1.10, the temperature effect on the current-
voltage characteristics was studied in the range of temperatures from 2.6 K to
the critical value T_c about 7.0 K [1.88]. A set of current-voltage characteristics
for a representative device, at 2.6, 3.0, 4.0, 4.5, 5.0, 5.5, 6.0, and 6.5 K, is
shown in Fig. 1.11. In these measurements, magnetic fields of 120–160 G
were applied to suppress the Josephson current. The product of the junction
resistance in the normal state $R_N = 0.6$ Ohm, and the subgap current $I^*(V^*)$ at
the voltage bias $V^* = \Delta/e$, where Δ is an *apparent* energy gap, is shown in
Fig. 1.12 as a function of temperature for three nominally identical junctions
(scattered plots).

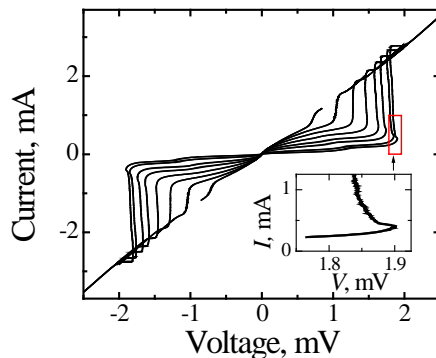Fig. 1.11 – Main panel: A set of current-voltage characteristics for a
MoGe(160)/Al/AlO$_x$/(1.3)/Al(1.3)MoGe(80) junction measured at 2.6, 3.0, 4.0, 4.5, 5.0,
5.5, 6.0, and 6.5 K. Magnetic field of 120–160 G was applied to suppress the Josephson
current. The arrow shows a step associated with the flux flow. Inset: zoomed-in portion
of the *I-V* curve for 2.6 K, marked by a red rectangle. Adapted from Fig. 4 in Ref. [1.88]

The subgap current vs temperature dependence presents further confirmation of high quality tunnel barriers in the Josephson junctions discussed. Fig. 1.11 exhibits a rapid decrease of the subgap current as the temperature goes down. For the curves measured at 6.0 and 6.5 K, the applied magnetic field was 160 G. However, even in such a field, the DC component of the AC Josephson current was not completely suppressed at voltage biases above that indicated by the vertical arrow. The Josephson current manifests itself as a smeared step, whose voltage position depends on the field. This step should not be confused with the step related to the subharmonic energy gap structure that is usually associated with the multiple Andreev reflections. Fig. 1.12 demonstrates the temperature dependence of the product $I*R_N$ as explained above. Current-voltage curves were calculated using the standard expression for the tunnel current between two identical superconductors: [1.101, 1.102]:

$$I(V,T)R_N = \frac{1}{e}\int_{-\infty}^{\infty} d\varepsilon N_s(\varepsilon - eV, T)N_s(\varepsilon, T)[f(\varepsilon - eV, T) - f(\varepsilon, T)], \quad (1.5)$$

where $N_s(\varepsilon, T) = \text{Re}\left\{\varepsilon / \sqrt{\varepsilon^2 - \Delta^2(T)}\right\}$ (1.4) is the normalized density of states in the superconducting electrode (the energy ε is measured from the Fermi level), $f(\varepsilon, T)$ is the Fermi distribution function, and $\Delta(T)$ was assumed to follow the conventional BCS dependence. Zero-temperature energy gap $\Delta_0 \equiv \Delta(0) = 1.14$ meV was found from the same BCS curve using the values $\Delta(4.2 \text{ K}) = 1.03$ meV and $T_c = 7$ K. Note that the obtained ratio $2\Delta_0/k_BT_c = 3.77$ is in agreement with that found by Tashiro *et al.* [1.103]. It is slightly larger than the BCS weak-coupling limit $2\Delta_0/k_BT_c = 3.52$ indicating moderate electron-phonon coupling in the amorphous α-MoGe superconductor.

In Fig. 1.11, one can see also a backward trend in the current-voltage characteristiucs at the gap-sum voltage, especially pronounced at lower temperatures. For example, the inset in Fig. 1.11 shows on a magnified scale a segment of the I–V curve near the voltage bias of $2\Delta/e$ outlined by the red dashed rectangle in the main panel for the curve measured at 2.57 K. A similar feature has been observed previously in a number of experiments involving tunnel junctions made of different superconducting materials and was associated with the gap suppression and formation of a nonequilibrium inhomogeneous state in superconducting films due to self-injection of quasiparticles [1.104].
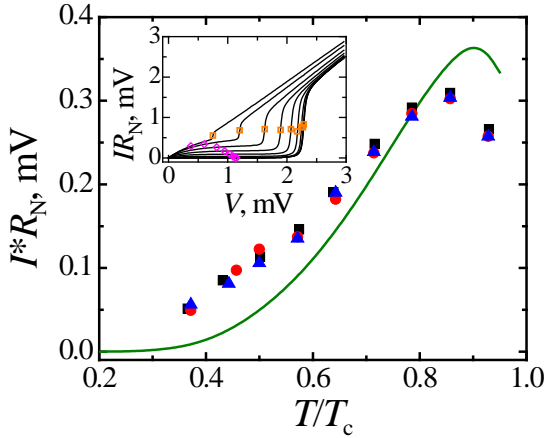
Fig. 1.12 – Main panel: Temperature dependence of the product I^*R_N, where the current I^* is measured at a voltage bias of $\Delta(T)/e$ ($\Delta(T)$ is an *apparent* energy gap) for three nominally identical MoGe(160)/Al/AlO$_x$/(1.3)/Al(1.3)MoGe(80) junctions (scattered plots). The solid line shows the theoretical dependence for an ideal tunnel junction with the same resistance as that of the measured junctions and $\Delta(0) = 1.14$ meV for both electrodes. Inset: a set of current-voltage characteristics calculated for an ideal tunnel junction at $T/T_{c=}$ 0.95, 0.9, 0.8, 0.7, 0.6, 0.5, 0.4, 0.3, 0.2, and 0.1 (curves from left to right, respectively). Orange squares denote voltages corresponding to $2\Delta(T)$. Magenta diamonds indicate current levels I^* corresponding to $\Delta(T)/e$ used for calculating the curve theoretically expected in the main panel. Adapted from Fig. 5 in Ref. 1.88

Since the effect of the gap suppression due to the excess quasiparticles, N_{exc}, created by the injection rate, I_0, may be important in some applications [1.105, 1.106], we have to analyze this feature in more detail. In the simplest case, $N_{exc} \equiv N(I_0) - N_T = I_0\tau_\varepsilon$, where N_T is the thermal-equilibrium number density of quasiparticle excitations, the injection rate I_0 is the number of quasiparticles injected into a unit volume per second, and τ_ε is the quasiparticle relaxation time [1.107]. Let us now compare the impact of the same I_0 on the energy gap suppression $\delta\Delta$ in Nb and amorphous MoGe electrodes. In a nonequilibrium state, when the distribution function of excess quasielectron excitations $n_{exc}(\varepsilon) \neq 0$, the gap Δ can differ from its thermodynamic value Δ_0. For the "narrow" distribution function $n_{exc}(\varepsilon)$ in the S film ($\Delta \leq \varepsilon \leq \Delta + \delta\Delta$; $\delta\Delta << \Delta$), we get the following relation for a relative gap suppression $\eta_\Delta(n) \equiv [\Delta(0) - \Delta(n)]/\Delta(0)$ in a conventional BCS superconductor [1.108]:

35

$$\eta_\Delta(n) \approx 2\overline{n} = \int\limits_\Delta^{\omega_D} \frac{2\varepsilon n_{exc}(\varepsilon)}{\Delta\sqrt{\varepsilon^2 - \Delta^2}} d\varepsilon,\tag{1.6}$$

where ω_D is the Debye energy. The excess quasiparticle concentration $\overline{n}$ is proportional to the ratio of $N_{exc}/N(0)$ where $N(0)$ is the single-spin density of states at the Fermi level [1.107].

Therefore, we can compare the effect of the same injection intensity I_0 in α-MoGe and Nb as follows:

$$\frac{\eta_\Delta^{MoGe}}{\eta_\Delta^{Nb}} \cong \frac{\tau_\varepsilon^{MoGe} N^{Nb}(0)}{\tau_\varepsilon^{Nb} N^{MoGe}(0)}.\tag{1.7}$$

The quasiparticle relaxation times τ_ε^{MoGe} and τ_ε^{Nb} depend on several factors such as the energy of excess quasiparticles, temperature, device size, environment, *etc.*, hence it is difficult to precisely estimate this ratio. However, the data [1.109] indicate that the relaxation processes in MoGe are as fast as in Nb. Specifically, the recombination time is $\tau_r = 3.5 \cdot 10^{-11}$ s for MoGe [1.109], whereas for Nb at $T/T_c \approx 0.5$ and for the quasiparticle energy $\varepsilon = 2\Delta$, τ_r is about $9 \cdot 10^{-11}$ s [1.110]. In realistic experimental situations, in addition to the recombination, other processes, such as electron-phonon interactions, are involved in the quasiparticle relaxation. Liang and Kunchur [1.109] measured quasiparticle relaxation time τ_ε in MoGe films. At $T/T_c \approx 0.6$ (which corresponds to our experimental situation), one can infer $\tau_\varepsilon^{MoGe} \approx 7 \cdot 10^{-10}$ s from the data [1.109] while for Nb the energy relaxation time $\tau_\varepsilon^{Nb} \approx 3 \cdot 10^{-11}$ s [1.111]. Note that according to [1.104], the quasiparticle energy relaxation and gap relaxation times coincide.

Using the latter data and the densities of states at $\varepsilon = 0$, $N^{MoGe}(0) = 6.4 \cdot 10^{21}$ eV^{-1}cm^{-3} [1.112] and $N^{Nb}(0) = 9 \cdot 10^{22}$ eV^{-1}cm^{-3} [1.113], we obtain from Eq. (1.7) that the ratio $\eta_\Delta^{MoGe}/\eta_\Delta^{Nb} > 300$ for *the same* injection rate I_0. This estimate indicates that a nonequilibrium quasiparticle population is much easier to realize in MoGe films than in Nb films. The data in Fig. 1.11 are consistent with the conclusion.

Fig. 1.13 exhibits experimental dependencies of the critical current I_c versus magnetic field H applied parallel to the layers of $5\,\mu m \times 5\,\mu m$

Josephson junctions with higher critical current density $j_c = 1.25$ kA/cm^2. The $I_c(H)$ characteristic of a representative device, recorded at 4.2 K, is close to the theoretical expectation described by the relation $I_c|\sin(\pi\Phi/\Phi_0)/\pi\Phi/\Phi_0|$ (solid red line), where Φ is the magnetic flux penetrating the junction, and $\Phi_0 = 2.07 \cdot 10^{-7}$ G·cm^2 is the flux quantum. A small deviation of the experimental $I_c(H)$ curve from theoretical one (in particular, a small asymmetry) is likely due to self-field effects and / or trapped flux [1.114, 1.115].

At the beginning of this subsection, we have mentioned ('strange' from the first insight) behavior of superconducting characteristics in amorphous metal alloys, also known as metallic glasses. Good superconductors change little by introducing disorder into them while those with relatively small T_c's can sharply raise their superconducting transition temperature. It is important that at low temperatures, many disordered materials have properties very similar to each other, including specific heat and thermal conductivity. Additionally, these properties differ significantly from those of related ordered crystals. Both features can be observed analyzing relaxation processes in glass-forming materials that usually occur as a two-stage process. First, there is a fast or 'β-relaxation' process, having a weakly temperature-dependent relaxation time (usually on the order of picoseconds), followed by the primary or 'α-relaxation' process with a relaxation time ranging from picoseconds to even minutes [1.116].
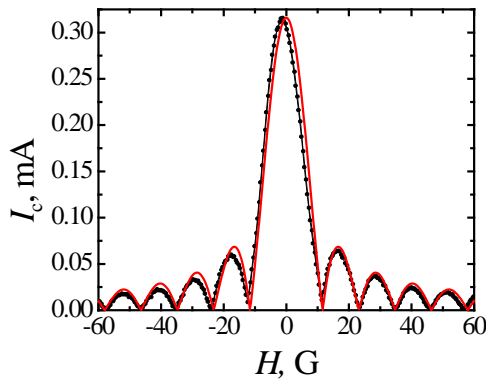

Fig. 1.13 – Ic vs H dependence of a 5 µm × 5 µm MoGe(160)/Al/AlOx/(1.3)/Al(1.3)MoGe(80) junctions at 4.2 K (black line + symbol plot). Red solid line is a theoretical dependence calculated using the period of the diffraction pattern $\delta H = 11.6$ G. Adapted from Fig. 6 in Ref. [1.88]

Furthermore, at a certain frequency range, amorphous materials exhibit excess of soft vibrational modes comparing to crystals, known as a 'boson peak' [1.117, 1.118], which shows up in the vibrational density of states $F(\omega)$ upon normalizing it by the Debye law ω^{d-1}: $F(\omega)/\omega^{d-1}$ (here d is the spatial dimensionality and ω is the angular frequency). Notice that $F(\omega)/\omega^{d-1} = $ const in the Debye's theory for crystals that successfully explained thermal behavior of ordered solids but cannot be straightforwardly applied to amorphous ones due to structural disorder and the absence of translational order, making it extremely challenging task.

The authors of Ref. [1.118] used sophisticated molecular dynamics computer simulations for revealing microscopic origins of the boson peak through numerical investigations of the dynamic structure factor of two-dimensional model glasses over a wide frequency–wavenumber range. They found that quasi-localized vibrations of string-like dynamical defects inside the material can move together, thus being important drivers of the anomalous observations in glassy systems: the boson peak, fast β-relaxation and slow structural relaxation. This conclusion has many important implications for both basic science and practical applications.

Typically, superconductivity in amorphous materials is strongly coupled, with the electron-phonon coupling parameter $\lambda > 1$ and the superconducting gap much larger than the BCS prediction, Presence of the boson peak means the need to transit from the oversimplified Bardeen-Cooper-Schrieffer model to the Eliashberg theory of strong-coupling phonon-mediated superconductivity [1.58, 1.119, 1.120]. This theory considers phonons as ballistic excitations while the largest part of the vibrational density of states for an amorphous material is formed by phonons, which propagate diffusively due to intense scattering promoted by disorder. Their Green's function

$$G_\lambda(\omega,k) = \frac{1}{\omega^2 - \Omega_\lambda^2(k) + i\omega\Gamma_\lambda(k)},\qquad(1.8)$$

takes into account propagating and diffusive damping (due to disorder-induced scattering) terms given by $\Omega_\lambda^2 = v_\lambda^2 k^2$ and $\Gamma_\lambda(k) = D_\lambda k^2$. Here v_λ and D_λ are the (dressed) speed of phonon propagation and the diffusion constant of the λ phonon branch, respectively, the subscript λ refers to either

longitudinal $\lambda = $ L or transverse $\lambda = $ T displacement fields, the diffusive form D_λ of the damping follows from related simulations performed over a broad range of k, see the references in Ref. [1.121]. Respectively, the Eliashberg electron-phonon interaction function equals to

$$\alpha^2 F(\vec{k},\vec{k}',\omega) \equiv N(\mu)\left|g_{\vec{k},\vec{k}'}\right|^2 B(\vec{k}-\vec{k}',\omega) \tag{1.9}$$

with the electronic density of states $N(\mu)$ at the chemical potential μ, the electron-boson matrix element $g_{\vec{k},\vec{k}'}$, and the spectral function

$$B_\lambda(\omega,k) = -\frac{1}{\pi}\operatorname{Im} G_\lambda(k,\omega+i\delta) \tag{1.10}$$

Using Eq. (1.8) we obtain [1.121]

$$B(\omega,k) = \frac{\omega\Gamma(k)}{\pi\left\{\left[\omega^2-\Omega^2(k)\right]^2+\omega^2\Gamma^2(k)\right\}} \tag{1.11}$$

Next, the Fermi-surface-averaged spectral function

$$\alpha^2 F(\omega) = \frac{1}{N(\mu)^2}\sum_{\vec{k},\vec{k}'}\alpha^2 F(\vec{k},\vec{k}',\omega)\delta(\varepsilon_{\vec{k}}-\mu)\delta(\varepsilon_{\vec{k}'}-\mu) \tag{1.12}$$

can be used for calculations of basic superconducting parameters as it was shown for crystalline samples in Ref. [1.58].

Using the Lorenzian form (1.11) to model the phonon spectral density, the authors of Ref. [1.121] went to some very important conclusions. First, they obtained (known from experiments) linear in frequency behavior of the Eliashberg function $\alpha^2 F(\omega)$ in the low-ω limit. Second, they found a non-monotonic dependence of the electron-phonon coupling parameter λ upon the disorder characteristic D (Fig. 1.14) with a maximum as a function of disorder, which monotonically grows upon increasing the speed of sound. Such tendency may be ascribed to two competing factors. On the one hand, the Lorentzian vibrational peak becomes bigger, which makes more phonon states accessible for pairing at low ω. On the other hand, upon increasing D further, the Lorentzian becomes broader and eventually shallower due to the term $\sim D^2$ in the denominator of the Lorentzian (1.11). These two opposite tendencies cause the presence of a peak in the dependence of λ on the diffusivity D., the position

of which shifts towards higher diffusion coefficients as the transverse speed of sound in a given material increases (a dashed line in Fig. 1.14) [1.121].
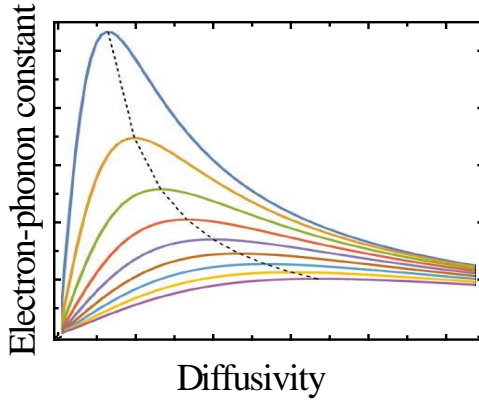

Fig. 1.14 – Schematic illustration of the electron-phonon coupling constant λ on the diffusivity D of transverse vibrational excitations for various values of the transverse speed of sound. The dashed line demonstrates an increase of the maximum position towards higher diffusion coefficients with increasing the speed of sound. The units for both axes are arbitrary. Adapted from Fig. 2 in Ref. [1.121]

The presence of a maximum in the λ-vs-D dependence shown in Fig. 1.14 means that the disorder effect on the main superconducting characteristics of a particular metal is controlled by its position on the λ-vs-D curve in the original crystalline state. If the initial superconductor has a relatively small value λ, then the disordering could enhance the electron-phonon coupling strength and we may observe the growth of T_c, as it happens, for example, in aluminum [1.122]. If, however, we are dealing with a superconductor with a sufficiently large λ, as in lead, then converting it to an amorphous state or adding impurities, most likely, will not lead to any noticeable effect or even cause slight weakening of the electron-phonon interaction.

These conclusions are well supported by comparing related experimental data for two model materials, for which the structural disorder can be varied continuously from the pure crystalline material limit (zero disorder) to the amorphous state (strong disorder) whether by means of alloying or by creating amorphous samples. Reconstructed Eliashberg functions feature two distinct peaks corresponding to transverse T (low frequency) and longitudinal L (high frequency) vibrational excitations. It is evident that, upon increasing the

degree of disorder, both peaks become much broader due to the increase of the phonons diffusivities D_T and D_L. This impact is more pronounced in the low-frequency region in agreement with the boson peak effect. Fig. 1.15 shows that in spite of the greater changes in the Eliashberg functions of Pb and related alloys in the low-frequency region, the disorder effect on T_c is much stronger in Al than in Pb, since, firstly, the crystalline aluminum has a significantly lower electron-phonon interaction strength, and secondly, due to the stronger broadening effect for longitudinal phonons.

The latter statement was also supported by experiments on nanostructured samples of Sn, a weekly coupled superconductor [1.26]. Relating their results to the bulk Sn phonon density of states, the authors [1.26] pointed out on a slightly increased number of low-energy phonon modes and a strong decrease in the number of high-energy phonon modes. It is important to note principal difference between Sn and Nb_3Sn thin films [1.122]. In Nb_3Sn, a strong coupling superconductor, with decreasing film thickness, a slight decrease in T_c was observed that was mainly caused by an electron confinement factor rather than phonon softening. Again, as in the case of Pb and Al discussed above, this difference arises due to lower electron-phonon interaction strength in the initial material.

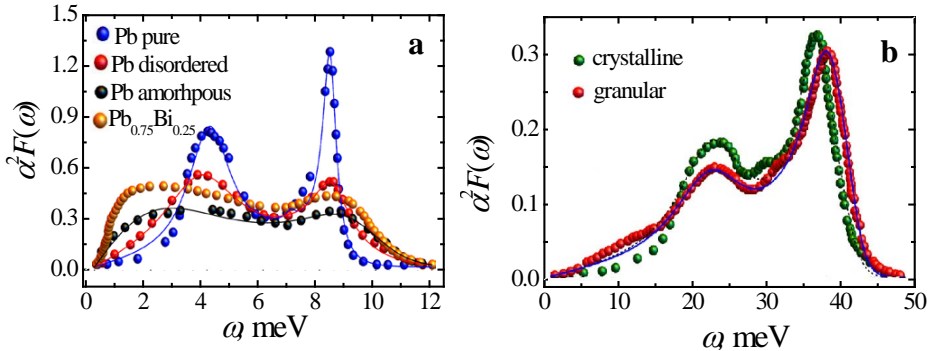Fig. 1.15 – Eliashberg electron-phonon interaction functions
α2F(ω) for Pb and PbBi alloy [1.123, 1.124] (a) and Al [100]
(b) reconstructed from tunneling experiments [1.123, 1.124] and [1.125], respectively.
Adapted from Figs. 3 and 5 in Ref. [1.121]

1.4 Superconducting quasicrystals and high-entropy alloys: intermediate compounds between crystalline and amorphous solids

We have discussed above two extreme states – crystalline and amorphous superconductors. According to the conventional crystallography, a crystal as a periodic arrangement of atoms with translational periodicity, leading to an infinitely extended crystal structure by aligning building blocks called unit cells [1.126]. The discovery of quasicrystals, stable solid-state materials without translational symmetry but having a high degree of order in their atomic arrangement (as manifested in the occurrence of sharp diffraction spots) led to a paradigm shift in materials science. Another feature that significantly distinguishes them from traditional crystals is the presence of a non-crystallographic rotational symmetry as fivefold symmetry in icosahedral quasicrystals. It was found that these specifically ordered materials exhibit anomalous electronic properties [1.127, 1.128], quantum criticality [1.129], etc. Superconductivity that emerged below T_c = 50 mK was observed for the first time in 2018 in an Al-Zn-Mg alloy [1.126]. In fact, it was the first quasicrystal exhibiting electronic long-range order. The authors revealed no difference between their samples and conventional weak-coupling superconductors. Nevertheless, during the last years the nature of superconductivity in such exotic materials has become the subject of intense theoretical debate, see Ref. [1.130] and references therein. In particular, the authors of Ref. [1.131] drew attention to the difference between the BCS theory and experiment [1.126] concerning the jump in the specific heat at the superconducting transition and explained it considering the attractive Hubbard model on the Penrose tiling as a simple theoretical model. However, from a theoretical point of view, there is no reason to believe that the mechanism of superconductivity in quasicrystals is fundamentally different from that in the BCS theory [1.130]. Undoubtedly, a further more detailed study of superconductivity in quasicrystals is needed.

Let us move on to more studied substances that also occupy an intermediate position between crystalline and amorphous superconductors, namely, to high-entropy alloys (HEA), a novel class of single-phase crystals with random solid solutions of five or more elements of a nearly equal composition [1.132]. These materials received a great amount of attention in recent years because

of their multi-elemental composition providing not only an enormous number of combinations for materials discovery but also a unique microstructure for property optimization [1.132, 1.133]. In particular, HEAs are known to exhibit intriguing electronic properties and superior mechanical properties such as a combination of high yield strength and ductility, high strength at high temperatures, strong resistance to corrosion and oxidation, outstanding thermal stability and so on, which are primarily derived from the high atomic disorder and near-equiatomic (5–35 at. %) mixing of different elements. The concept of this type of materials was originally proposed for simple crystal structures such as face-centered-cubic (fcc), body-centered-cubic (bcc), and hexagonal-closed packing (hcp) structures, all of which possess only one crystallographic site. Now this idea was implemented in many multi-site alloys beyond the structures mentioned above. Up to now there was not proposed a strict definition of HEAs. One of the definitions of HEA is that more than five elements with an atomic fraction of each element between 5 % and 35 % randomly occupy one crystallographic site [1.134]. The other definition uses the value of mixing entropy ΔS_{mix}, which is expressed as follows:

$$\Delta S_{\mathrm{mix}} = -R\sum_{i=1}^{n} c_i \ln c_i \,, \tag{1.13}$$

where n is the number of components, c_i is the atomic fraction and R is the gas constant. According to this equation, we classify low-entropy alloys as having an R value less than 0.69, medium-entropy alloys as having an R value between 0.69 and 1.60, and HEAs has having an R value of 1.60 or larger [1.135].

One of the attractive properties of HEAs is superconductivity [1.136, 1.137, 1.138]. In 2014, Koželj et $al.$ reported the synthesis of the first HEA superconductor $Ta_{0.34}Nb_{0.33}Hf_{0.8}Zr_{0.14}Ti_{0.11}$ with $T_c = 7.3$ K [1.37]. It was a type II superconductivity with the upper critical field $H_{c2}(0) = 82$ kOe. The measured physical properties were consistent with a conventional phonon-mediated superconductivity in the weak electron–phonon coupling limit. One of the salient features of this superconductor is that it exhibits extremely stable superconductivity under pressures up to 190 GPa. Later on, superconductivity was also observed in other HEAs, in particular, in CsCl-type Sc-Zr-Nb-Rh-Pd

and Sc-Zr-Nb-Ta-Rh-Pd alloys [1.139] and $TrZr_2$-type (Fe,Co,Ni,Rh,Ir)Zr_2 [1.140, 1.141]. Most interestingly, the superconducting (ScZrNb)$_{0.65}$[RhPd]$_{0.35}$ compound has $T_c \approx 9.7$ K and $H_{c2} \approx 100.7$ kOe, comparable to those characteristics of NbTi alloys [1.142]. From the basic viewpoint, HEA superconductors composed of transition metals can be regarded as an intermediate state between crystalline and amorphous materials, that is why their study is expected to shed light on the relationship between main parameters and the structural properties of superconductors.

Such an analysis based on experiments carried out on the Ta-Nb-Hf-Zr-Ti system, the most explored combination, was made by the authors of Ref. [1.137]. In particular, a large amount of data already available was considered from the perspective of an empirical Matthias rule [1.143] for T_c plotted as a function of the valence electron count per atom (VEC), see also the review [1.144]. This rule states that the superconducting critical temperature of transition-metal crystalline superconductors vs VEC dependence has the form of broad peak structures at specified VEC values. Indeed, in the compound (TaNb)$_{1-x}$(HfZrTi)$_x$ ($0.2 \leq x \leq 0.84$) where, depending on x, T_c ranges from 4.5 K to 8.0 K the maximum T_c is reached at the VEC value about 4.7 following the Matthias rule for crystalline transition-metal superconductors [1.145]. The curve of the VEC dependence of T_c for the HEAs lies between those of crystalline $4d$ metal solid solutions and amorphous $4d$ metals.

One of the high-impact results is the superconducting properties under high pressures. The (TaNb)$_{0.67}$(HfZrTi)$_{0.33}$ HEA superconductor showed a robust zero-resistance state up to 190.6 GPa [1.146]. This observation makes the HEAs promising candidates for superconducting materials working under extreme conditions. Another important conclusion to be noticed is the thermal annealing effect [1.147]. Long-term annealing induces short-range clustering of atoms, modifying the HEA microstructure. However, the superconducting properties are rather insensitive to such changes. There were reported first successful fabrications of (TaNb)$_{1-x}$(HfZrTi)$_x$ thin films using a magnetron sputtering method [1.148]. The highest $T_c = 6.8$ K was observed at $x = 0.43$ with VEC = 4.57. It was also found that the high-entropy state tends to stabilize the crystalline structure in spite of a rather large mismatch of atomic radii among constituent elements and therefore the high-entropy impact on

superconducting characteristics is correlated more to the structural properties than the electronic ones.

Let us now compare our results for Mo-Re crystalline alloys presented above with HEA compounds which are including molybdenum and rhenium as constituent elements. Ref. [1.149] reported related data for several hcp HEA superconductors based on a Mo-Re-Ru hcp alloy with the critical temperature T_c of 9.1 K. The highest T_c of 4.7 K was observed for a $Mo_{0.225}Re_{0.225}Ru_{0.225}Rh_{0.225}Ti_{0.1}$ compound. We can see that the superconducting transition temperature does not reach values typical for binary Mo-Re crystalline samples. This again indicates that the main benefit of the HEA samples is not their superconducting parameters but other superior properties arising due to high mixing entropy.
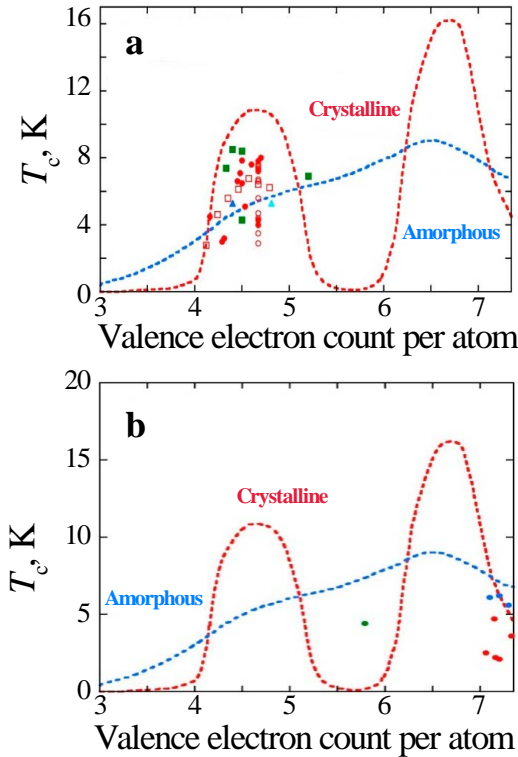

Fig. 1.16 – Superconducting transition temperatures Tc vs valence electron count per atom (VEC) dependence for bcc (left) and hcp and hcp-related (right) HEA superconductors compared with related dependences for crystalline 4d metal solid solutions and amorphous 4d metal superconductors. Adapted from Figs. 3 and 5 in Ref. [1.137]

The elemental choice for superconducting HEA compounds is now limited by Hf, Zr, Ti, Ta, Nb, Mo, V, Re, Ru and Rh with a VEC between 4 and 5 for bcc materials and neat 7 for hcp and hcp-related alloys. Due to it, the total number of HEA superconductors is rather small. Such state of affairs opens up a wide field of machine learning activities [1.150, 1.151]. In this regard, the most important, although perhaps not feasible in practice, task is to find a high-T_c HEA. As was argued by the authors of the overview [1.137], interest in HEA superconductors will grow due to the high degree-of-freedom of the HEA design. For example, it can relate HEA superconductors containing magnetic element(s) [1.137], eutectic [1.152], or gum-like [1.153] HEA superconducting compounds. In the first case, we may anticipate an exotic superconducting state originating from the large mixing entropy [1.137]. The change of the internal arrangement in eutectic HEAs could lead to the enhancement not only T_c but the critical current density as well since the microstructure of such material can be regarded as built-in multifilamentary one [1.137]. Gum metals. $i.\ e.$, metals which can be bent as gum [1.154] (for example, as-cast $Al_{0.05}Nb_{0.24}Ti_{0.4}V_{0.05}Zr_{0.26}$ [1.153]) are highly advantageous for making next-generation superconducting wires because their good superconducting properties are preserved even after cold rolling [1.137]. Last, the creation of new superconducting devices based on HEAs remains the most important task of this research line.

1.5 Conclusions

The interplay between disorder and superconductivity is a fascinating fundamental phenomenon in quantum physics. The famous Anderson's theorem states that conventional superconductors are insensitive to dilute nonmagnetic impurities. Even more, in the strong disorder regime far beyond the scope of the Anderson's theorem application, destruction of superconductivity and even superconductor–insulator transitions may take place [1.4]. That is why disorder-enhanced superconductivity is usually considered anomalous. However, our review shows that this effect is not so rare and manifests itself in a wide range of superconductors with different degrees of structural ordering. Notice that superconducting properties can be controlled not only by the overall density of impurities and / or defects but also by their spatial correlations [1.155].

To demonstrate the ubiquity of this phenomenon, we considered two limiting cases – a simplest binary alloy with a clear crystal structure (on the example of an alloy of molybdenum with rhenium) and an amorphous superconductor with a short-range ordering (on the example of a-MoSi and a-MoGe films). In the first case, a sharp increase in the critical temperature of the normal-to-superconducting transition was caused by modification of the electronic structure due to alloying, while in the second case, the main factor was the diffusive character of the phonon propagation promoted by increased number of scattering events. The best way to understand the interplay between the two sources of superconductivity enhancement would be careful and well-controlled study of an intermediate case, superconducting high-entropy alloys characterized by a multi-component alloy in which five or more elements are randomly occupying a crystallographic site. The materials research on the latter materials has just started recently, and we believe that it will bring new unexpected results. Solving the dilemma of crystalline and amorphous superconductors will give researchers a better understanding of chemical design principles for optimizing the key critical parameters in order to create novel superconductor-based devices.

1.6 References to chapter 1

1.1 Shalnikov A. Superconducting thin films. *Nature.* 1938. V. 142. P. 74.

1.2 Anderson P. W. Theory of dirty superconductors. *J. Phys. Chem. Solids.* 1959. V. 11. P. 26–30.

1.3 Abrikosov A. A., Gor'kov L. P. Superconducting alloys at finite temperatures. *J. Exp. Theor. Phys.* 1959. V. 38. P. 319–320.

1.4 Finkel'stein A. M. Suppression of superconductivity in homogeneously disordered systems. *Physica B*. 1994. V. 197. P. 636–648.

1.5 Fisher M. P. A. Quantum phase transitions in disordered two-dimensional superconductors. *Phys. Rev. Lett*. 1990. V. 65. P. 923–926.

1.6 Gupta A., Awana V., Samanta S., Kishan H., Narlikar A. Disordered superconductors. In: *Frontiers in Superconducting Materials*. Ed. By Narlikar A. V. Springer: Berlin, Heidelberg. 2009.

1.7 Alloul H., Bobroff J., Gabay M., Hirschfeld P. J. Defects in correlated metals and superconductors. *Rev. Mod. Phys.* 2009. V. 81. P. 45.

1.8 Sacépé B., Feigel'man M., Klapwijk T. M. Quantum breakdown of superconductivity in low-dimensional materials. *Nat. Phys*. 2020. V. 16. P. 734–746.

1.9 Petrović A. P., Ansermet D., Chernyshov D., Hoesch M., Salloum D., Gougeon P., Potel M., Boeri L., Panagopoulos C. A disorder-enhanced quasi-one-dimensional superconductor. *Nat. Commun.* 2016. V. 7. P. 1–10.

1.10 Lowe A., Kagalovsky V., Yurkevich I. V. Disorder-enhanced superconductivity in a quasi-one-dimensional strongly correlated system. *Phys. Rev. Res.* 2021. V. 3. P. 033059.

1.11 Zhao K., Lin H., Xiao X., Huang W., Yao W., Yan M., Xing Y., Zhang Q., Li Z.-X., Hoshino S., Wang J., Zhou S., Gu L., Bahramy M. S., Yao H., Nagaosa N., Xue Q.-K., Law K. T., Chen X., Ji S. H. Disorder-induced multifractal superconductivity in monolayer niobium dichalcogenides. *Nat. Phys.* 2019. V. 15. P. 904–910.

1.12 Leroux M., Mishra V., Ruff J. P., Claus H., Smylie M. P., Opagiste C., Rodie P., Kayani A., Gu G. D., Tranquada J. M., Kwok W.-K., Islam Z., Welp U. Disorder raises the critical temperature of a cuprate superconductor. *PNAS*. 2019. V. 116. P. 10691–10697.

1.13 Grassme R., Seidel P. The BCS Gap equation within the van Hove scenario of high-Tc superconductivity. *J. Supercond.* 1996. V. 9. P. 619–624.

1.14 Grassme R., Seidel P. An upper bound for the gap ratio of superconductors within the BCS theory for weak coupling. *Solid State Commun*. 1996. V. 98. P. 143–146.

1.15 Litak G. Van Hove singularity and superconductivity in a disordered Hubbard model. *Phys. Stat. Sol. B*. 2002. V. 229. P. 1427–1449.

1.16 Arnold G. B. Theory of thin proximity-effect sandwiches. II. Effects of s-wave elastic scattering. *Phys. Rev. B.* 1981. V. 23. P. 1171.

1.17 McMillan W. L. Tunneling model of the superconducting proximity effect. *Phys. Rev.* 1968. V. 175. P. 537.

1.18 Schopohl N., Scharnberg K. Tunneling density of states for the two-band model of superconductivity. *Solid State Commun.* 1977. V. 22. P. 371–374.

1.19 Golubov A. A., Mazin I. I. Effect of magnetic and nonmagnetic impurities on highly anisotropic superconductivity. *Phys. Rev. B.* 1997. V. 55. P. 15146.

1.20 Markowitz D., Kadanoff L. P. Effect of impurities upon critical temperature of anisotropic superconductors. *Phys. Rev.* 1963. V. 131. P. 563.

1.21 Belogolovskii M., Plecenik A., Grajcar M. Temperature effect on the quasiparticle spectrum of an impurity-doped superconductor with two separate electron groups. *Phys. Rev. B.* 2005. V. 72. P. 052508.

1.22 Mishra V. Effect of disorder on superconductivity in the presence of spin-density wave order. *Phys. Rev. B.* 2015. V. 91. P. 104501.

1.23 Bosworth D., Sahonta S. L., Hadfield R. H., Barber Z. H. Amorphous molybdenum silicon superconducting thin films. *AIP Adv.* 2015. V. 5. P. 087106.

1.24 Chen S. Z., Yang J. W., Peng T. Y., Chu Y. C., Yeh C. C., Hu I. F., Mhatre S., Lu Y.-J., Liang, C. T. Disorder-induced 2D superconductivity in a NbTiN film grown on Si by ultrahigh-vacuum magneton sputtering. *Supercond. Sci. Technol.* 2022. V. 35. P. 064003.

1.25 Scheurer M. S., Schmalian J. Topological superconductivity and unconventional pairing in oxide interfaces. *Nat. Commun.* 2015. V. 6. P. 1–10.

1.26 Houben K., Jochum J. K., Couet S., Menéndez E., Picot T., Hu M. Y., Zhao J. Y., Alp E. E., Vantomme A., Temst K., Van Bael M. J. The influence of phonon softening on the superconducting critical temperature of Sn nanostructures. *Sci. Rep.* 2020. V. 10. P. 5729.

1.27 Buckel W. Elektronenbeugungs-Aufnahmen von dünnen Metallschichten bei tiefen Temperaturen. *Z. Phys.* 1954. V. 138. P. 136–150.

1.28 Prakash O., Kumar A., Thamizhavel A., Ramakrishnan S. Evidence for bulk superconductivity in pure bismuth single crystals at ambient pressure. *Science.* 2017. V. 355. P. 52–55.

1.29 Bergmann G. Amorphous metals and their superconductivity. *Phys. Rep*. 1976. V. 27. P. 159–185.

1.30 Buzea C., Robbie K. Assembling the puzzle of superconducting elements: a review. *Supercond. Sci. Technol*. 2004. V. 18. P. R1.

1.31 Curzon A. E., Mascall A. J. Superconductivity in thin films of beryllium. *J. Phys. C.* 1969. V. 2. P. 382.

1.32 Gastiasoro M. N., Andersen B. M. Enhancing superconductivity by disorder. *Phys. Rev. B.* 2018. V. 98. P. 184510.

1.33 Gao M. C., Yeh J.-W., Liaw P. K., Zhang Y. High-entropy alloys. Springer: Cham. 2015.

1.34 Ye Y. F., Wang Q., Lu J., Liu C. T., Yang Y. High-entropy alloy: challenges and prospects. *Mater. Today*. 2016. V. 19. P. 349–362.

1.35 Senkov O. N., Miracle D. B., Chaput K. J., Couzinie J.-P. Development and exploration of refractory high entropy alloys – A review. *J. Mater. Res.* 2018. V. 33. P. 3092–3128.

1.36 George E. P., Raabe D., Ritchie R. O. High-entropy alloys. *Nat. Rev. Mater*. 2019. V. 4. P. 515–534.

1.37 Koželj P., Vrtnik S., Jelen A., Jazbec S., Jagličić Z., Maiti S., Feuerbacher M., Steurer W., Dolinšek J. Discovery of a superconducting high-entropy alloy. *Phys. Rev. Lett.* 2014. V. 113. P. 107001.

1.38 Mott N. F., Jones W. Theory of the properties of metals and alloys. Oxford University Press: Oxford. 1958.

1.39 Cossy-Favre A., Boyen H. G., Oelhafen P. Electronic structure of Nb_xMo_{100-x} solid solutions. *Phys. Rev. B*. 1995. V. 52. P. 16410.

1.40 Becker C., Hafner J. Electronic structure of crystalline and amorphous Nb_xMo_{1-x} alloys: Rigid versus rectangular bands. *J. Phys.: Condens. Matter*. 1995. V. 7. P. 5843.

1.41 Skorodumova N. V., Simak S. I., Abrikosov I. A., Johansson B., Vekilov Yu. Kh. Electronic topological transitions in Mo-Re random alloys. *Phys. Rev. B.* 1998. V. 57. P. 14673.

1.42 Anderson P. W. Localized magnetic states in metals. *Phys. Rev*. 1961. V. 124. P. 41.

1.43 Okada M., Rotenberg E., Kevan S. D., Schäfer J., Ujfalussy B., Stocks G. M., Genatempo B., Bruno E., Plummer E. W. Evolution of

the electronic structure in $Mo_{1-x}Re_x$ alloys. *New J. Phys.* 2013. V. 15. P. 093010.

1.44 Tarenkov V., Dyachenko A., Krivoruchko V., Shapovalov A., Belogolovskii M. Tunneling-spectroscopy evidence for two-gap superconductivity in a binary Mo-Re alloy. *J. Supercond. Nov. Magn.* 2020. V. 33. P. 569–574.

1.45 Tarenkov V., Shapovalov A., Boliasova O., Belogolovskii M., Kordyuk A. Two-band superconductivity in a Mo–Re alloy with an equal concentration of the components. *Low Temp. Phys.* 2021. V. 47. P. 101–105.

1.46 Lifshitz I. M. Anomalies of electron characteristics of a metal in the high pressure region *Sov. Phys. JETP.* 1960. V. 11. P. 1130–1135.

1.47 Lifshitz I. M., Azbel M. Ya., Kaganov M. I. Electron Theory of Metals. Consultant Bureau: New York. 1973.

1.48 Blanter Y. M., Kaganov M. I., Pantsulaya A. V., Varlamov A. A. The theory of electronic topological transitions. *Phys. Rep.* 1994. V. 245. P. 159–257.

1.49 Brandt N. B., Ginzburg N. I., Ignat'eva T. A., Lazarev B. G., Lazareva L. S., Makarov V. I. Influence of impurities on the effect of pressure on thallium. II. *J. Exp. Theor. Phys.* 1966. V. 22. P. 61–64.

1.50 Sharath Chandra L. S., Sundar S., Banik S., Ramjan S. K., Chattopadhyay M. K., Jha S. N., Roy S. B. Localization of electronic states resulting from electronic topological transitions in the $Mo_{1-x}Re_x$ alloys: A photoemission study. *J. Appl. Phys.* 2020. V. 127. P. 163906.

1.51 Davidson D. L., Brotzen F. R. Plastic deformation of molybdenum-rhenium alloy crystals. *Acta Metall.* 1970. V. 18. P. 463–470.

1.52 Smith H. G., Wakabayashi N., Mostoller M. Phonon anomalies in transition metals, alloys and compounds. In: Proceedings of Second Rochester Conference on Superconductivity in d- and f-band Metals. Ed. by Douglass D. H. Plenum Press: New York. 1976. P. 223–249.

1.53 Ignat'eva T. A. Electron localization during an electronic-topological transition in Mo-Re alloys. *Phys. Solid State.* 2007. V. 49. P. 403–412.

1.54 Sundar S., Chandra L. S., Chattopadhyay M. K., Roy S. B. Evidence of multiband superconductivity in the β-phase $Mo_{1-x}Re_x$ alloys. *J. Condens. Matter Phys.* 2015. V. 27. P. 045701.

1.55 Sundar S., Sharath Chandra L. S., Chattopadhyay M. K., Pandey S. K., Venkateshwarlu D., Rawat R., Ganesan V., Roy S. B. Strong electron–phonon coupling and multiband effects in the superconducting β-phase $Mo_{1-x}Re_x$ alloys. *New J. Phys.* 2015. V. 17. P. 053003.

1.56 Stewart G. R., Giorgi A. L. A search for strong coupling superconductivity. *Solid State Commun*. 1978. V. 28. P. 969–972.

1.57 Kim M. S., Skinta J. A., Lemberger T. R., Kang W. N., Kim H.-J., Choi E.-N., Lee S.-I. Reflection of a two-gap nature in penetration-depth measurements of MgB_2 film. *Phys. Rev. B*. 2002. V. 66. P. 064511.

1.58 Wolf E. L. Principles of electron tunneling spectroscopy, 2nd edn. Oxford University Press: New York. 2012.

1.59 Agraıt N., Yeyati A. L., Van Ruitenbeek J. M. Quantum properties of atomic-sized conductors. *Phys. Rep*. 2003. V. 377. P. 81–279.

1.60 Aono M., Hasegawa T. The atomic switch. *Proc. IEEE*. 2010. V. 98. P. 2228–2236.

1.61 Blonder G. E., Tinkham M., Klapwijk T. M. Transition from metallic to tunneling regimes in superconducting microconstrictions: Excess current, charge imbalance, and supercurrent conversion. *Phys. Rev. B*. 1982. V. 25. P. 4515.

1.62 Volkov S., Gregor M., Plecenik T., Zhitlukhina E., Belogolovskii M., Plecenik A. Above-gap differential conductance dips in superconducting point contacts. *Appl. Nanosci.* 2022. V. 12. P. 761–768.

1.63 Zhitlukhina E., Devyatov I., Egorov O., Belogolovskii M., Seidel P. Anomalous inner-gap structure in transport characteristics of superconducting junctions with degraded interfaces. *Nanoscale Res. Lett.* 2016. V. 11. P. 1–9.

1.64 Daghero D., Gonnelli R. S. Probing multiband superconductivity by point-contact spectroscopy. *Supercond. Sci. Technol.* 2010. V. 23. P. 043001.

1.65 Talvacchio J., Janocko M. A., Greggi J. Properties of evaporated Mo-Re thin-film superconductors. *J. Low Temp. Phys*. 1986. V. 64. P. 395–408.

1.66 Falge Jr R. L. Superconductivity of hexagonal beryllium. *Phys. Lett. A*. 1967. V. 24. P. 579–580.

1.67 Curzon A. E., Mascall A. J. Superconductivity in thin films of beryllium. *J. Phys. C*. 1969. V. 2. P. 382.

1.68 Granqvist C. G., Claeson T. Superconductivity of vapour quenched beryllium and beryllium-based alloys. Z. *Phys. B Con. Mat.* 1975. V. 20. P. 13–20.

1.69 Flasck J., Wood J., Edelstein A. S., Keem J. E., Missell F. P. Superconducting properties of amorphous transition metal alloys. *Solid State Commun*. 1982. V. 44. P. 649–652.

1.70 Bandyopadhyay S., Ganguly S. The effect of disorder on electronic structure and conducting properties of superconductors with various kinds of pairing symmetries. In *2019 International Conference on Opto-Electronics and Applied Optics (Optronix). IEEE.* 2019.

1.71 Komnik Y. F. Electrical properties of fine crystalline and amorphous metal films, obtained by low temperature condensation (Review). *Sov. J. Low Temp. Phys*. 1982. V. 8. P. 57–78.

1.72 Wright A. C. The great crystallite versus random network controversy: a personal perspective. *Int. J. Appl. Glass Sci*. 2014. V. 5. P. 31–56.

1.73 Mavračić J., Mocanu F. C., Deringer V. L., Csányi G., Elliott S. R. Similarity between amorphous and crystalline phases: the case of TiO_2. *J. Phys. Chem. Lett.* 2018. V. 9. P. 2985–2990.

1.74 Guillamón I., Suderow H., Fernández-Pacheco A., Sesé J., Córdoba R., De Teresa J. M., Ibarra M. R., Vieira S. Direct observation of melting in a two-dimensional superconducting vortex lattice. *Nat. Phys.* 2009. V. 5. P. 651–655.

1.75 Roy I., Dutta S., Roy Choudhury A. N., Basistha S., Maccari I., Mandal S., Jesudasan J., Bagwe V., Castellani C., Benfatto L., Raychaudhuri P. Melting of the vortex lattice through intermediate hexatic fluid in an a− MoGe thin film. *Phys. Rev. Lett*. 2019. V. 122. P. 047001.

1.76 Natarajan C. M., Tanner M. G., Hadfield R. H. Superconducting nanowire single-photon detectors: physics and applications. *Supercond. Sci. Technol*. 2012. V. 25. P. 063001.

1.77 Banerjee A., Baker L. J., Doye A., Nord M., Heath R. M., Erotokritou K., Bosworth D., Barber Z. H., MacLaren I., Hadfield R. H. Characterisation of amorphous molybdenum silicide (MoSi) superconducting thin films and nanowires *Supercond. Sci. Technol*. 2017. V. 30. P. 084010.

1.78 Miyahara K., Mukaida M., Tokumitsu M., Kubo S., Hohkawa K. Abrikosov vortex memory with improved sensitivity and reduced write current levels. *IEEE Trans. Magn.* 1987. V. 23. P. 875–878.

1.79 Holzman I., Ivry Y. Superconducting nanowires for single-photon detection: Progress, Challenges, and Opportunities. *Adv. Quantum Technol.* 2019. V. 2. P. 1800058.

1.80 Yu L. Superconducting nanowire single-photon detectors for quantum information. *Nanophotonics.* 2020. V. 9. P. 2673–2692.

1.81 Semenov A. D. Superconducting nanostrip single-photon detectors: some fundamental aspects in detection mechanism, technology and performance. *Supercond. Sci. Technol*. 2021. V. 34. P. 054002.

1.82 Lehtinen J. S., Kemppinen A., Mykkänen E., Prunnila M., Manninen A. J. Superconducting MoSi nanowires. *Supercond. Sci. Technol.* 2017. V. 31. P. 015002.

1.83 Mooij J. E., Nazarov Y. V. Superconducting nanowires as quantum phase-slip junctions *Nature Phys.* 2006. V. 2. P. 169–172.

1.84 Murphy A., Averin D. V., Bezryadin A. Nanoscale superconducting memory based on the kinetic inductance of asymmetric nanowire loops. *New J. Phys*. 2017. V. 19. P. 063015.

1.85 Singh A., Voltan S., Lahabi K., Aarts J. Colossal proximity effect in a superconducting triplet spin valve based on the half-metallic ferromagnet CrO_2. *Phys. Rev. X.* 2015. V. 5. P. 021019.

1.86 Dausy H., Nulens L., Raes B., Van Bael M. J., Van de Vondel J. Impact of kinetic inductance on the critical-current oscillations of nanobridge SQUIDs. *Phys. Rev. Appl.* 2021. V. 16. P. 024013.

1.87 Douçot B., Ioffe L. B. Physical implementation of protected qubits. *Rep. Prog. Phys.* 2012. V. 75. P. 072001.

1.88 Nevirkovets I. P., Belogolovskii M. A., Ketterson J. B. Josephson junctions based on amorphous MoGe: Prospects for use in superconducting electronics. *Supercond. Sci. Technol*. 2022 V. 35. P. 035008.

1.89 Wolf E., Arnold G., Gurvitch M., Zasadzinski J. Josephson junctions: History, devices, and applications. Pan Stanford Publ.: Singapore. 2017. Ch. 5.

1.90 Miller R. E., Mallison W. H., Kleinsasser A. W., Delin K. A., Macedo E. M. Niobium trilayer tunnel junctions with ultrahigh critical-current densities. *Appl. Phys. Lett*. 1993. V. 63. P. 1423–425.

1.91 Tolpygo S. K., Semenov V. K. Increasing integration scale of superconductor electronics beyond one million Josephson junctions. *J. Phys.: Conf. Ser*. 2020. V. 1559. P. 012002.

1.92 Kwo J., Wertheim G. K., Gurvitch M., Buchanan D. N. X-ray photoemission spectroscopy study of surface oxidation of Nb/Al overlayer structures. *Appl. Phys. Lett.* 1982. V. 40. P. 675–677.

1.93 Kleinsasser A. W., Rammo F. M., Bhushan M. Degradation of superconducting tunnel junction characteristics with increasing barrier transparency. *Appl. Phys. Lett.* 1993. V. 62. P. 1017–1019.

1.94 Belogolovskii M., Zhitlukhina E., Lacquaniti V., De Leo N., Fretto M., Sosso A. Intrinsically shunted Josephson junctions for electronics applications. *Low Temp. Phys*. 2017. V. 43. P. 756–765.

1.95 Seidel P., Richter J. Theoretical investigation of the current-voltage characteristics of superconducting niobium-lead tunnel junctions. *Phys. Stat. Solidi. B*. 1980. V. 98. P. 189–197.

1.96 Köhler H. J., Seidel P., Weber P., Blüthner K., Linke S., Berthel K. H. Influence of the niobium base electrode on the temperature dependence of the effective niobium energy gap and the critical Josephson current in Nb-NbO$_x$-Pb tunnel junctions. *Phys. Stat. Solidi. A*. 1981. V. 67. P. 497–503.

1.97 Nguyen L., Hashimoto T., Zakharov D. N., Stach E. A., Rooney A. P., Berkels B., Thompson G. E., Haigh S. J., Burnett T. L. Atomic-scale insights into the oxidation of aluminum. *ACS Appl. Mater. Interfaces*. 2018. V. 10. P. 2230–2235.

1.98 Aykol M., Persson K. A. Oxidation protection with amorphous surface oxides: thermodynamic insights from ab initio simulations on aluminum. *ACS Appl. Mater. Interfaces*. 2018. V. 10. P. 3039–3045.

1.99 Cai N., Zhou G., Mueller K., Starr D. E. Effect of oxygen gas pressure on the kinetics of alumina film growth during the oxidation of Al(111) at room temperature. *Phys. Rev. B*. 2011. V. 84. P. 125445.

1.100 Flototto D., Wang Z. M., Jeurgens L. P. H., Mittemeijer E. J. Intrinsic stress evolution during amorphous oxide film growth on Al surfaces. *Appl. Phys. Lett*. 2014. V. 104. P. 091901.

1.101 Svistunov V. M., D'yachenko A. I., Belogolovskii M. A. Elastic tunneling spectroscopy of single-particle excitations in metals. *J. Low Temp. Phys*. 1978. V. 31. P. 339–356.

1.102 Dynes R. C., Garno J. P., Hertel G. B., Orlando T. P. Tunneling study of superconductivity near the metal-insulator transition. *Phys. Rev. Lett*. 1984. V. 53. P. 2437–2440.

1.103 Tashiro H., Graybeal J. M., Tanner D. B., Nicol E. J., Carbotte J. P., Carr G. L. Unusual thickness dependence of the superconducting transition of α-MoGe thin films. *Phys. Rev. B.* 2008. V. 78. P. 014509.

1.104 Elesin V. F., Kopaev Yu. V. Superconductors with excess quasiparticles. *Sov. Phys. Usp*. 1981. V. 24. P. 116–141.

1.105 Nevirkovets I. P., Chernyashevskyy O., Prokopenko G. V., Mukhanov O. A., Ketterson J. B. Superconducting-ferromagnetic transistor. *IEEE Trans. Appl. Supercond*. 2014. V. 24. P. 1800506.

1.106 Nevirkovets I. P., Chernyashevskyy O., Prokopenko G. V., Mukhanov O. A., Ketterson J. B. Control of supercurrent in hybrid superconducting–ferromagnetic transistors. *IEEE Trans. Appl. Supercond*. 2015. V. 25. P. 1800705.

1.107 Parker W. H. Modified heating theory of nonequilibrium superconductors. *Phys. Rev. B.* 1975. V. 12. P. 3667–3672.

1.108 Gulian A., Dulal R., Teknowijoyo S., Chahid S. Dialogue on a superconducting laser operating via nonequilibrium inversed population. *Modern Phys. Lett. B*. 2020. V. 34. P. 2030005.

1.109 Liang M., Kunchur M. N. Vortex instability in molybdenum-germanium superconducting films. *Phys. Rev. B.* 2010. V. 82. P. 144517.

1.110 Kaplan S. B., Chi C., Langenberg D. N., Chang J. J., Jafarey S., Scalapino D. J. Quasiparticle and phonon lifetimes in superconductors. *Phys. Rev. B.* 1976. V. 14. P. 4854–4873.

1.111 Gershenson M. E., Gubankov V. N. Gap relaxation time in superconducting Nb films. *Physica.* 1981. V. 108B. P. 971–972.

1.112 Bezryadin A. Superconductivity in nanowires: Fabrication and quantum transport, Wiley-VCH: Weinheim. 2013.

1.113 Gladstone G., Jensen M. A., Schrieffer J. R. Superconductivity in the transition metals: Theory and experiment. In: *Superconductivity*. Vol. 2. Ed. by Parks R. D. M. Dekker: New York. 1969. Ch. 13.

1.114 Barone A., Paterno G. Physics and applications of the Josephson effect. Wiley: *Hoboken*. 1982.

1.115 Enpuku K., Yoshida K., Hamasaki K., Irie F. Effects of microshorts on current-voltage characteristics of Josephson tunnel junctions. *JJAP*. 1981. V. 20. P. 265.

1.116 Kojima S., Sato H., Yosihara A. Light scattering of supercooled propylene glycol. *J. Phys.: Condens. Matter*. 1997. V. 9. P. 10079.

1.117 Nakayama T. Boson peak and terahertz frequency dynamics of vitreous silica. *Rep. Prog. Phys.* 2002. V. 65. P. 1195.

1.118 Hu Y. C., Tanaka H. Origin of the boson peak in amorphous solids. *Nat. Phys*. 2022. P. 1–9.

1.119 Combescot R. Strong-coupling limit of Eliashberg theory. *Phys. Rev. B.* 1995. V. 51. P. 11625–11634.

1.120 Marsiglio F. Eliashberg theory: A short review. *Ann. Phys.* 2000. V. 417. P. 168102.

1.121 Baggioli M., Setty C., Zaccone A. Effective theory of superconductivity in strongly coupled amorphous materials. *Phys. Rev. B.* 2020. V. 101. P. 214502.

1.122 Pettit R. B., Silcox J. Film structure and enhanced superconductivity in evaporated aluminum films. *Phys. Rev. B.* 1976. V. 13. P. 2865–2872.

1.123 Knorr K., Barth N. Electron tunneling into disordered thin films. *J. Low Temp. Phys*. 1971. V. 4. P. 469–484.

1.124 Bergmann G., Rainer D. The sensitivity of the transition temperature to changes in $\alpha^2F(\omega)$. *Z. Phys*. 1973. V. 263. P. 59–68.

1.125 Dayan M. Tunneling measurements on crystalline and granular aluminum. *J. Low Temp. Phys*. 1978. V. 32. P.643.

1.126 Kamiya K., Takeuchi T., Kabeya N., Wada N., Ishimasa T., Ochiai A., Deguchi K., Imura K., Sato N. K. Discovery of superconductivity in quasicrystal. *Nat. Commun.* 2018. V. 9. P. 1–8.

1.127 Kimura K., Iwahashi H., Hashimoto T., Takeuchi S., Mizutani U., Ohashi S., Itoh G. Electronic properties of the single-grained icosahedral phase of Al–Li–Cu. *J. Phys. Soc. Japan.* 1989. V. 58. P. 2472–2481.

1.128 Mizutani U., Sakabe Y., Shibuya T., Kishi K., Kimura K., Takeuchi S. Electron transport properties of thermodynamically stable Al-Cu-Ru icosahedral quasicrystals. *J. Phys. Condens. Matter.* 1990. V. 2. P. 6169.

1.129 Deguchi K., Matsukawa S., Sato N.K., Hattori T., Ishida K., Takakura H., Ishimasa T. Quantum critical state in a magnetic quasicrystal. *Nat. Mater.* 2012. V. 11. P. 1013–1016.

1.130 Liu Y. B., Hao J. J., Zhang Y., Cao Y., Chen W. Q., Yang F. Cooper instability and superconductivity of the Penrose lattice. *Sci. China Phys. Mech.* 2022. V. 65. P. 1–11.

1.131 Takemori N., Arita R., Sakai S. Physical properties of weak-coupling quasiperiodic superconductors. *Phys. Rev. B.* 2020. V. 102. P. 115108.

1.132 Zhang Y., Zuo T., Tang Z., Gao M. C., Dahmen K. A., Liaw P. K., Lu Z. Microstructures and properties of high-entropy alloys. *Prog. Mater. Sci.* 2014. V. 61. P. 1–93.

1.133 Miracle D. B., Senkov O. N. A critical review of high entropy alloys and related concepts. *Acta. Mater.* 2017. V. 122. P. 448–511.

1.134 Yeh J.-W., Chen S.-K., Lin S.-J., Gan J.-Y., Chin T.-S., Shun T.-T., Tsau C.-H., Chang S.-Y. Nanostructured high-entropy alloys with multiple principal elements: Novel alloy design concepts and outcomes. *Adv. Eng. Mater.* 2004. V. 6. P. 299–303.

1.135 Otto F., Yang Y., Bei H., George E. P. Relative effects of enthalpy and entropy on the phase stability of equiatomic high-entropy alloys. *Acta Mater.* 2013. V. 61. P. 2628–2638.

1.136 Sun L., Cava R. J. High-entropy alloy superconductors: Status, opportunities, and challenges. *Phys. Rev. Mater.* 2019. V. 3. P. 090301.

1.137 Kitagawa J., Hamamoto S., Ishizu N. Cutting edge of high-entropy alloy superconductors from the perspective of materials research. *Metals.* 2020. V. 10. P. 1078.

1.138 Kitagawa J., Ishizu N., Hamamoto S. Materials research on high-entropy alloy superconductors. In: *Advances in High-Entropy Alloys-*

Materials Research, Exotic Properties and Applications. IntechOpen: London. 2021.

1.139 Stolze K., Tao J., von Rohr F. O., Kong T., Cava R. J. Sc–Zr–Nb–Rh–Pd and Sc–Zr–Nb–Ta–Rh–Pd high-entropy alloy superconductors on a CsCl-type lattice. *Chem. Mater.* 2018. V. 30. P. 906–914.

1.140 Mizuguchi Y., Kasem M. R., Matsuda T. D. Superconductivity in CuAl$_2$-type Co$_{0.2}$Ni$_{0.1}$Cu$_{0.1}$Rh$_{0.3}$Ir$_{0.3}$Zr$_2$ with a high-entropy-alloy transition metal site. *Mater. Res. Lett.* 2021. V. 9. P. 141–147.

1.141 Kasem M. R., Yamashita A., Goto Y., Matsuda T. D., Mizuguchi Y. Synthesis of high-entropy-alloy-type superconductors (Fe, Co, Ni, Rh, Ir) Zr$_2$ with tunable transition temperature. *J. Mater. Sci.* 2021. V. 56. P. 9499–9505.

1.142 Charifoulline Z. Residual resistivity ratio (RRR) measurements of LHC superconducting NbTi cable strands. *IEEE Trans. Appl. Supercond*. 2006. V. 16. P. 1188–1191.

1.143 Matthias B. T. Empirical relation between superconductivity and the number of valence electrons per atom. *Phys. Rev*. 1955. V. 97. P. 74–76.

1.144 Hott R., Kleiner R., Wolf T., Zwicknagl G. Review on superconducting materials. In: Applied Superconductivity. Handbook on Devices and Applications. V. 1. Ed. P. Seidel. Wiley-VCH: Weinheim. P. 26–48.

1.145 von Rohr F., Winiarski M. J., Tao J., Klimczuk T., Cava R. J. Effect of electron count and chemical complexity in the Ta-Nb-Hf-Zr-Ti high-entropy alloy superconductor. *Proc. Natl. Acad. Sci. USA*. 2016. V. 113. P. E7144–E7150.

1.146 Guo J., Wang H., von Rohr F., Wang Z., Cai S., Zhou Y., Yang K., Li A., Jiang S., Wu Q., Cava R. J., Sun L. Robust zero resistance in a superconducting high-entropy alloy at pressures up to 190 GPa. *Proc. Natl. Acad. Sci. USA*. 2017. V. 114. P. 13144–13147.

1.147 Vrtnik S., Koželj P., Meden A., Maiti S., Steurer W., Feuerbacher M., Dolinšek J. Superconductivity in thermally annealed Ta-Nb-Hf-Zr-Ti high-entropy alloys. *J. Alloys Compd*. 2017. V. 695. P. 3530–3540.

1.148 Zhang X., Winter N., Witteveen C., Moehl T., Xiao Y., Krogh F., Schilling A., von Rohr F. O. Preparation and characterization of high-entropy alloy (TaNb)$_{1-x}$(ZrHfTi)$_x$ superconducting films. *Phys. Rev. Res*. 2020. V. 2. P. 013375.

1.149 Lee Y.-S., Cava R. J. Superconductivity in high and medium entropy alloys based on MoReRu. *Phys. C*. 2019. V. 566. P. 1353520.

1.150 Islam N., Huang W., Zhuang H. L. Machine learning for phase selection in multi-principal element alloys. *Comput. Mater. Sci*. 2018. V. 150. P. 230–235.

1.151 Li Y., Guo W. Machine-learning model for predicting phase formations of high-entropy alloys. *Phys. Rev. Mater*. 2019. V. 3. P. 095005.

1.152 Lu Y., Dong Y., Guo S., Jiang L., Kang H., Wang T., Wen B., Wang Z., Jie J., Cao Z., Ruan H., Li T. A promising new class of high-temperature alloys: Eutectic high-entropy alloys. *Sci. Rep*. 2015. V. 4. P. 6200.

1.153 Zherebtsov S., Yurchenko N., Panina E., Tikhonovsky M., Stepanov N. Gum-like mechanical behavior of a partially ordered $Al_5Nb_{24}Ti_{40}V_5Zr_{26}$ high entropy alloy. *Intermetallics*. 2020. V. 116. P. 106652.

1.154 Yuan S., Lin N., Zeng Q., Zhang H., Wu Y. Recent advances in gum metal: Synthesis, performance and application. *Crit. Rev. Solid State Mater. Sci*. 2022. P. 1–32.

1.155 Neverov V. D., Lukyanov A. E., Krasavin A. V., Vagov A., Croitoru M. D. Correlated disorder as a way towards robust superconductivity. *Commun Phys*. 2022. V. 5. P. 177.

2. IRON-CONTAINING SUPERCONDUCTORS FROM THE VIEWPOINT OF CHEMISTS: THERMODYNAMIC STABILITY AND SUBSTITUTION LIMITS IN $La_{1-x}Ln_xFeAsO_{1-y}$ HIGH-TEMPERATURE SUPERCONDUCTORS (Ln = Ce–Er and Y)

E. Get'man[1], Yu. Oleksii[1,2], O. Mariichak[1], L. Ardanova[3], S. Radio[1]

Abstract

Within the framework of V. S. Urusov's crystal energy approach, we calculated mixing energies (interaction parameters), critical decomposition (stability) temperatures and built the domes of the decomposition of solid solutions of the following systems: $La_{1-x}Ce_xFeAsO_{0.65}$, $La_{1-x}Pr_xFeAsO_{0.65}$, $La_{1-x}Nd_xFeAsO_{0.65}$, $La_{1-x}Pm_xFeAsO_{0.65}$, $La_{1-x}Sm_xFeAsO_{0.65}$, $La_{1-x}Eu_xFeAsO_{0.65}$, $La_{1-x}Gd_xFeAsO_{0.65}$, $La_{1-x}Tb_xFeAsO_{0.65}$, $La_{1-x}Dy_xFeAsO_{0.65}$, $La_{1-x}Ho_xFeAsO_{0.80}$, $La_{1-x}Er_xFeAsO_{0.75}$, $La_{1-x}Y_xFeAsO_{0.80}$, $La_{1-x}Y_xFeAsO_{0.60}$, $La_{1-x}Sm_xFeAsO_{0.85}$, whose components are isostructural with ZrCuSiAs. It is shown that the magnitude of the mixing energy is determined mainly by the difference in sizes of the substituting structural units. The presented diagram makes it possible to predict the regions of thermodynamic stability of solid solutions, as well as the substitution limits (x) depending on the decomposition temperature (T_d) or the decomposition temperature according to the given substitution limits for limited series of solid solutions in all the above systems. Within the error of the method, our results do not contradict the available experimental data for $La_{1-x}Y_xFeAsO_{0.6}$ and $La_{1-x}Sm_xFeAsO_{0.85}$ systems and can be useful in choosing the ratio of components in «mixed» matrices, as well as the amount of an activator in high-temperature superconductors and effective magnetic materials.

✉ Dr. Serhii Radio

radio@donnu.edu.ua

[1] Vasyl' Stus Donetsk National University, 600-richchia vul. 21, 21021 Vinnytsia, Ukraine

[2] Université d'Angers, rue de Rennes 40 - BP 73532, 49035 Angers cedex 01, France

[3] Minnesota State University, Ford Hall 241, 56001 Mankato, Minnesota, USA

2.1 Introduction: Iron-based layered superconductors

Iron-based layered superconductors ($LnFePnO_{1-y}$, Ln – lanthanides, Pn – P or As) are Fe–containing compounds with a ZrCuSiAs-type of structure (tetragonal, *P4/nmm*) whose superconducting properties were discovered in 2006 for LaOFeP [2.1], and in 2008 for fluorine-doped LaFeAsO [2.2].

The structure, depicted in Fig. 2.1, consists of alternating Fe–As and La–O layers. Fe and O atoms sit at the center of slightly distorted As and La tetrahedra; the As tetrahedra are squeezed in the *z* direction. Since the radius of As atoms is much larger than the radius of a Fe atom, the Fe–As blocks are not atomically planar, in contrast to the Cu–O planes of cuprates. Fe atoms form a planar square lattice, with As atoms located above and below this plane, forming tetrahedra with Fe atoms in the center; the Fe–As distance is 2.41 Å, and the As–Fe–As angles are either 107.5^0 or 113.5^0. Fe atoms also bond to other Fe atoms in the plane, which are arranged on a square lattice at a distance of 2.85 Å [2.2–2.3]. Crystallochemical properties of LnFeAsO compounds are determined by the configuration of the outer electron shells: Fe(4s4p3d), As(4s4p), Ln(6s5d4f), O(2s2p). The formal valences of ions are as follows: La^{3+}, O^{2-}, Fe^{2+}, and As^{3-}. It is thought that these two layers are, respectively, positively and negatively charged, and that the La–O chemical bond in the La–O layer is ionic whereas the Fe–As has a predominantly covalent nature. Thus, the chemical formula may be expressed as $(La^{3+}O^{2-})^+(Fe^{2+}As^{3-})^-$. The conductive carriers, the concentration of which can be increased by substitution of the O^{2-} ion with a F^- ion, are confined two dimensionally in the $(FeAs)^-$ layers (Fig. 2.1) [2.4].
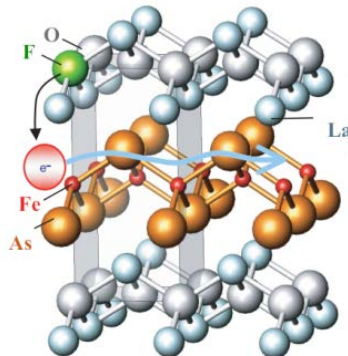

Fig. 2.1 – Crystal structure of LaFeAsO1–xFx. Adapted from Ref. [2.4]

Crystal lattice parameters and superconducting transition temperatures for some compounds LnFeAsO are given in Table 2.1.

Table 2.1. Maximal temperatures of superconducting transitions obtained by doping of LnFeAsO compounds.

LnFeAsO$_{1-y}$F$_y$ or LnFeAsO$_y$	T_c, K	a, Å	c, Å
LaFeAsO$_{0.95}$F$_{0.05}$ [2.2]	26	4.0320	8.7263
LaFeAsO [2.2]		4.0355	8.7393
LaFeAsO$_{0.89}$F$_{0.11}$ [2.4]	43 (at 4 GPa)	–	–
	9 (at 30 GPa)		
LaFeAsO$_{0.8}$F$_{0.2}$ [2.5]	27.5±0.2	4.030	8.716
LaFeAsO [2.5]		4.039	8.742
LaFeAsO$_{0.85}$ [2.6]	31.2	4.022	8.707
LaFeAsO [2.6]		4.033	8.739
CeFeAsO$_{0.84}$F$_{0.16}$ [2.7]	41	3.989	8.631
CeFeAsO [2.7]		3.996	8.648
CeFeAsO$_{0.88}$F$_{0.12}$ [2.8]	47 (at 1.8 GPa)	–	–
	4.5 (at 19 GPa)		
	<1.1 (at 26.5 GPa)		
CeFeAsO$_{0.85}$ [2.6]	46.5	3.979	8.605
CeFeAsO [2.6]		3.998	8.652
PrFeAsO$_{0.89}$F$_{0.11}$ [2.9]	52	3.967	8.561
PrFeAsO [2.9]		3.9853 (y = 0)	8.595
PrFeAsO$_{0.85}$ [2.6]	51.3	3.968	8.566
PrFeAsO [2.6]		3.985	8.600
NdFeAsO$_{0.89}$F$_{0.11}$ [2.10]	52	–	–
NdFeAsO$_{0.82}$F$_{0.18}$ [2.11]	50	–	–
NdFeAsO$_{0.85}$ [2.6]	53.5	3.943	8.521
NdFeAsO [2.6]		3.965	8.572
NdFeAsO$_{0.7}$F$_{0.3}$ [2.12]	46	–	–
SmFeAsO$_{0.90}$F$_{0.10}$ [2.13]	55	3.915	8.428
SmFeAsO [2.13]		3.933	8.495
SmFeAsO$_{0.85}$F$_{0.15}$ [2.14]	43	3.932	8.490
SmFeAsO [2.14]		3.940	8.501
SmFeAsO$_{0.85}$ [2.6]	55	3.897	8.407
SmFeAsO [2.6]		3.933	8.795
GdFeAsO$_{0.85}$ [2.15]	53.5	3.890	8.383
GdFeAsO [2.15]		3.903	8.453
GdFeAsO$_{0.8}$F$_{0.2}$ [2.15]	51.2	–	–
GdFeAsO$_{0.83}$F$_{0.17}$ [2.16]	36.6	4.001	8.650
TbFeAsO$_{0.85}$ [2.17]	42	3.889	8.376
TbFeAsO$_{0.9}$F$_{0.1}$ [2.18]	45.5	3.8634	8.333
TbFeAsO [2.18]		3.8632	8.322
TbFeAsO$_{0.8}$F$_{0.2}$ [2.18]	45.2	3.860	8.332
TbFeAsO$_{1-\delta}$ [2.19]	48.5	3.878	8.354
TbFeAsO [2.19]		3.898	8.404
DyFeAsO$_{0.9}$F$_{0.1}$ [2.18]	45.3	3.8425	8.2837
DyFeAsO$_{0.8}$F$_{0.2}$ [2.18]	43.0	3.8530	8.299
DyFeAsO$_{1-\delta}$ [2.19]	52.2	3.859	8.341
HoFeAsO$_{1-\delta}$ [2.19]	50.3	3.846	8.295
ErFeAsO$_{0.75}$ [2.20][a]	35.9	3.8198	8.2517
ErFeAsO$_{0.95}$ [2.20][a]	43.0	3.8238	8.2680
ErFeAsO$_{0.95}$ [2.20][a]	44.5	3.8219	8.2807
YFeAsO$_{1-\delta}$ [2.19]	46.5	3.842	8.303

[a] Nominal starting compositions; polycrystalline samples were synthesized by heating pellets with nominal compositions of ErFeAsO$_{1-y}$ (1−y = 0.75–0.95) sandwiched between pellets of LaFeAsO$_{0.8}$H$_{0.8}$ compositions at 1373 K under pressures of 5.5, 5.0 and 5.0 GPa, respectively [2.20].

Information on the influence of the synthesis time and synthesis temperature on the final temperature of the transition into the superconducting state is very limited in the literature. For the $HoFeAsO_{1-x}F_x$ system, such data was discussed in Ref. [2.21] (see Table 2.2).

Table 2.2. Synthesis conditions (all samples were synthesized at 10 GPa), refined lattice parameters (a, c) and volume (V), T_c, mass fractions, and superconducting volume fractions for $HoFeAsO_{1-x}F_x$ samples [2.21].

Sample	t_{synth}, hr	T_{synth}, °C	a, Å	c, Å	V, Å^3	T_c, K	Mass frac., %	Diamag. frac., %
1	2	1 150	3.8246	8.254	120.74	29.3	75	70
2	2	1 100	3.8272	8.2649	121.06	33.0	74	85
3	1	1 150	3.8258	8.264	120.96	33.2	73	76
4	3	1 100	3.8282	8.261	121.07	33.7	84	74
5	2	1 100	3.8282	8.2654	121.13	35.2	81	57
6	2	1 100	3.8297	8.270	121.30	36.2	58	46

Although all samples in Table 2.2 have the same starting composition, small variations in synthesis pressure and temperature result in a dispersion in x around the nominal 0.1 value for the $HoFeAsO_{1-x}F_x$ phase and corresponding variations in superconducting properties. T_c increases to a maximum value, $T_c(max)$, at the upper solubility limit of x in $LnFeAsO_{1-x}F_x$ systems [2.14], and this is consistent with the observation that the superconducting phases in samples 1, 3, and 4, which are heated at high temperatures or for longer times and so are likely to have a slightly lower F content, have lower T_c (an average value of 32.1 K) compared to other three samples with the average value $T_c = 34.8$ K, made under nominally identical "optimum" conditions. Sample 6 shows the highest $T_c = 36.2$ K and the lowest proportion of the diamagnetic fraction in the $HoFeAsO_{1-x}F_x$ phase. This demonstrates that the sample is at the upper limit of the superconducting composition range and so gives a realistic $T_c(max)$ for the $HoFeAsO_{1-x}F_x$ system [2.21].

Also of interest are systematic studies of the pressure effect on properties of the obtained materials. In Ref. [2.22], single-phase polycrystalline samples of oxygen-deficient oxypnictide superconductors $LnFeAsO_{0.7}$ (Ln = Sm, Gd, Tb, and Dy) were synthesized using high-pressure technique. It was found out that the synthesis pressure is a key parameter for synthesizing samples, in particular, for heavier lanthanides. It was established that the lattice parameters systematically decrease with the atomic number of Ln, reflecting the

shrinkage of Ln ionic radius: for the lighter Ln atoms (La, Ce, Pr, Nd), T_c increases monotonously with decreasing the lattice parameters from 26 K for La to 54 K for Nd, then stays at the constant value around 53 K in the case of the heavier lanthanides (Nd, Sm, Gd, Tb, and Dy) (see Fig. 2.2). Obtained results suggest the intimate relationship between the crystal structural parameters and superconductivity, as well as the possible existence of the inherent maximum of T_c located around 50 K in the LnFeAsO based materials [2.22].
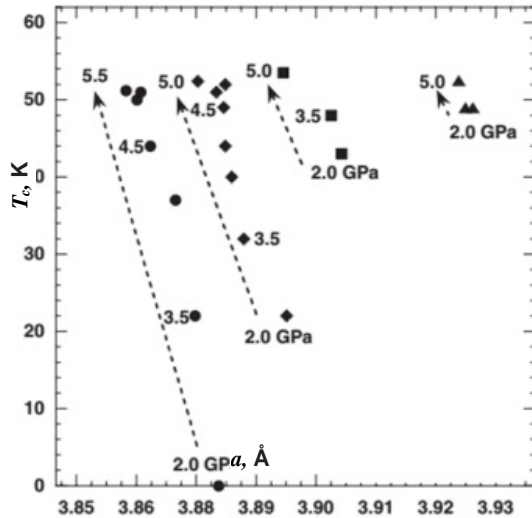

Fig. 2.2 – Relationships between T_c and a-axis lattice parameter for the samples with a nominal composition of LnFeAsO$_{0.7}$ (Ln = Sm(▲), Gd(■), Tb(♦), and Dy(●)) synthesized under various pressures ranging from 2.0 to 5.5 GPa. Adapted from Ref. [2.22]

Despite the great interest in high-temperature superconductors based on LnFeAsO$_{1-y}$F$_y$ and LnFeAsO$_y$ expressed in recent reviews [2.23–2.30] and monographs [2.31–2.33], the data on isomorphous substitutions of lanthanides in Ln positions in the LnFeAsO$_{1-y}$ structure are rather scarce.

The effect of replacing La atoms by Y atoms in the oxypnictide superconductor LaFeAsO$_{0.6}$ was studied in Ref. [2.34]. It has been found that the replacement of La^{3+} by smaller Y^{3+} in the La$_{1-x}$Y$_x$FeAsO$_{0.6}$ form leads to the decrease in lattice parameters, and superconducting transition temperature increases monotonically with increasing x up to 43.1 K at $x = 0.5$. Similar

results were obtained in the study of partial substitution of La for Y in the $La_{1-x}Y_xFeAsO_{0.85}F_{0.15}$ superconductor [2.35] that, up to $x = 0.70$, leads to the decrease in lattice parameters a and c of the structure by 1.8 % and 1.7 %, respectively. It was determined that 15 % F-doped samples reach a maximum critical temperature of 40.2 K for the 50 % yttrium substitution. In addition, in the mixed lanthanide compounds of $La_{1-x}Sm_xFeAsO_{0.85}$, the onset superconducting critical temperature was found to rise monotonically from 31.2 K to 55 K with increasing amount of Sm doping from $x = 0$ to 1 [2.36].

Using resistivity and magnetization studies the pressure effect on the superconducting transition temperature of Yb doped $Ce_{0.6}Yb_{0.4}FeAsO_{0.9}F_{0.1}$ has been investigated [2.37]. It has been established that increase in chemical pressure by substitution of smaller Yb^{3+} ions in place of Ce^{3+} ions results in a significant enhancement of T_C from 38 K (Yb free) to 47 K (40 % Yb), enhancement in T_C with external pressure has been observed for this compound up to a maximum value of $T_c = 48.7$ K at 1 GPa, beyond which T_c starts decreasing monotonously.

It is also of interest to study the replacement of three-charged lanthanide cations by ions with a larger charge that can lead to the creation of novel materials with a higher T_c. First studies in this direction showed encouraging results for $Tb_{0.8}Th_{0.2}OFeAs$ [2.38], $Gd_{0.8}Th_{0.2}OFeAs$ [2.39], and $Sm_{0.7}Th_{0.3}OFeAs$ [2.40] where values of $T_c = 52$–56 K were achieved.

2.2 Isomorphous substitutions in the LnFeAsO structure

Isomorphous substitutions of atoms in crystals attract the attention of researchers for the reason that many new inorganic materials (phosphors, semiconductors, ferroelectric, piezoelectrics, etc.) are created on the basis of not individual compounds, but solid solutions. This is due to the fact that the properties in the region of homogeneity regularly change depending on the composition. The properties of high-temperature superconductors (HTSCs) of the first generation based on barium cuprates and rare-earth elements (REEs) are the most studied, both in the case of individual compounds, for example [2.41–2.43], and solid solutions based on them when modified with other REEs [2.44–2.45]. At the same time, REE intersubstitutions for HTSCs with

a tetragonal structure of the ZrCuSiAs type, for which more than 150 representatives are known [2.46–2.47], have been hardly studied.

It is known that undoped LnFeAsO compounds are not superconductors [2.46]. However, those obtained at high pressures (from 2.0 to 5.5 GPa) with a lack of oxygen or with partial substitution of oxygen by fluorine do superconduct [2.34, 2.48]. Isomorphous substitution of lanthanum or iron cations with other cations can lead to an increase in the critical temperature [2.19, 2.48]. Therefore, the study of isomorphous substitutions in superconducting solid solutions is of current interest, as it has been argued in the first chapter above.

To the best of our knowledge, LnFeAsO-based solid solutions with partial REE substitution are described only for a limited number of systems: $La_{1-x}Y_xFeAsO_{0.6}$ ($x = 0.0$–0.5) [2.34], $La_{1-x}Sm_xFeAsO$ [2.47], and also for $Sm_{1-x/3}Sc_{x/3}FeAsO_{1-x}F_x$ ($x = 0.09$–0.27) [2.48]. $La_{1-x}Y_xFeAsO_{0.6}$ samples were synthesized by heating LaAs, YAs, Fe, and Fe_2O_3 at 1423 K for 2 h under the pressure of 2 GPa [2.34]. When x changes in the range from 0.0 to 0.4, the unit cell parameters in the $La_{1-x}Y_xFeAsO_{0.6}$ structure naturally decrease from $a = 4.029$ Å and $c = 8.729$ Å to $a = 3.992$ Å and $c = 8.652$ Å, correspondingly. In this case, the critical temperatures of the superconducting transition increase substantially. However, the experimental determination of substitution limits in this work is not entirely unambiguous. The cell parameters really change in the range of initial compositions x from 0.0 to 0.4, however, only samples with x from 0.0 to 0.1 are single-phase. Samples of initial compositions x from 0.2 to 0.5 consist of several phases that is explained by the fact that the compound of composition YFeAsO does not exist [2.34]. In this case, the $La_{1-x}Y_xFeAsO_{0.6}$ system should be considered multicomponent rather than pseudobinary, and the cell parameters can change in the mixed-phase region. The authors [2.34] believe that the designations they use for the compositions simply mean the nominal value and do not necessarily agree with the actual ones. However, there is another point of view: in Ref. [10] the YFeAsO compound is described and even the cell parameters are given. It is possible that equilibrium was not reached in Ref. [8] due to the fact that the interaction of the components was not completed, since the synthesis was carried out for only 2 h, or partial decomposition of the solid solution occurred when the samples were cooled after calcination.

Similarly, in the $Sm_{1-x/3}Sc_{x/3}FeAsO_{1-x}F_x$ system, as x changes in the range from 0.09 to 0.27, the unit cell parameters also regularly decrease, and the critical superconducting temperatures increase significantly [2.48]. At the same time, samples with $x \geq 0.12$ are also not single-phase, and the authors suggest that $x = 0.23$ is the substitution limit. Apparently, the substitution limit is approximate in this case as well. An increase in the critical temperature T_c can be promoted not only by the substitution of samarium for scandium but also by the substitution of oxygen for fluorine with an ionic radius smaller than that of oxygen.

In Ref. [2.36], the $La_{1-x}Sm_xFeAsO_{0.85}$ system with $x = 0, 0.1, 0.2, 0.3, 0.4,$ 0.6, 0.8, 0.9, 0.95 and 1.0 was synthesized at a final temperature of 1623 K for 2 h. Based on the phase composition and the change in cell parameters, an unlimited substitution of lanthanum for samarium was established in the x range from 0 to 1. In Ref. [2.47], for the same system, it was found that the values of the Ln—O and Ln—As interatomic distances also regularly decrease with increasing x in the entire range of compositions indicating the substitution of lanthanum by samarium. An increase in the transition temperature T_c is due to the compression of the crystal structure, which, in the case of isomorphous substitution by a smaller ion, is even called the «effect of chemical pressure» [2.47].

It should be also noted that the limits of isomorphous substitutions in solid solutions are significantly affected not only by the synthesis temperature but also by pressure. The data on the pressure effect on the critical decomposition (stability) temperature of solid solutions indicate that the pressure growth by 1 GPa leads to its increase by 20–150 degrees [2.49–2.50]. Also, the degree of the pressure influence on the miscibility of the system components depends on the temperature. Studies of solid solutions in the enstatite $Mg_2Si_2O_6$ – diopside $CaMgSi_2O_6$ system carried out at pressures of 5–40 kbar (0.5–4 GPa) and temperatures of 1173–1773 K showed that increasing pressure reduces the mutual miscibility only starting from 1473 K, while at 1173 K the effect of pressure is still very small. The same conclusion follows from the study of the solubility of calcium in olivines at different temperatures and pressures [2.49].

At present, one of the ways to search for HTSCs with desired properties is to study their dependence on the composition in the regions of the solid-

solution existence. At the same time, the physicochemical foundations of the synthesis of solid solutions, such as state diagrams and solubility regions of the $La_{1-x}Ln_xFeAsO_{1-y}$ systems, to the best of our knowledge, are almost not studied. Therefore, in particular, authors studying superconductors based on $LnFeAsO_{1-y}$ in most cases limit themselves by the properties of individual compounds rather than solid solutions.

At the same time, it is known [2.49–2.50] that solid solutions which are synthesized at high temperatures tend to decompose upon cooling that can lead to degradation of materials based on them, changes and irreproducibility of their properties. In this regard, before the synthesis of solid solutions and the study of their properties depending on the composition, it is desirable to know the limits of isomorphous substitutions depending on temperature and stability of solid solutions in the corresponding areas of the systems under synthesis, storage and intended operation conditions. Experimental determination of substitution limits with X-ray diffraction analysis (XRD) by annealing and hardening is complicated by the difficulty of achieving equilibrium at low temperatures due to the low diffusion rate in the solid phase and the possibility of partial decomposition of the solid solution during its quenching from high temperatures. In addition, XRD can be inefficient, in particular, for isostructural components with similar sizes of substituting structural units, in the cases of spinodal decomposition of a solid solution [2.49–2.50] or nanosized particles. In such cases, difficulties arise in determining the substitution limits by XRD, as was the case in the $La_{1-x}Y_xFeAsO_{0.6}$ [2.34] and $Sm_{1-x/3}Sc_{x/3}FeAsO_{1-x}F_x$ systems [2.48].

Insufficient information about substitution limits and stability regions of solid solutions forces researchers to choose the composition of matrices and modifying additives (dopants) either by analogy with related systems or by the «trial and error» method that can lead to excessive consumption of expensive reagents and an increase in the duration of reearch. Thus, for determining the substitution limits, it is rational to use not only experimental but also calculation methods, devoid of the above disadvantages. The aim of our work has been to predict the substitution limits and thermodynamic stability of solid solutions with a structure of the ZrCuSiAs type in a wide range of compositions and temperatures in $La_{1-x}Ln_xFeAsO_{1-y}$ systems with Ln = Ce–Er, and Y.

The choice of such systems was also due to the fact that LnFeAsO$_{1-y}$ super-conductors are perspective naterials for generating very strong magnetic fields [2.51].

2.3 Calculation method and initial data

In the general case, according to V. S. Urusov, the mixing energy (interaction parameter) Q which determines possibility and substitution limits, consists of three contributions due to the difference in the sizes of the substituting structural units, the degrees of ionicity of the chemical bond in the components, and the crystal structures of the components [2.49–2.50].

Since we are dealing with the intersubstitution of REE in groups of systems, both components of which are isostructural to ZrCuSiAs, the third contribution is equal to zero. The second contribution, according to [2.49–2.50], must be taken into account in cases where the electronegativity difference $\Delta\chi(Ln^{3+})$ of ions replacing each other is greater than 0.4. Since the value of this difference calculated by us does not exceed 0.111 (Table 1), the mixing energy is calculated using the formula [2.49–2.50]:

$$Q = 1000Cmnz_{m}z_{x}\delta^2 \text{ J/mol}, \tag{2.1}$$

where C is an empirical parameter calculated from the expression $C = 20(2\Delta\chi + 1)$ kJ [2.50] by the difference in the electronegativity of the cation and anion, taken from Ref. [2.52]. The electronegativity of the anion $\chi(AsO_{1-y})$ is estimated as the average of the electronegativity of arsenic and oxygen; $n = 6.8$ is the effective coordination number of the substituted structural unit for the LnFeAsO$_{1-y}$ structure calculated according to S. Batsanov [2.53], since in LnFeAsO$_{1-y}$ the REE cation is surrounded by four arsenic anions and four oxide anions located at two significantly different distances (for example, in the SmFe$_{0.92}$Co$_{0.08}$AsO structure they are equal to 3.277 and 2,2884 Å, respectively) [2.54]; m is the number of different structural units in the components calculated taking into account the peculiarities of the LnFeAsO$_{1-y}$, layered structure with alternating LnO$^+$ and FeAs$^-$ layers [2.46]. Since the substitution occurs only in the LnO$^+$ layers (the Ln—O and Ln—As distances decrease, while the Fe—As distances are constant [2.47]), iron cations are passive in isomorphous substitution and, therefore, in accordance

with Ref. [2.49] were not taken into account in the calculations: $m = 1 + 1 + (1 - y)$ (Table 2); z_m, z_x are moduli of charges of structural units, $z_m = 3$, $z_x = 2,5$ are average charges of oxygen and arsenic ions; δ is the relative difference in the sizes of substituting structural units (a size parameter) that was calculated taking into account the assisting rule [2.49] by crystalline ionic radii:

$$\delta = [(r(La^{3+}) - r(Ln^{3+}))]/[r(Ln^{3+}) + r(O^{2-})]. \qquad (2.2)$$

Crystalline ionic radii of REE were taken according to R. Shannon [2.55] for a coordination number of 7 closest to the effective coordination number of 6.8 according to S. Batsanov [2.53]. The Ln—O distances were taken equal to the sum of the crystalline ionic radii of the cations and the oxide anion: $r(Ln^{3+}) + r(O^{2-})$. The choice of the oxide anion as the common structural unit in calculating δ is due to the fact that it is located in the LnO^+ layer, in which substitution occurs. The crystalline ionic radius of oxygen was taken according to R. Shannon for a coordination number of 4. The accuracy of the calculation of the mixing energy according to the data [2.49] is $\pm$ 13 %.

Since the values of the dimensional parameters δ are less than 0.067 (Table 2), according to the recommendations [2.49–2.50], the critical decomposition temperatures of solid solutions were calculated in the approximation of regular solutions by the expression $T_{cr} = Q/2kN$, where k is the Boltzmann constant and N is the Avogadro number. The equilibrium decomposition temperature T_d was calculated from the given substitution limit x or the substitution limit x from the decomposition temperature, according to the Becker equation [2.56]:

$$- (1 - 2\,x)\,/\,\ln[x/(1 - x)] = kN \times T_d/Q. \qquad (2.3)$$

In the two cases, the Q value was taken in cal/mol [2.49–2.50].

2.4 Results and discussion

Some initial data and results of calculations of the mixing energy and critical decomposition temperatures T_{cr} are summarized in Tables 2.3–2.4.

Table 2.3. Values of electronegativity of cations $\chi(Ln^{3+})$, the average electronegativity of anions $\chi(As, O)$ and constants C calculated for $La_{1-x}Ln_xFeAsO_{1-y}$ solid solutions (Ln = Ce–Er, and Y)

Ln	1–y	$\chi(Ln^{3+})$	$\Delta\chi(Ln^{3+})$	$\chi(As,O)$	$\chi(As,O) - \chi(Ln^{3+})$	C, kJ
La	0.65	1.327	–	2.300	0.973	58.92
Ce	0.65	1.348	0.021	2.300	0.952	58.08
Pr	0.65	1.374	0.047	2.300	0.926	57.04
Nd	0.65	1.382	0.055	2.300	0.918	56.72
Pm	0.65	1.391	0.064	2.300	0.909	56.36
Sm	0.65	1.410	0.083	2.300	0.890	55.6
Eu	0.65	1.433	0.106	2.300	0.867	54.68
Gd	0.65	1.386	0.059	2.300	0.914	56.56
Tb	0.65	1.410	0.083	2.300	0.890	55.6
Dy	0.65	1.426	0.099	2.300	0.874	54.96
Ho	0.80	1.433	0.106	2.583	1.150	66.00
Er	0.95	1.438	0.111	2.865	1.427	77.08
Er	0.75	1.438	0.111	2.488	1.051	62.04
Y	0.80	1.340	0.013	2.583	1.150	66.00
Y	0.60	1.340	0.013	2.207	0.867	54.68
Sm	0.85	1.410	0.083	2.677	1.267	70.68

Table 2.4. Some initial data and results of calculation of mixing energies and critical decomposition temperatures for $La_{1-x}Ln_xFeAsO_{1-y}$ solid solutions (Ln = Ce–Er, and Y)

Ln	1–y	$r(Ln^{3+})$, Å	Ln–O, Å	δ	C, kJ	m	Q, J/mol	T_{cr}, K
La	0.65	1.240	2.480		58.92	2.65		
Ce	0.65	1.210	2.450	0.01224	58.08	2.65	1175	70
Pr	0.65	1.198	2.436	0.01806	57.04	2.65	2513	150
Nd	0.65	1.186	2.426	0.02225	56.72	2.65	3794	226
Pm	0.65	1.172	2.412	0.02819	56.36	2.65	6053	361
Sm	0.65	1.160	2.400	0.03333	55.60	2.65	8346	498
Eu	0.65	1.150	2.390	0.03765	54.68	2.65	10474	625
Gd	0.65	1.140	2.380	0.04202	56.56	2.65	13496	806
Tb	0.65	1.120	2.360	0.05084	55.60	2.65	19422	1159
Dy	0.65	1.110	2.350	0.05531	54.96	2.65	22722	1352
Ho	0.80	1.098	2.338	0.06073	66.00	2.80	34759	2075
Y	0.80	1.100	2.340	0.05982	66.00	2.80	33725	2014
Y	0.60	1.100	2.340	0.05982	54.68	2.60	25945	1549
Sm	0.85	1.160	2.400	0.03333	70.68	2.85	11412	681
Er	0.95	1.085	2.325	0.06666	77.08	2.95	51530	3077
Er	0.75	1.085	2.325	0.06666	62.04	2.75	38663	2309

The calculations were carried out for substitutions in the previously oxygen-deficient compounds [2.19, 2.20, 2.22], synthesized by the following procedures:

1. Samples of the $LnFeAsO_{0.8}$ initial composition with Ln = Ho and Y sintered for 1 h at a temperature of 1 273 K and a pressure of 5 GPa. After

turning off the power, the samples were quickly quenched to room temperature by cooling in water for about 1 min and then the pressure was released [2.19].

2. Samples of the $LnFeAsO_{1-y}$ composition ($y = 0{,}60$–$0{,}70$), synthesized at a pressure of 2.0 GPa for Ln = La, Ce, Pr, Nd, at a pressure of 5.0 GPa for Ln = Sm, Gd, Tb and at a pressure of 5.5 GPa for Ln = Dy. The pellets were heated for 2 h at a synthesis temperature of 1 323–1 373 K for Ln = Gd, Tb, Dy and 1 373–1 423 K for Ln = La, Ce, Pr, Nd and Sm [2.22].

3. Samples with the $ErFeAsO_{1-y}$ nominal composition were synthesized by heating pellets, sandwiched between $LaFeAsO_{0.8}H_{0.8}$ granules at 1 373 K under a pressure of 5.0–5.5 GPa [2.20].

As can be seen from the data presented, with an increase in the atomic number of REEs, values of the dimensional parameter δ, mixing energies Q, and critical decomposition temperatures T_{cr} increase in the series of the $La_{1-x}Ln_xFeAsO_{1-y}$ systems, where Ln = Ce–Er. This is so since in such series of systems the difference between the radii of lanthanum and REE ions increases. According to the calculated values of the critical decomposition temperatures (for $x = 0.50$) and decomposition temperatures of limited solid solutions (for $x = 0.01$, $x = 0.03$, $x = 0.05$, $x = 0.09$, see Table 2.5) their dependence on REE numbers for the $La_{1-x}Ln_xFeAsO_{0.65}$ systems with Ln = Ce–Dy (diagram of thermodynamic stability of solid solutions) was plotted in Fig. 2.3.

Table 2.5. Decomposition temperatures (K) of $La_{1-x}Ln_xFeAsO_{0.65}$ solid solutions, where Ln = Ce–Dy, for $x = 0.01$, 0.03, 0.05, 0.09, and 0.50

x	Ce	Pr	Nd	Pm	Sm	Eu	Gd	Tb	Dy
0,01	30	64	97	154	213	267	344	495	579
0,03	38	81	122	196	269	338	436	627	734
0,05	43	92	138	221	305	382	493	709	830
0,09	50	106	161	256	353	443	571	822	962
0,50	70	150	226	361	498	625	806	1159	1352

The thermodynamic stability diagram was calculated only for $La_{1-x}Ln_xFeAsO_{0.65}$ systems, where Ln = Ce–Dy, since the chemical composition of their components in terms of oxygen content is identical and the value $(1-y)$ according to Ref. [2.22] differed only within 0.60–0.70 (for the calculations, an average value of 0.65 was taken).

It follows from the presented diagram that the continuous series of solid solutions for the $La_{1-x}Ln_xFeAsO_{0.65}$ systems (Ln = Ce–Dy) are thermodynami-cally stable in the temperature ranges above the critical ones (above curve e).

At lower temperatures (below curve e), they can decompose, forming two series of limited solid solutions in each system, if the diffusion rate is sufficient for the formation and growth of new phases. Similarly, limited solid solutions of limiting compositions $x = 0.01$, $x = 0.03$, $x = 0.05$, and $x = 0.09$ at temperatures in the region above curves a, b, c, and d are thermodynamically stable while below these curves they can decompose. It should be also noted that a change in the oxygen content significantly affects the mixing energy, the critical decomposition temperatures of solid solutions, and, consequently, the stability and substitution limits. Thus, in the $La_{1-x}Ln_xFeAsO_{1-y}$ systems with Ln = Sm, Er, and Y, with growing $(1-y)$ values from 0.65, 0.75 and 0.60 to 0.85, 0.95 and 0.80, the critical decomposition temperatures increase from 498, 2 309 and 1 549 K to 681, 3 077 and 2 014 K respectively.
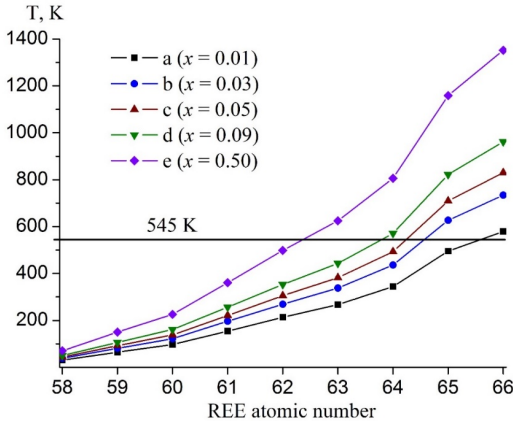

Fig. 2.3 – Diagram of the thermodynamic stability of solid solutions: Dependences of the calculated decomposition temperatures for $La_{1-x}Ln_xFeAsO_{0.65}$ solid solutions (Ln = Ce–Dy) for $x = 0.01$ (a), $x = 0.03$ (b), $x = 0.05$ (c), $x = 0.09$ (d), and $x = 0.50$ (e) of the REE atomic number. Below the horizontal line at 545 K, solid solutions can become metastable

It is known that with decreasing temperature the mobility of the solid-solution structural units reduces due to the diminishing diffusion rate and the solubility regions become narrower [2.49–2.50]. This happens until the diffusion rate becomes so small that the decrease in the solubility regions practically stops, i. e., spontaneous hardening occurs and solid solutions can be metastable. If we assume that the spontaneous hardening temperature is close

to the temperature at which the components begin to interact when their mixture is heated, leading to the formation of a solid solution, we can estimate the spontaneous hardening temperature and the metastability region [2.57]. For example, as was shown in Ref. [2.46], the BiCuSO compound with the ZrCuSiAs structure, similar in composition to LnFeAsO, was synthesized by the low-temperature hydrothermal method at 520 K or using freshly prepared highly reactive precursor compounds at 570 K. Therefore, it can be assumed that spontaneous hardening of solid solutions of the systems under consideration can occur at temperatures of ~545 K and less.

Thus, the $La_{1-x}Ln_xFeAsO_{0.65}$ systems with Ln = Ce–Dy, continuous series of solid solutions, are thermodynamically stable above the critical decomposition temperatures of 70–1 352 K (Table 2.4, Fig. 2.3, curve e). With decreasing temperatures, they become thermodynamically unstable and can split into two regions of limited solid solutions. At temperatures below ~545 K solid solutions should not decompose, that is, spontaneous hardening will take place and they will come to be metastable.

Based on the foregoing, it can be assumed that continuous series of solid solutions in the $La_{1-x}Ln_xFeAsO_{0.65}$ systems, where Ln = Ce–Pm, in the range of temperatures above the critical one (above 70, 150, 226, and 361°K, respectively) will be thermodynamically stable, and below critical temperatures do not decompose, i. e., become metastable.

In the range from melting temperatures to critical ones (625, 806, 1 159, 1 352 K respectively), continuous series of solid solutions in the $La_{1-x}Ln_xFeAsO_{0.65}$ systems with Ln = Eu–Dy will be thermodynamically stable. In the temperature range from critical one to ~ 545 K they will decompose into two solid solutions, which will become metastable at lower temperatures. Since the critical temperature of the $La_{1-x}Sm_xFeAsO_{0.65}$ solid solutions (498 K) differs from the spontaneous hardening temperature (~ 545 K) within the calculational error, it is not possible to conclude unequivocally about their behaviour at temperatures close to the critical one.

According to Fig. 2.3, one can visually estimate the decomposition temperature of limited series of solid solutions by setting the substitution limit or determine the substitution limit of lanthanum for REE by setting the decomposition temperature. To find the substitution limit for a given temperature, it

is necessary to draw an isotherm until it intersects with a vertical line drawn from the REE number. This will determine the range of compositions in which there is a substitution limit, and the interpolation of the vertical segment between the two nearest curves gives this substitution limit. The slatter can be determined more precisely by constructing for a specific system the dependence of the decomposition temperatures calculated from the Becker equation on the composition (the dome of decomposition), which, in the approximation of regular solid solutions, will be symmetrical.
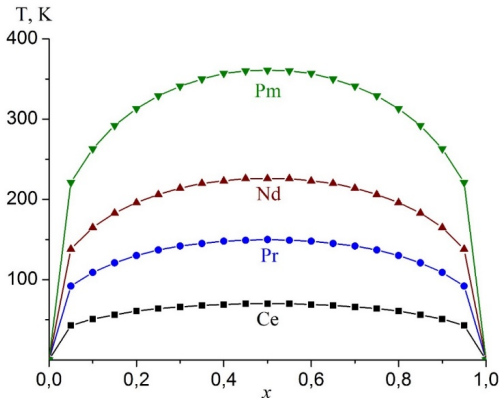

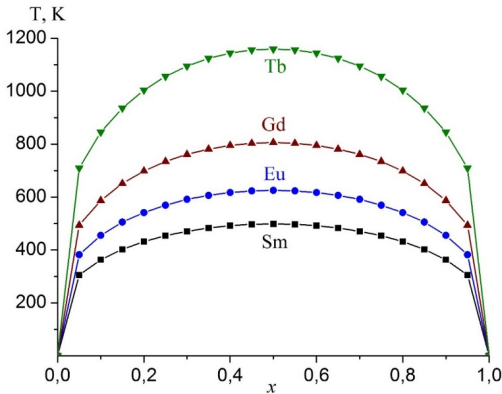Fig. 2.4 – Calculated domes of the solid solutions decomposition
for $La_{1-x}Ln_xFeAsO_{0.65}$ systems

Fig. 2.5 – Calculated domes of the solid solutions decomposition
for the $La_{1-x}Ln_xFeAsO_{0.65}$ systems

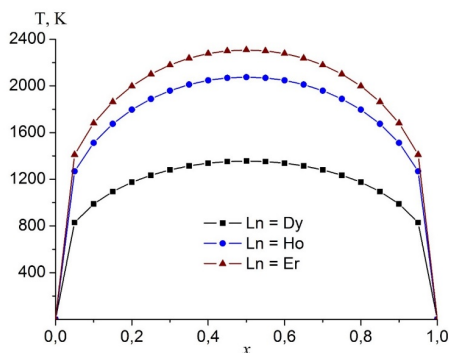Fig. 2.6 – Calculated domes of the solid solutions decomposition
for $La_{1-x}Ln_xFeAsO_{1-y}$ systems with Ln = Dy $(1-y = 0.65)$ (■); Ln = Ho $(1-y = 0.80)$ (●);
Ln = Er $(1-y = 0.75)$ (▲)

To do this, using the Becker equation, the decomposition temperatures for the $La_{1-x}Ln_xFeAsO_{1-y}$ systems, where Ln = Ce–Er, and Y, were calculated in the composition range $1,0 > x > 0$ with the step $x = 0.05$ and the dependences of the decomposition temperatures on the composition (domes of decomposition, Fig. 2.4–2.8) were plotted. Using them, with greater accuracy, one can graphically determine the equilibrium composition at a given temperature, or the decomposition temperature at a given composition, as well as the stability regions of solid solutions.

2.5 Comparison of calculation results with literature data

To the best of our knowledge, there are no literature data concerning mixing energies and critical decomposition temperatures in the $La_{1-x}Ln_xFeAsO_{1-y}$ systems. This, of course, makes it difficult to assess the reliability of the calculations performed. At the same time, there is information about experimental studies of isomorphous substitutions of lanthanum for yttrium in the $La_{1-x}Y_xFeAsO_{0.6}$ system [2.34] and lanthanum for samarium in the $La_{1-x}Sm_xFeAsO_{0.85}$ system [2.36]. In the $La_{1-x}Y_xFeAsO_{0.6}$ system, the substitution limit of lanthanum for yttrium at 1 423 K was not determined in Ref. [2.34]. Using the XRD method it was shown that the single-phase region extends up to $x = 0.1$ inclusive, the non-single-phase region is located at $x \geq 0.2$, and the cell parameters decrease in the region up to $x = 0.4$. It follows

from this that the substitution limit is in the interval between 0.1 and 0.4, which does not contradict the limit $x = 0.27$ calculated by us (Fig. 2.7) that is in the middle of this interval.

In the $La_{1-x}Sm_xFeAsO_{0.85}$ system, compositions with $x = 0$, 0.1, 0.2, 0.3, 0.4, 0.6, 0.8, 0.9, 0.95, and 1.0 were previously studied [2.36]. According to the phase composition and the change in cell parameters, unlimited substitution of lanthanum for samarium in the x range from 0 to 1 was established. This does not oppose the calculation results, since the established unlimited miscibility of the components [2.36] is in the temperature range above 681 K which is predicted by us for the thermodynamic stability of continuous series of solid solutions, see Table 2.4 and Fig. 2.8.
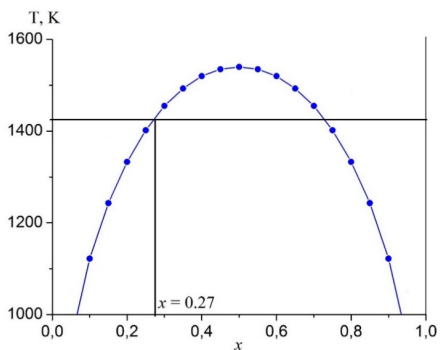

Fig. 2.7 – Calculated dome of the solid solutions decomposition
for the $La_{1-x}Y_xFeAsO_{0.6}$ system. The straight line at 1 423 K is the temperature
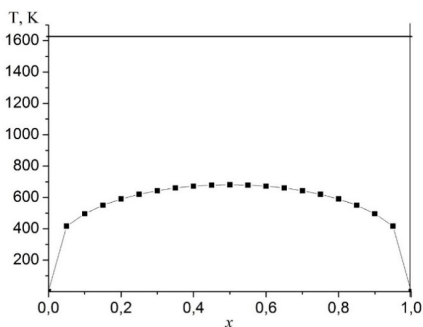of the solid solution synthesis [2.34]

Fig. 2.8 – Calculated dome of the solid solutions decomposition
for the La1–xSmxFeAsO0.85 system. The straight line at 1 623 K is the temperature
of the solid solution synthesis [2.36]

2.6 Conclusions

1. Within the approximation of regular solid solutions and using the crystal-chemical approach by V. S. Urusov, the mixing energies (interaction parameters) and critical decomposition (stability) temperatures of solid solutions of the $La_{1-x}Ln_xFeAsO_{1-y}$ systems (Ln = Ce–Er, and Y) with the ZrCuSiAs structure have been calculated.

2. With an increase in the REE number, the calculated mixing energies and critical decomposition temperatures for the $La_{1-x}Ln_xFeAsO_{1-y}$ solid solutions grow in the Ce–Er series of the rare earth elements.

3. It is shown that the magnitude of the mixing energy is determined mainly by the difference in sizes of the substituting structural units of the system components.

4. The presented thermodynamic stability diagram for the $La_{1-x}Ln_xFeAsO_{0.65}$ systems with Ln = Ce–Dy makes it possible to visually evaluate not only the thermodynamic stability, instability, and supposed metastability of solid solutions in a wide range of compositions and temperatures, but also the substitution limits for limited series of solid solutions according to a given decomposition temperature, or their decomposition temperature according to a given substitution limit.

5. Continuous series of solid solutions in the $La_{1-x}Ln_xFeAsO_{0.65}$ systems (Ln = Ce–Pm) in the range of temperatures above the critical ones (above 70, 150, 226, 361 K, respectively) will be thermodynamically stable, and below the critical ones they cannot decompose, i. e., become metastable. In the range of temperatures above the critical ones (625, 806, 1 159, 1 352 K, respectively), continuous series of solid solutions in the $La_{1-x}Ln_xFeAsO_{0.65}$ systems with Ln = Eu–Dy will be thermodynamically stable. In the temperature range from critical values to ~ 545 K, they will decompose into two solid solutions, which will become metastable at lower temperatures.

6. The decomposition temperatures of solid solutions in the $La_{1-x}Ln_xFeAsO_{1-y}$ systems, where Ln = Ce–Er and Y, have been calculated in the composition range $1.0 > x > 0$ with the step $x = 0.05$ and the dependences of their decomposition temperatures on the composition (domes of decomposition) were plotted.

7. The calculation results do not contradict experimental data for $La_{1-x}Y_xFeAsO_{0.6}$ and $La_{1-x}Sm_xFeAsO_{0.85}$ systems obtained by other research groups [2.34, 2.36].

2.7 References to chapter 2

2.1 Kamihara Y., Hiramatsu H., Hirano M., Kawamura R., Yanagi H., Kamiya T., Hosono H. Iron-based layered superconductor: LaOFeP. *J. Am. Chem. Soc.* 2006. V. 128. P. 10012–10013.

2.2 Kamihara Y., Watanabe T., Hirano M., Hosono H. Iron-based layered superconductor $La[O_{1-x}F_x]FeAs$ (x = 0.05–0.12) with $T_c = 26$ K. *J. Am. Chem. Soc.* 2008. V. 130. P. 3296–3297.

2.3 Boeri L., Dolgov O. V., Golubov A. A. Is $LaFeAsO_{1-x}F_x$ an electron-phonon superconductor? *Phys. Rev. Lett.* 2008. V. 101. P. 026403.

2.4 Takahashi H., Igawa K., Arii K., Kamihara Y., Hirano M., Hosono H. Superconductivity at 43 K in an iron-based layered compound $LaO_{1-x}F_xFeAs$. *Nature*. 2008. V. 453. P. 376–378.

2.5 Shekhar Ch., Singh S., Siwach P. K., Singh H. K., Srivastava O. N. Synthesis and microstructural studies of iron oxypnictide $LaO_{1-x}F_xFeAs$ superconductors. *Supercond. Sci. Technol.* 2009. V. 22. P. 015005.

2.6 Ren Zh.-A., Che G.-C., Dong X.-L., Yang J., Lu W., Yi W., Shen X.-L., Li Zh.-C., Sun L.-L., Zhou F., Zhao Zh.-X. Superconductivity and phase diagram in iron-based arsenic-oxides $ReFeAsO_{1-\delta}$ (Re = rare-earth metal) without fluorine doping. *Europhys. Lett.* 2008. V. 83. P. 17002.

2.7 Chen G. F., Li Z., Wu D., Li G., Hu W. Z., Dong J., Zheng P., Luo J. L., Wang N. L. Superconductivity at 41 K and its competition with spin-density-wave instability in layered $CeO_{1-x}F_xFeAs$. *Phys. Rev. Lett.* 2008. V. 100. P. 247002.

2.8 Zocco D. A., Hamlin J. J., Baumbach R. E., Maple M. B., McGuire M. A., Sefat A. S., Sales B. C., Jin R., Mandrus D., Jeffries J. R., Weir S. T., Vohra Y. K. Effect of pressure on the superconducting critical temperature of $La[O_{0.89}F_{0.11}]FeAs$ and $Ce[O_{0.88}F_{0.12}]FeAs$. *Phys. C: Supercond.* 2008. V. 468. P. 2229–2232.

2.9 Ren Z. A., Yang J., Lu W., Yi W., Che G. C., Dong X. L., Sun L. L., Zhao Z. X. Superconductivity at 52 K in iron based F doped layered

quaternary compound $Pr[O_{1-x}F_x]FeAs$. *Mater. Res. Innov.* 2008. V. 12. P. 105–106.

2.10 Ren Z.-A., Yang J., Lu W., Yi W., Shen X.-L., Li Z.-C., Che G.-C., Dong X.-L., Sun L.-L., Zhou F., Zhao Z.-X. Superconductivity in the iron-based F-doped layered quaternary compound $Nd[O_{1-x}F_x]FeAs$. *Europhys. Lett.* 2008. V. 82. P. 57002.

2.11 Cheng P., Yang H., Jia Y., Fang L., Zhu X., Mu G., Wen H.-H. Hall effect and magnetoresistance in single crystals of $NdFeAsO_{1-x}F_x$ (x = 0 and 0.18). *Phys. Rev. B*. 2008. V. 78. P. 134508.

2.12 Jaroszynski J., Hunte F., Balicas L., Jo Y.-J., Raičević I., Gurevich A., Larbalestier D. C., Balakirev F. F., Fang L., Cheng P., Jia Y., Wen H. H. Upper critical fields and thermally-activated transport of $NdFeAsO_{0.7}F_{0.3}$ single crystal. *Phys. Rev. B*. 2008. V. 78. No. 174523.

2.13 Ren Zh.-A., Lu W., Yang J., Yi W., Shen X.-L., Li Zh.-C., Che G.-C., Dong X.-L., Sun L.-L., Zhou F., Zhao Zh.-X. Superconductivity at 55 K in iron-based F-doped layered quaternary compound $Sm[O_{1-x}F_x]FeAs$. *Chin. Phys. Lett*. 2008. V. 25. P. 2215–2216.

2.14 Chen X. H., Wu T., Wu G., Liu R. H., Chen H., Fang D. F. Superconductivity at 43 K in $SmFeAsO_{1-x}F_x$. *Nature*. 2008. V. 453. P. 761–762.

2.15 Yang J., Li Zh.-C., Lu W., Yi W., Shen X.-L., Ren Zh.-A., Che G.-C., Dong X.-L., Sun L.-L., Zhou F., Zhao Zh.-X. Superconductivity at 53.5 K in $GdFeAsO_{1-\delta}$. *Supercond. Sci. Technol.* 2008. V. 21. P. 082001.

2.16 Cheng P., Fang L., Yang H., Zhu X., Mu G., Luo H.-Q., Wang Zh.-Sh., Wen H.-H. Superconductivity at 36 K in gadolinium-arsenide oxides $GdO_{1-x}F_xFeAs$. *Sci. China: Phys. Mech. Astron.* 2008. V. 51. P. 719–722.

2.17 Shi Y. G., Yu S., Belik A. A., Matsushita Y., Tanaka M., Katsuya Y., Kobayashi K., Yamaura K., Takayama-Muromachi E. Synthesis and superconducting properties of the iron oxyarsenide $TbFeAsO_{0.85}$. *J. Phys. Soc. Jpn.* 2008. V. 77. P. 155–157.

2.18 Bos J.-W. G., Penny G. B. S., Rodgers J. A., Sokolov D. A., Huxley A. D., Attfield J. P. High pressure synthesis of late rare earth RFeAs(O,F) superconductors; R = Tb and Dy. *Chem. Commun*. 2008. V. 31. P. 3634–3635.

2.19 Yang J., Shen X.-L., Lu W., Yi W., Li Z.-C., Ren Z.-A., Che G.-C., Dong X.-L., Sun L.-L., Zhou F. Zhao Z.-X. Superconductivity in some

heavy rare-earth iron arsenide $REFeAsO_{1-\delta}$ (RE = Ho, Y, Dy and Tb) compounds. *New J. Phys*. 2009. V. 11. P. 025005.

2.20 Shirage P. M., Miyazawa K., Kihou K., Lee Ch.-H., Kito H., Tokiwa K., Tanaka Y., Eisaki H., Iyo A. Synthesis of ErFeAsO-based superconductors by the hydrogen doping method. *Europhys. Lett.* 2010. V. 92. P. 57011.

2.21 Rodgers J. A., Penny G. B. S., Marcinkova A., Bos J.-W. G., Sokolov D. A., Kusmartseva A., Huxley A. D., Attfield J. P. Suppression of the superconducting transition of $RFeAsO_{1-x}F_x$ (R = Tb, Dy, and Ho). *Phys. Rev. B*. 2009. V. 80. P. 052508.

2.22 Miyazawa K., Kihou K., Shirage P. M., Lee Ch.-H., Kito H., Eisaki H., Iyo A. Superconductivity above 50 K in $LnFeAsO_{1-y}$ (Ln = Nd, Sm, Gd, Tb, and Dy) synthesized by high-pressure technique. *J. Phys. Soc. Jpn.* 2009. V. 78. P. 034712.

2.23 Sadovskii M. V. High-temperature superconductivity in iron-based layered iron compounds. *Phys.-Usp.* 2008. V. 51, P. 1201–1227.

2.24 Ishida K., Nakai Y., Hosono H. To what extent iron-pnictide new superconductors have been clarified: a progress report. *J. Phys. Soc. Jpn*. 2009. V. 78. P. 062001.

2.25 Oh H., Moon J., Shin D., Moon Ch.-Y., Choi H. J. Brief review on iron-based superconductors: are there clues for unconventional superconductivity? *Prog. Supercond. Cryog.* 2011. V. 13. P. 65–84.

2.26 Si Q., Yu R., Abrahams E. High-temperature superconductivity in iron pnictides and chalcogenides. *Nat. Rev. Mater.* 2016. V. 1. P. 16017.

2.27 Hosono H., Yamamoto A., Hiramatsu H., Ma Y. Recent advances in iron-based superconductors toward applications. *Mater. Today*. 2018. V. 21. P. 278–302.

2.28 Rasaki S. A., Thomas T., Yang M. Iron based chalcogenide and pnictide superconductors: From discovery to chemical ways forward. *Prog. Solid. State Ch.* 2020. V. 59. P. 100282.

2.29 Song C., Ma X., Xue Q. Emergent high-temperature superconductivity at interfaces. *MRS Bulletin*. 2020. V. 45. P. 366–372.

2.30 Fernandes R. M., Coldea A. I., Ding H., Fisher I. R., Hirschfeld P. J., Kotliar G. Iron pnictides and chalcogenides: a new paradigm for superconductivity. *Nature*. 2022. V. 601. P. 35–44.

2.31 Izyumov Yu., Kurmaev E. High-T$_c$ superconductors based on FeAs compounds. Springer Series in Materials Science. Vol. 143. Springer Heidelberg Dordrecht London New York. 2010.

2.32 Iron-Based Superconductors. Edited by N.-L. Wang, H. Hosono, P. Dai. Pan Stanford Publishing: Taylor & Francis Group. 2013.

2.33 Mancini F., Citro R. The Iron Pnictide Superconductors: An Introduction and Overview. Springer Series in Solid-State Sciences. Vol. 186. Springer International Publishing AG. 2017.

2.34 Shirage P. M., Miyazawa K., Kito H., Eisaki H., Iyo A. Superconductivity at 43 K at ambient pressure in the iron-based layered compound La$_{1-x}$Y$_x$FeAsO$_y$. *Phys. Rev. B.* 2008. V. 78. P. 172503.

2.35 Tropeano M., Fanciulli C., Canepa F., Cimberle M. R., Ferdeghini C., Lamura G., Martinelli A., Putti M., Vignolo M., Palenzona A. Effect of chemical pressure on spin density wave and superconductivity in undoped and 15 % F-doped La$_{1-y}$Y$_y$FeAsO compounds. *Phys. Rev. B.* 2009. V. 79. P. 174523.

2.36 Yi W., Yang J., Shen X.-L., Lu W., Li Zh.-C., Ren Zh.-A., Che G.-C., Dong X.-L., Zhou F., Sun L.-L., Zhao Zh.-X. Superconductivity in the mixed rare earth iron oxyarsenide La$_{1-x}$Sm$_x$FeAsO$_{0.85}$. *Supercond. Sci. Technol.* 2008. V. 21. P. 125022.

2.37 Arumugam S., Kanagaraj M., Tamil Selvan N. R., Esakki Muthu S., Prakash J., Thakur G. S., Ganguli A. K., Yoshino H., Murata K., Matsubayashi K., Uwatoko Y. Pressure effects on the superconducting transition of ytterbium doped Ce$_{0.6}$Yb$_{0.4}$FeAsO$_{0.9}$F$_{0.1}$. *Phys. Status Solidi RRL.* 2012. V. 6. P. 220–222.

2.38 Li L.-J., Li Y.-K., Ren Z., Luo Y.-K., Lin X., He M., Tao Q., Zhu Zh.-W., Cao G.-H., Xu Zh.-A. Superconductivity above 50 K in Tb$_{1-x}$Th$_x$FeAsO. *Phys. Rev. B.* 2008. V. 78. P. 132506.

2.39 Wang C., Li L., Chi S., Zhu Z., Ren Z., Li Y., Wang Y., Lin X., Luo Y., Jiang S., Xu X., Cao G., Xu Z. Thorium-doping–induced superconductivity up to 56 K in Gd$_{1-x}$Th$_x$FeAsO. *Europhys. Lett.* 2008. V. 83. P. 67006.

2.40 Zhigadlo N. D., Katrych S., Weyeneth S., Puzniak R., Moll P. J. W., Bukowski Z., Karpinski J., Keller H., Batlogg B. Th-substituted

SmFeAsO: Structural details and superconductivity with T_C above 50 K. *Phys. Rev. B*. 2010. V. 82. P. 064517.

2.41 Ohmukai M., Fujita T., Ohn T. The Temperature dependence of critical current in $YBa_2Cu_3O_{7-d}$ thin films deposited on MgO by an eclipse PLD. *Braz. J. Phys*. 2001. V. 31. P. 511–513.

2.42 Conradson S. D., Raistrick I. D. The Axial Oxygen Atom and Superconductivity in $YBa_2Cu_3O_7$. *Science*. 1989. V. 243. P. 1340–1343.

2.43 Moriya K., Igarashi K., Watanabe H., Hasegawa H., Sasaki T., Yasuda A. Growth of $YBa_2Cu_3O_7$ superconductor thin films using ethanolamine-based solutions via simple spin coating. *Results. Phys.* 2018. V. 11. P. 364–367.

2.44 Dhami A. K., Basak S., Ghatak S. K., Dey T. K. Thermoelectric power of samarium substituted $Y_{1-x}Sm_xBa_2Cu_3O_{7-\delta}$ superconducting pellets. *Mater. Res. Bull.* 2001. V. 36. P. 971–980.

2.45 Haugan T. J., Campbell T. A., Pierce N. A., Locke M. F., Maartense I., Barnes P. N. Microstructural and superconducting properties of $(Y_{1-x}Eu_x)Ba_2Cu_3O_{7-\delta}$ thin films: x = 0–1. *Supercond. Sci. Technol.* 2008. V. 21. P. 025014.

2.46 Pöttgen R., Johrendt D. Materials with ZrCuSiAs-type structure. *Z. Naturforsch. B*. 2008. V. 63b. P. 1135–1148.

2.47 Iadecola A., Joseph B., Paris E., Provino A., Martinelli A., Manfrinetti P., Putti M., Saini N. L. Effect of chemical pressure on the local structure of $La_{1-x}Sm_xFeAsO$ system. *Supercond. Sci. Technol*. 2015. V. 28. P. 025007.

2.48 Chen H., Zheng M., Fang A., Yang J., Huang F., Xie X., Jiang M. Enhanced superconductivity of SmFeAsO Co-doped by scandium and fluorine to increase chemical inner pressure. *J. Solid State Chem.* 2012. V. 194. P. 59–64.

2.49 Urusov V. S. Teoriia izomorfnoi smesimosti [The Theory of Isomorphous Miscibility]. Moscow: Nauka. 1977. (in Russian).

2.50 Urusov V. S., Tauson B. L., Akimov V. V. Geokhimiya tverdogo tela [Solid state geochemistry]. Moscow: GEOS. 1997. (in Russian).

2.51 Hunte F., Jaroszynski J., Gurevich A., Larbalestier D. C., Jin R., Sefat A. S., McGuire M. A., Sales B. C., Christen D. K., Mandrus D. Two-

band superconductivity in $LaFeAsO_{0.89}F_{0.11}$ at very high magnetic fields. *Nature*. 2008. V. 453. P. 903–905.

2.52 Li K., Xue D. Estimation of electronegativity values of elements in different valence states. *J. Phys. Chem. A.* 2006. V. 110. P. 11332–11337.

2.53 Batsanov S. S. Ob effektivnom koordinatsionnom chisle atomov v kristallakh [On the effective coordination number of atoms in crystals]. *Zh. Neorg. Khim.* 1977. V. 22. P. 1155–1159. (in Russian).

2.54 Zhigadlo N. D., Weyeneth S., Katrych S., Moll P. J. W., Rogacki K., Bosma S., Puzniak R., Karpinski J., Batlogg B. High-pressure flux growth, structural, and superconducting properties of LnFeAsO (Ln = Pr, Nd, Sm) single crystals. *Phys. Rev. B.* 2012. V. 86. P. 214509.

2.55 Shannon R. D. Revised effective ionic radii and systematic studies of interatomic distances in halides and chalcogenides. *Acta Cryst. Sect. A.* 1976. V. A32. P. 751–767.

2.56 Becker R. Über den aufbau binarer legierungen (On the constitution of binary alloys). *Zeit. Metal.* 1937. V. 29. P. 245–249. (in German).

2.57 Get'man E. I., Radio S. V., Ignatova L. B., Ardanova L. I. Energies of mixing (interaction parameters), substitution limits, and phase stability of solid solutions $Lu_{1-x}Ln_xVO_4$ (Ln = Ce–Yb, Sc, Y). *Russ. J. Inorg. Chem.* 2019. V. 64. P. 118–124.

3. SPIN-POLARIZED SUPERCURRENT IN PROXIMITIZED SINGLET SUPERCONDUCTOR – HALF-METALLIC MANGANITE NANOSTRUCTURES

V. Krivoruchko[1], V. Tarenkov[1]

Abstract

A common path to superconducting spintronics, superconducting magnonics, and topologically protected quantum computing relies on spin-triplet superconductivity. However, superconductors realizing spin-triplet *p*-wave pairing are not common in nature. While naturally occurring spin-triplet superconducting pairing is very exclusive, proximity effects in ferromagnet / superconductor heterostructures can overcome this limitation. That is why artificial nanostructures demonstrating equal-spin triplet superconductivity have attracted special interest as new functional materials. In this chapter, we present the results of experimental and theoretical investigations of proximitized nanocomposites based on half-metallic manganites – singlet *s*-wave or *d*-wave superconductors. The experimental data obtained, and theoretical reasoning give conclusive evidence that proximity induced long-range superconducting state in such hybrid structures can be qualitatively and quantitatively understood within the scenario of proximity induced *p*-wave spin-triplet superconductivity. It means that the superconductor–half-metallic manganites nanostructures are promising functional materials for superconducting spintronics, superconducting magnonics, and topologically protected quantum computing.

✉ Vladimir Krivoruchko
krivoruc@gmail.com

[1] O. O. Galkin Donetsk Institute for Physics and Engineering, National Academy of Sciences of Ukraine, Nauki Ave. 46, 03028 Kyiv, Ukraine

3.1 Introduction

Over past decades, one of the basic directions in the condensed matter physics has been search of materials for *superconducting spintronics*, *superconducting magnonics*, as well as materials with topologically protected quasiparticle excitations for a *quantum computer*.

Digital superconductive electronics is inherently faster at much less power dissipation than semiconductor analogue. That is why a superconducting version of the conventional spintronics – superconducting spintronics – has become the most attractive subject of spintronics in past decades [3.1–3.6]. The idea of combining superconductivity with spintronics and magnonics has focused on the net spin polarization of quasiparticles in superconductors – triplet Cooper pairs. Condensed materials with the spin-triplet superconducting pairing state will have great potential applications in the field of superconducting spintronics and magnonics and recent experimental demonstration of spin-polarized supercurrents in proximitized structures provides a guiding principle of the functional materials establishment. The field of superconducting spintronics and magnonics offers new concepts for spin transmission by combining superconducting phase coherence and magnetism [3.4, 3.7]. Spin-polarized supercurrent offers new ideas to carry information by spin instead of charge, leads to massive reductions in ohmic losses and support the development of novel spin-based devices. The exploration of superconducting spin currents opens fascinating potential for novel spintronic device concepts.

At the present time in the condensed matter physics a 'second quantum revolution' is carried out through the introduction of topology-originated concepts used to characterize physical states and properties of solids (see, e. g., reviews [3.8–3.11] and references therein). With the introduction of topology, the description of phase transitions and phases of the system expands and includes not only differentiating in terms of a local (Landau) order parameter, but also those characterized in terms of global quantities that are measured nonlocally and which endow the system with a global stability to perturbations. Topological state is a state of a matter characterized by nonzero topological number of the wave functions and nontrivial topological states of their quasiparticles. One of the promising motivations of topology-originated views in the condensed matter physics is searching for materials to create a quantum

computer. The most significant obstacles for successful realization of a quantum computer are the quantum decoherence, i. e., a loss of information from a system. In this regard, quantum computing, based on topologically protected excitations has been considered as an attractive solution for overcoming the related problems [3.12–3.16]. It processes quantum information in a nonlocal fashion, and in addition exploits the peculiarities of non-Abelian braiding statistics, allowing the performance of decoherence-free and fault-tolerant quantum logical operations [3.15]. In this standpoint, so-called Majorana fermions have been proposed as elementary building blocks of a topological quantum computing hardware [3.16].

Majorana fermions are fundamental particles originally proposed in 1937 by E. Majorana as a real solution to the Dirac equation. The Majorana fermion is a fermion that is its own antiparticle has no charge but can carry spin or heat. Among promising grounds for topologically protected non-Abelian excitations like Majorana fermion is a superconducting state. Topological superconducting states support topologically protected gapless Andreev bound states that are their own antiparticles, and which partially mimic the so-called zero mode Majorana fermions. Recently, a great effort has been put towards an unambiguous experimental detection of Majorana fermions in systems which, as expected, can be in the topological superconducting state (see, e. g., reviews [3.8–3.10] and references therein).

Though topological materials and their unusual properties are in a focus of modern experimental and theoretical research in condensed matter physics, beyond doubt, experimental identification / observation of Majorana quasiparticles is still absent. Materials having good prospects for the topological superconducting phase realization are those with the spin-triplet superconducting pairing state [3.10]. Indeed, in a p-wave superconductor (SC) Bogoliubov quasiparticles, $b_{\mathbf{k}\sigma} = uc_{\mathbf{k}\sigma} + vc_{\mathbf{-k}\sigma}^+ = (u - v^*)c_{\mathbf{k}\sigma} + (v^*c_{\mathbf{k}\sigma} + vc_{\mathbf{-k}\sigma}^+)$, have both electron and hole components of equal spin projection, σ, and thus can possess the Majorana fermions properties. The task is to create necessary conditions when p-wave Bogoliubov quasiparticles are 'forced' to demonstrate their Majorana fermions characteristics, i. e., when $b_{\mathbf{k}\sigma} \rightarrow (v^*c_{\mathbf{k}\sigma} + vc_{\mathbf{-k}\sigma}^+)$. Yet, SC realizing a spin-triplet p-wave pairing is not common in nature; Sr_2RuO_4 with the critical temperature $T_C \approx 1.5$ K being the only realistic candidate so far.

A way that overcomes this difficulty settles in artificially engineered topological materials. Artificially engineered topological superconductivity in SC-magnet hybrid structures are currently attracting attention, because, as expected, they represent one of the most promising platforms for realizing topological superconducting phases [3.10, 3.17–3.21]. Particularly, Choy *et al*. has proposed to create Majorana fermions by depositing a chain of magnetic nanoparticles on an *s*-wave superconducting substrate [3.17]. Chung *et al.* [3.18] consider the creation of spin-triplet superconductivity and topological phase in SC / half-metal heterostructures (a half-metal is a spin-polarized metal at the Fermi surface, *i. e.*, a metal for the majority spin and an insulator for the minority spin).

Superconducting phase needs cooling to quite low temperatures. For practical applications cooling with liquid helium is not adequate because the handling is too error prone. In this chapter, we discuss a promising way for creating artificial materials with a high-temperature triplet superconductivity. These are hybrid spin-singlet superconductors–half-metallic manganites nanostructures; in particular, nanocomposites of half-metallic manganites nanoparticles and *s*-wave or *d*-wave SCs. A key factor of these hybrid structures is *local high-temperature triplet superconductivity* of half-metallic manganites. The experimental evidence for the existence of latent (noncoherent) spin-triplet pairing in half-metal manganites is presented and conditions favoring their topological superconductivity are discussed. Our findings presented here are substantially based on the experimental results, especially obtained in Refs. [3.22–3.36], evidencing unconventional superconducting proximity effect in SC / half-metallic manganites hybrid structures.

Summing the above, a common path to superconducting spintronics, superconducting magnonics, and topologically protected quantum computing relies on spin-triplet superconductivity. While naturally occurring spin-triplet superconducting pairing is very exclusive, proximity effects in ferromagnet / superconductor heterostructures can overcome this limitation.

3.2 Coexistence of superconductivity and ferromagnetism, proximity effect

Ferromagnetic order and singlet superconductivity are incompatible, since in a ferromagnet (F) the exchange field H_{exc} splits conduction bands. In a typical metal ferromagnets the exchange energy is larger than the pairing energy of electrons in singlet Cooper pairs by orders of magnitude, so that only triplet amplitudes of the form $f^{tr}(r) = g_1(r)|\uparrow\uparrow>$ or $f^{tr}(r) = g_2(r)|\downarrow\downarrow>$ can be supported. That is why, when a metallic F is in contact with s-wave SC, s-wave Cooper pairs can penetrate into F layer by diffusing only over the small distance given by the superconducting penetration depth $\zeta_F = (4\hbar D_F/H_{exc})^{1/2}$, here D_F is the diffusion coefficient of the conduction electrons in the F layer).

The incompatible nature of superconductivity and ferromagnetic order was confirmed in various materials and geometries. Yet, number of experimental facts point also that a physical interpretation of the proximity effect when Cooper pairs are broken by a strong exchange field H_{exc} in the F layer can be too simplified. Long-ranged proximity effects have been observed in a variety of ferromagnetic materials, including wires [3.37, 3.38], bi- and multi-layers [3.39], half-metallic $La_{0.7}Ca_{0.3}Mn_3O$ [3.40] and CrO_2 [3.41], rare-earth metals with helical magnetic structure [3.42] *etc*. Coexistence of superconductivity and ferromagnetism close to the interfaces in hybrid SC/F systems leads to unusual and interesting phenomena. If a ferromagnet with a uniform exchange field is in a metallic contact with a SC, from a theoretical viewpoint, the base physics is well understood, and the proximity effect is described by considering the splitting of electronic bands of opposite spins [3.43]. The situation becomes more complicated when the magnetic structure is inhomogeneous. Theories [3.26, 3.44, 3.45] predict the appearance of a long-range proximity effect if there is a spatial variation of the magnetization in the F layer. In this case, the triplet component of anomalous correlations needs to be taken into consideration with a characteristic coherence length of $\zeta_F = (\hbar D_F/2\pi T)^{1/2}$ that can be as large as ~ 100 nm at low temperatures (here T is the temperature; we choose $k_B = 1$). See, *e. g.*, the discussion in Ref. [3.5, 3.26, 3.45] and references therein.

Magnetic inhomogeneities may, in principle, be artificially generated in ferromagnets. Yet, existing technology cannot create them in a controlled way

at the SC/F interface with a nanoscale precision so that the most realistic scenario is to use a ferromagnet with given magnetic inhomogeneity. An interesting limit of systems with tunable inhomogeneity of the magnetic partner is SC/F nanocomposites. Being an experimentally accessible electronic system with controllable parameters, such heterostructures offer a unique testing ground for studying superconducting proximity effect in systems with an arbitrary length of magnetic disorder. Superconductivity in a granular mixture of superconductor-insulator films has been extensively studied, both experimentally and theoretically, in the framework of the percolation theory (see, e. g., Ref. [3.46]). The proximity effects in granular superconductor–normal-metal structures are also explored [3.47, 3.48]. Proximity effects in composites of a (nano)granular half-metal ferromagnet (hmF) and conventional s-wave or d-wave superconductors will be discussed in Sec. 3.4.2.

Equal-spin p-wave triplet Cooper pairs are immune to the exchange field and can propagate into ferromagnetic metals over the same long distance as singlet pairs into normal metals. However, superconductors realizing a spin-triplet p-wave pairing are not common in nature; Sr_2RuO_4 with $T_C = 1.5$ K being the only real candidate, so far. That is why artificial materials demonstrating p-wave superconductivity have attracted notable interest. A microscopic quantum mechanism on which the long-range triplet condensate induced in artificial materials is based on the Andreev reflection [3.49].

As is known, at energies below the superconducting gap, the charge transport through a normal nonmagnetic (N) metal been in contact with a SC is possible only due to the specific two-particle process, called Andreev reflection [3.49]. In the N metal, an incident electron above the Fermi energy E_F and an electron below E_F with the opposite spin are coupled together and transferred across the interface into the SC side, forming a singlet Cooper pair in the condensate. Simultaneously, an evanescent hole with opposite momentum and spin appears in the N metal. This implies the doubling of the normal-state conductance since two electrons are transferred across the interface into the SC region where they form a spin-singlet Cooper pair. Unlike this conventional Andreev reflection, a spin-active interface with interfacial spin-flip scattering also yields Andreev reflection with an equal spin of electrons and holes [3.5, 3.50], responsible for spin-triplet pair correlations, see Fig. 3.1. As

the Cooper pair's size is determined by the superconducting coherence length s-wave Cooper pairs extend on a coherence length from the interface SC/F into the F bulk and near the SC/F interface a singlet-triplet mixed Cooper pairs state is formed. (For more details the reader is referred, *e. g.*, to articles [3.5, 3.43, 3.45, 3.51]). The two phenomena, proximity effect and Andreev reflection are intertwined and cannot be discussed separately from each other. The superconducting proximity effect is evidence of the macroscopic quantum coherence and prove the macroscopic character of the Cooper pair wave function.
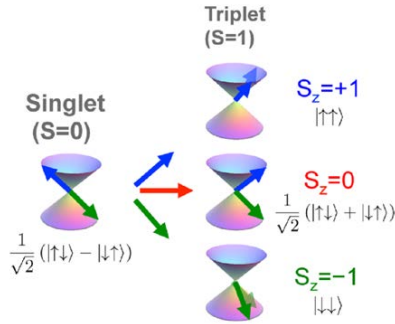

Fig. 3.1 – Andreev reflection at the SC/F interface. Adapted from Ref. [3.5]

Symmetry classification of Cooper pairs in superconductors. Note to avoid confusion, here and below we mean the *ordinary* triplet pairing. That is the Cooper pair wave function is even-spin, even-frequency, odd-momentum. An unconventional new type of superconducting pairing function (even-spin, even-momentum, odd-frequency) the so-called odd triplet pairing, was predicted theoretically [3.45], too. To date, it remains under question direct experimental verification of the odd-frequency symmetry Cooper pair wave function, and we will not consider this superconducting state below.

3.3 Ferromagnetic manganites, spin-polarization, and half-metallicity

Magnetic and transport properties of manganites $R_{1-x}A_xMnO_3$, where trivalent cations R^{3+} are substituted by divalent ones A^{2+}, are discussed in detail in reviews [3.52–3.54] Here we summarized the main physics and statements.

Bulk samples. The initial compound $RMnO_3$ has a perovskite structure. It is electrically homogeneous due to the single valence of the Mn^{3+} ion and below the Neel temperature $T_N \approx 130$ K exhibits an antiferromagnetic order. Compounds of the type $R_{1-x}A_xMnO_3$, where a divalent ion A^{2+} (= Ca, Sr, Ba, Pb, …) replaces the trivalent ion R^{3+}, are electrically inhomogeneous with a competition between different types of magnetic interactions among the Mn ions due to random positions of ions Mn^{3+} and Mn^{4+} having different ionic radii, charges, and spins. When the concentration of the A^{2+} ions exceed ~1/8, the material undergoes a transition to a ferromagnetic state with a metallic type of conductivity. The Curie temperature of the ferromagnetic state depends significantly on the extent of substitution and the difference in the ionic radii of the A^{2+} and La^{3+} ions. The highest value of Curie temperature, close to 360 K, is attained in the compound $La_{5/8}Sr_{3/8}MnO_3$. The ferromagnetic-paramagnetic transition itself appears to be close to a second order phase transition and the behavior of the system is described by critical indices corresponding (or close) to a three-dimensional Heisenberg ferromagnet. (The specific realization of the metal-insulator transition in manganites with colossal magnetoresistance caused by inhomogeneities in the electronic and magnetic states of the manganites near the Curie temperature is reviewed in Refs. [3.52–3.54]).

In terms of the traditional model proposed by Zener [3.55], magnetic and transport properties of the substituted manganites are generated by the so-called 'double-exchange' interaction. In brief, consider two cations Mn^{3+} and Mn^{4+} located at equivalent crystallographic positions and separated by an O^{2-} anion. The Mn^{4+} ion is in a t_{2g}^3 configuration and the Mn^{3+} ion is in a $t_{2g}^3 e_g^1$ configuration. Because of the large intra-atomic Hund coupling, the three electrons in the t_{2g} level form a localized spin S = 3/2. Due to the same Hund rule, the e_g electron on the Mn^{3+} ion has its spin aligned parallel to the localized spin of the ion. Since the positions of the Mn ions are equivalent, the $Mn^{3+} - O^{2-} - Mn^{4+}$ and $Mn^{4+} - O^{2-} - Mn^{3+}$ configurations are energetically equivalent, i. e., the ground state of the pair is degenerate. It is natural to expect a strong resonance coupling between the two configurations, which can be interpreted as a state of two Mn^{4+} cations with a generalized e_g-electron (or Mn^{3+} cations with a generalized hole). As an e_g-electron moves along the lattice it is energetically favorable that all the localized spins be parallel to one

another, *i. e.*, a ferromagnetic ordering of the localized spins minimizes the kinetic energy of the e_g-electrons. When the substitution degree is sufficiently high, the e_g-electrons form a ferromagnetic metallic state. As a result, in the ground state, all conducting electrons are spin-polarized in the direction of the spontaneous magnetic moment and there are no electrons with opposite spins. This type of metals is referred to as *half-metallic ferromagnet* (hmF), *i. e.*, it is a metal for the majority spin and an insulator for the minority spin [3.56].

Experimental data on manganites with a perovskite structure, where the magnetic ions are ions of a single element with different valences, are in good qualitative and quantitative agreements with this model. For example, Bowen *et al*. curried out the measurements a current's spin polarization in magnetic tunnel junctions with the manganite $La_{2/3}Sr_{1/3}MnO_3$ as the electrode material. The results obtained suggest that the electrode's current spin polarization is at least 95 % [3.57]. That is why for inducing triplet correlations in a singlet SC the high-transmission contacts of half-metallic ferromagnets and SC are most promising ones. Yet, to overcome the spin conservation low and allow for proximity induced triplet amplitudes in the ferromagnet, see Fig. 3.1, one needs an inhomogeneous non-collinear magnetization in the interface region. One such possibility is nanoparticles of hmF manganites.

Nanoparticles. A natural question arises whether the bulk characteristics of manganite are retained in nanosized samples. In Refs. [3.58–3.60] perovskite-type manganese oxide nanoparticles (NPs) with particle sizes of 15–30 nm and 100–200 nm were prepared and studied using ^{55}Mn nuclear magnetic resonance, superparamagnetic resonance, and magnetic measurements. The nuclear spin dynamics results provided direct evidence that the grain boundary of NPs is not sharp in magnetic and electrical respects, but rather should be considered as a transfer region of several (~ two) monolayers with magnetic and structural orders different from the inner part of the grain. The cores of the NPs are magnetically homogeneous. The local structure of the outer shell is that of perovskites yet modified by vacancies, stress, disordering of atoms in perovskite cells and broken bonds on the surface. The Curie temperature, determined as the magnetization onset was close to that in a bulk crystalline sample of the same composition. Electrical transport properties support this physical picture. Hence, the manganites nanoparticle's inner parts

are magnetically identical to a bulk sample of the same composition, and in the inner part the strength of the double exchange interaction and the half-metallic conductivity are preserved.

3.4 Two-dimensional Berezinskii–Kosterlitz–Thouless topological phase transition in three-dimensional nanocomposites

As already noted above, hybrid SC/hmF nano-heterostructures can enable new intelligently tailored functionality and have gained attention over the past few years as promising functional materials for superconducting spintronics. Apart the purpose of superconducting spintronics functional materials, transport properties of SC/hmF *nano*composites have been attracted a fundamental interest themselves, as well. One of the distinctive features of SC/hmF nanocomposites is an unconventional superconducting proximity effect, that determines their important characteristics to be beyond the conventional chaotic two-component nanostructures. Due to the proximity effect in SC/hmF nanocomposites, geometric contacts and electrical connectivity of individual particles are often not the same issue [3.61 - 3.65].

To date, a few works have been reported on the study of transport properties of a SC with half-metallic magnetic nanoparticles composites. Unconventional double percolation transition was identified by Liu *et al.* [3.61] for a binary network composed of MgB_2 superconductor and CrO_2 hmF nanoparticles. It was shown that the double percolation transition (superconductor–insulator–metal) is controlled by volume fractions of the components and originates from the suppressed interface conduction and tunneling as well as a large geometric disparity between particles [3.61]. In Ref. [3.62], Acharya *et al*. prepared and studied electrical transport characteristics of $Bi_2Sr_2CaCu_2O_8/BiFeO_3$ nanocomposite with various weight percentage of superparamagnetic $BiFeO_3$ nanoparticles. Measurement of the critical current density reveals that the superconducting transition temperature splits into two ones, T_{C1} and T_{C2}, along with broadening of overall superconducting transition. Such behavior has been attributed to a weak-link nature of a granular SC as the latter is composed of superconducting grains embedded in a non-superconducting host. The point is that for nanoparticles the geometric contacts and

electrical connectivity of individual particles are often not the same. Of the two superconducting transitions temperatures, the higher one, T_{C1}, marks the superconductivity in grains' balk whereas the grain boundary remains normal, and the lower one, T_{C2}, emerges when the grain boundary becomes superconducting, too.

Conventional Berezinskii–Kosterlitz–Thouless (BKT) transition [3.66–3.68] in the case of superconducting system has topological nature and is associated with a vortex-antivortex (un-) binding [3.69]. At temperatures below T_{BKT}, the vortex-antivortex pairs composite a bound state; for $T > T_{BKT}$, the vortex proliferation takes place, and the system enters a Coulomb gas-type state. This BKT topological transition is general and was observed in many two-dimensional systems, such as superfluid and superconducting films [3.70], two-dimensional spin systems [3.71, 3.72], *etc.* Although the BKT transition is a well-known phenomenon on planar surfaces, for curved spaces the situation is not so clear. The realization of a classical BKT transition in nominally three-dimensional systems has not an obvious case *a priori* [3.73, 3.74], as well.

It is well known that in the vicinity of the BKT transition to a superconducting state the resistance of thin films is described by the expression (see, *e. g.*, the review [3.69] and references therein):

$$R(T) = R_0 \exp\left\{-4\alpha \left[\frac{T_{C0} - T_{BKT}}{T - T_{BKT}}\right]^{1/2}\right\}. \tag{3.1}$$

Here the parameter α is uniquely expressed in terms of the effective mass of the core of a fluctuating vortex and an antivortex. It was shown [3.74] that α is not an arbitrary constant of the order of unity but is causally related to the effective mass μ of the vortex core in a two-dimensional (2D) SC. To be exact, $\alpha = \mu/\mu_{XY}$ where μ_{XY} stands for the mass of the vortex core in the classical XY model. In the most cases, when the two-dimensional nature of the film's superconducting transition is not in doubt, and especially for high-T_C cuprate SCs, the ratio $\alpha = \mu/\mu_{XY}$ turned out to be limited by a rather narrow interval of $1 \lesssim \alpha \lesssim 1.5$ [3.75, 3.76].

3.4.1 s-wave superconductor

In this subsection, we discuss transition from the normal state to super-conducting one in chaotic two-component nanostructures, which are nano-composites consisting of MgB_2 superconductor microparticles and nanoparticles of a half-metallic $La_{2/3}Sr_{1/3}MnO_3$ (LSMO) ferromagnet (see Ref. [3.33]).
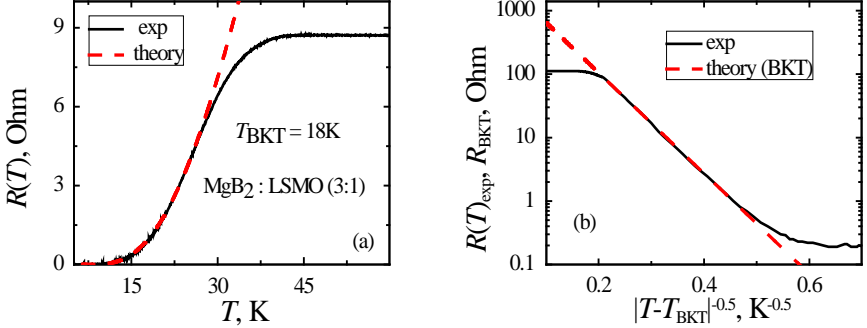

Fig. 3.2 – (a) Experimental (solid curve) and theoretical [dashed curve, Eq. (3.1)] dependences R(T) for the $MgB_2/La_{2/3}Sr_{1/3}MnO_3$ (3:1) nanocomposite. (b) The same dependences represented in a logarithmic scale on the ordinate axis. Adapted from Ref. [3.33]

Figure 3.2(a) displays typical temperature dependence of the nanocomposite resistance $R(T)$ (solid line) in a broad temperature range. In addition to a steep fall of resistance at $T < T_C$ that is typical of manganites (not shown in the plot), there is a virtually linear dependence $R(T)$ in the $T^* < T < T_C$ temperature range that is followed by a significant decrease in resistance at a temperature of $T^* \approx 40$ K $\approx T_{C0}(MgB_2) \approx 39$ K, Fig. 3.2(a). Figure 3.2(b) displays the same dependence in a logarithmic scale on the ordinate axis. The most interesting observation is that the temperature behavior of the resistance at $T < T_{C0}$ is surprisingly well described by Eq. (3.1) [dashed lines in Figs. 3.2(a) and 3.2(b)]. Thus, the $R(T)$ behavior points that in the three-dimensional (3D) nanocomposite, transition to a superconducting state goes through a BKT transition similarly to a 2D system with the transition temperature $T_{BKT} \approx 18$ K and parameter $\alpha = 1 - 1.2$. It should be noted that the theoretical Eq. (3.1) and experimental $R(T)$ dependences agree well in a broad temperature range of $T_{C0} - T_{BKT} \approx 20$ K, where the resistance varies by three orders of magnitude.

The transport characteristics of the nanocomposite also proved to be very sensitive to the external high-frequency (HF) irradiation. Figure 3.3(a) shows the effect of the HF irradiation on resistive transitions in the temperature range $T_{BKT} < T < T_{C0}$. It should be noted that the HF signal applied to the MgB$_2$ sample does not result in significant changes in the $R(T)$ dependence [see the $R(T)$ dependence for MgB$_2$ in Fig. 3.3(a)]. At the same time, the resistance of a nanocomposite increases inder the HF irradiation. The HF-signal caused changes in the current-voltage $(I–V)$ characteristics of the nanocomposite are shown in Fig. 3.3(b). The increase of the resistance and the decrease of the excess current under the influence of a small amplitude of the electromagnetic signal indicate that weak couplings (Josephson-like contacts) in the –MgB$_2$– LSMO–MgB$_2$– chains are suppressed.
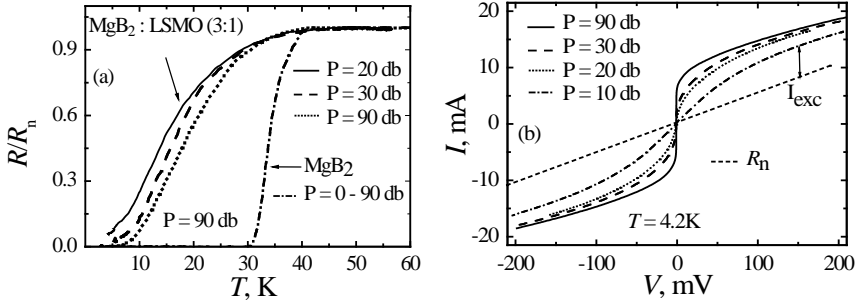

Fig. 3.3 – The effect of the HF irradiation on the (a) resistive transition and (b) current-voltage characteristics of MgB$_2$/La$_{2/3}$Sr$_{1/3}$MnO$_3$ (3:1) nanocomposite. The straight dashed line is plotted to visualize the effect of the HF irradiation on the excess current I_{exc} at $T = 4.2$ K. Adapted from Ref. [3.33]

According to the classical BCS theory of superconductivity, an equilibrium density of Cooper pairs at the temperature T_{C0} exists concurrently with the onset of a dissipation-free state. The superconducting state of the system is described by a complex order parameter

$$\Phi(\mathbf{r}) = |\Phi| \exp\{\varphi(\mathbf{r})\}, \qquad (3.2)$$

where $|\Phi| \equiv \Delta$ is the binding energy of a Cooper pair, and the phase $\varphi(\mathbf{r})$ characterizes the coherent state of Cooper pairs. In the absence of the current in a superconductor, $\varphi(\mathbf{r}) = $ const. In 3D systems, the destruction of super-conductivity usually occurs via vanishing the order-parameter modulus $|\Phi|$,

due to an increase in temperature to T_{C0} or under the action of a magnetic field having a critical magnitude. Distinguishing feature of 2D superconducting systems is that a gas of fluctuations may exist in the form of spontaneously generated magnetic vortices at a temperature below the temperature T_{C0} of the bulk superconducting transition (see, for example, the review [3.69]). The vortices are generated in pairs with opposite directions of ring currents (vortex–antivortex pairs), which annihilate after a finite time because of collisions. In a zero magnetic field, the number of vortices having opposite signs is the same and is determined by the dynamic equilibrium between their spontaneous generation and annihilation. The wave-function phase changes because of going around an immobile vortex by 2π; therefore, the free motion of vortices results in fluctuations of the phase. If the amplitude of the fluctuations is large enough, the coherence of the superconducting state is lost. The order parameter modulus Δ remains non-zero in most of the sample volume (and vanishes only near the vortex axis).

If the temperature decreases, the BKT transition occurs at some temperature T_{BKT} $(< T_{C0})$: vortex pairs are no longer generated, vortex density sharply decreases to become exponentially small, and dissipation becomes exponentially small as well. Thus, in the $T_{BKT} < T < T_{C0}$ temperature range, Cooper pairs coexist in 2D superconductors with vortices. Dissipation decreases due to the presence of Cooper pairs but does not vanish. In samples with defects, the BKT transition broadens due to internal non-uniformities, and this circumstance should be considered to ensure that the numerical estimates of system parameters are correct [3.75, 3.76].

If a sample consists of superconducting granules embedded into a normal (non-magnetic) metal, the superconducting state is destroyed by another mechanism: transition to the resistive state occurring due to the loss of phase coherence in the system with a finite order parameter modulus $|\Phi|$ in individual superconducting granules (see, for example, the review [3.77]). This implies that the system is in the dissipative state, while individual granules remain in the superconducting state. In this case, charge may be transferred from one granule to another via two channels $j_{tot} = j_S + j_N$: by the Josephson current j_S and uncorrelated electrons j_N. If charge is transferred by the Josephson current of Cooper pairs, the phases of the order parameter between granules partici-

pating in the current transfer are correlated, and a macroscopic superconducting state is established between them. However, the Josephson currents can be suppressed by fluctuations, such as due to a large normal resistivity between granules or external influences. Then the charge is transferred between the granules due to single-particle excitations, $j_{\text{tot}} \rightarrow j_{\text{N}} = eN_{\text{e}}$, the concentration of which, N_{e}, is exponentially small in the granules due to their superconducting state: $N_{\text{e}} \propto \exp(-\Delta/T)$ (e is the electron charge). In the general case, a resistive state with a non-zero equilibrium density of Cooper pairs is realized in the system. This is manifested experimentally by the emergence of an excess current in the current-voltage characteristics of the sample.

Specific features of the BKT transitions in superconductor / normal metal (SC/N) proximity structures were studied in Refs. [3.78–3.80]. Particularly, in proximity Pb–Sn film contacts in the temperature range $T_{\text{C0}}(\text{Sn}) \approx 3.75$ K $< T < T_{\text{C0}}(\text{Pb}) \approx 7.3$ K the authors of Ref. [3.78] observed a resistive transition to the superconducting state that reproduces the main features of the BKT transition. In the same temperature range, nonlinear current-voltage characteristics were observed as it had been predicted in Ref. [3.79] for the case of the topological ordering of vortices in 2D superconductors.

Although the layered proximity SC/hmF structures have been actively studied using both experimentally and theoretically (see, for example, reviews [3.26, 3.45, 3.51] and references therein), a satisfactory description of the properties of SC/hmF nanocomposite materials is still missing. As was noted above, main characteristics of SC/hmF nanocomposites (critical transition temperatures, current-voltage characteristics, percolation transition thresholds, etc.), most likely, cannot be quantitatively described by standard percolation models (see a discussion in Refs. [3.33, 3.34]). The analysis of the structure of the MgB_2/LSMO nanocomposite shows that nanosized LSMO grains fully 'cover' the significantly larger MgB_2 granules. This assumption is supported by measurements of sample density after pressing. For example, the density of the MgB_2 plates produced under a pressure of 40–60 kbar is (72 ± 3) % of the MgB_2 single crystal density. The density of the LSMO nanopowder compressed under the same pressure was a mere (68 ± 3) % of the single-crystal density. At the same time, the density of the MgB_2/LSMO (26 % LSMO) composite was (96 ± 3) % of the calculated value. Such a high

composite density indicates that the LSMO nanoparticles 'spread' under high uniaxial pressure across the sample volume, filling in pores that surround large MgB_2 granules.

Under these types of conditions, the onset of superconductivity occurs in each MgB_2 microgranule independently, and BCS-type fluctuations are formed at the temperature of the condensate formation in bulk MgB_2. The magnetic fluxes caused by the magnetization of manganite nanoparticles are coupled to these nanoparticles and no longer fluctuate at temperatures $T \ll T_C$. A resistive state emerges in the nanocomposite, featuring a nonzero equilibrium concentration of Cooper pairs and a frozen magnetic field created by the LSMO nanoparticles. If the temperature decreases further, a (quasi-) two-dimensional structure is most likely formed in the system in the $T_{BKT} < T < T_{c0}$ temperature range; it consists of superconducting granules covered by ferromagnetic nanoparticles (hmF–SC–hmF). The manganite nanoparticles contacting with MgB_2 transitioned to the superconducting (triplet) state induced by the proximity effect [3.28–3.30].

This physical model provides an explanation for the agreement between the observed dependence $R(T)$ (Fig. 3.2) and Eq. (3.1) deduced for 2D systems. Thus, we are dealing with a composite, the main resistive losses of which are caused by current flowing through the ferromagnetic LSMO granules that cover the MgB_2 granules (an analog of a 2D shell / plane). As the temperature decreases, the processes that result in the BKT transition are realized in the two-dimensional superconducting LSMO layers (contacting with MgB_2). In the superconducting state of the nanocomposite, an overcurrent flows through the Josephson-like junctions –SC–hmF–SC–hmF–SC–. If the nanocomposite is irradiated with a small-amplitude HF signal, the currents induced by the HF signal are sufficient to suppress weak Josephson junctions between superconducting LSMO nanoparticles. This contributes to the creation of single-particle charge carriers, which is recorded as the emergence of additional resistance and the decrease in the excess current (Fig. 3.3). That is, in the nanocomposite, the main effect of the high frequency field is the destruction of the coherent state of weakly linked Josephson junctions formed by manganite layers that are in a superconducting state due to the proximity effect (for more details, see Ref. [3.81, 3.82]).

3.4.2 d-wave superconductor

MgB$_2$ is an *s*-wave superconductor. In this subsection, we discuss results of experimental investigations and theoretical analysis of the transition to a superconducting state of random binary nanocomposites of *d*-wave cuprate SC Bi$_2$Sr$_2$Ca$_2$Cu$_3$O$_{6+x}$ (Bi2223) microparticles and hmF La$_{2/3}$Sr$_{1/3}$MnO$_3$ (LSMO) nanoparticles – Bi2223/LSMO nanocomposites [3.34, 3.35].
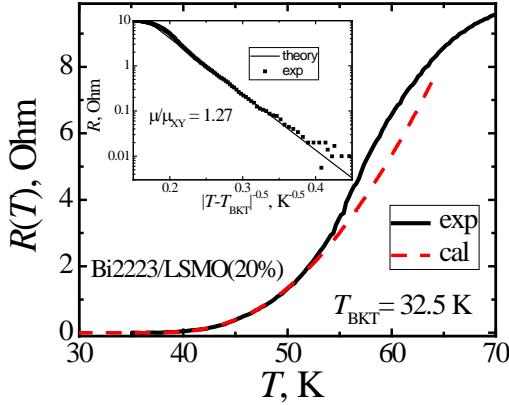

Fig. 3.4 – The nanocomposite's (20 % LSMO) resistance temperature dependence. *Main panel:* Experimental, black solid curve, and theoretical, Eq. (3.1), red dashed curve, $R(T)$ behavior. *Insert*: Effective $\alpha = \mu/\mu_{XY}$ where μ_{XY} is the vortex core mass in the classical XY model. Adapted from Ref. [3.35]

Figure 3.4 displays experimental temperature dependence of the 20 vol. % of LSMO nanocomposite (black solid line) resistance $R(T)$ in a temperature range below T_{C0} of Bi2223. In addition to a steep fall of resistance at $T < T_{C0}$, there is a virtually parabolic dependence $R(T)$ in the temperature range ~ 30–60 K that is followed by a significant decrease in resistance. The most interesting observation is that the nanocomposite's resistance temperature behavior at $T < 55$ K is surprisingly well described by Eq. (3.1), red dashed curve in Fig. 3.4. It should be noted that the theoretical Eq. (3.1) and experimental $R(T)$ dependences agree well in a broad temperature range of $\Delta T \approx 32 \div 55$ K, where the resistance R varies by three orders of magnitude. Such $R(T)$ dependence points that the 3D nanocomposite goes through the BKT-like transition similarly to a 2D system with the transition temperature $T_{BKT} \approx 32.5$ K and the parameter α equals to ≈ 1.27.

In the context of the genuine BKT transition broadening in inhomogeneous layered SCs, the temperature behavior of the *I–V* characteristic should correspond to the dependence $V \sim |I|^{a(T)}$, with the exponent $a(T_{BKT}) = 3$ and $a(T) \to 1$ above T_{BKT} [3.75, 3.76, 3.79, 3.80]. Figure 3.5 (a) displays a logarithmic plot of *I–V* characteristics of the sample with 20 % LSMO at temperatures spanning the range $T_{BKT} \leq T < T_{C0}$. At $T = 52.5$ K the *I–V* curve is approximately linear, while at T_{BKT}, $V \sim I^3$. Experimental (points) temperature dependence of the parameter $a(T)$ in $V \sim |I|^{a(T)}$ dependence is shown in Fig. 3.5 (b), as well. The choice of T_{BKT} which provides the best fit to the resistance theory [3.79, 3.80] also corresponds to the value at which the *I–V* curves have an exponent $a(T_{BKT}) \approx 3$. Again, we have observed that the transition to a superconducting state, the 3D nanocomposite's *I–V* characteristics, are well described within a 2D topological transition approach and is associated with the BKT-like superconducting transition [3.75, 3.76, 3.79, 3.80].
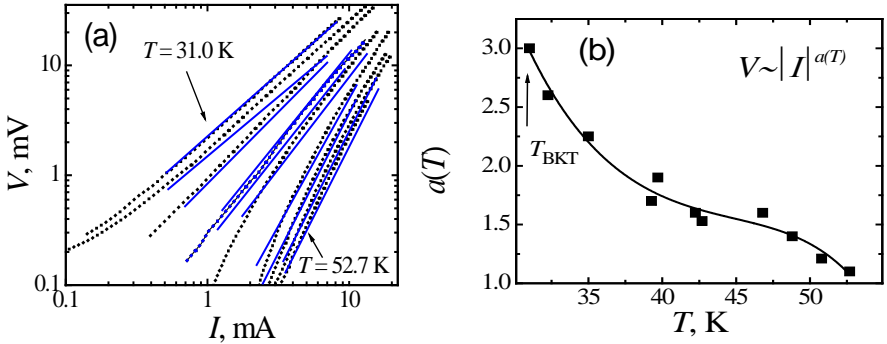

Fig. 3.5 – (a) Logarithmic plot of *I–V* characteristics of the sample 20 % LSMO at temperatures spanning the range $T_{BKT} \leq T < T_{C0}$ ($T = 31.0$ K, 32.3 K, 39.3 K, 39.7 K, 42.3 K, 42.7 K, 46.8 K, 48.8 K, 50.8 K, 52.7 K); points – experiment, blue solid lines – theory. (b) Experimental data (points) and quadratic approximation (solid line) for the temperature dependence of the parameter $a(T)$, $V \sim |I|^{a(T)}$. Adapted from Ref. [3.35]

As in the case of the MgB$_2$/LSMO nanocomposite, it is naturally to suggest that the Bs2223/LSMO sample's resistivity distinctive features are determined by an inhomogeneous spatial distribution of the local superconducting grains coupled by Josephson currents. The validity of the experimental data interpretation has been supported by the effect of an external HF radiation on the nanocomposite's transport characteristics.
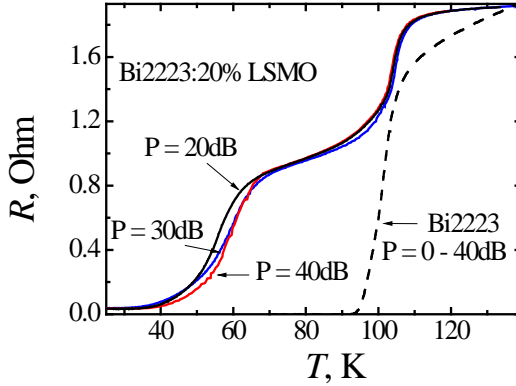
Fig. 3.6 – Effect of the HF radiation ~ 100 MHz on the resistive transition of a Bi2223 sample and nanocomposites with 20 % of LSMO. Adapted from Ref. [3.35]

Figure 3.6 demonstrates the effect of the HF irradiation on resistive transitions in the temperature range $T < T_{C0}$ in the nanocomposites Bi2223/20%LSMO and in compacted Bi2223 sample. As it is shown in Fig. 3.6, the HF signal applied to the compacted Bi2223 sample does not cause noticeable changes in the $R(T)$ dependence. At the same time, when the nano-composite is a subject of the HF irradiation, a tail with an upward curvature change demonstrating increasing resistance. This is typical for the fluctuation resistivity near the T_{BKT} transition [3.77] when the resistive tail can be attributed to the inhomogeneous spatial distribution of the local superfluid, caused by intrinsic inhomogeneous density distribution in the systems.

The changes in the I-V characteristics of the 20 % LSMO nanocomposite's superconducting state under the HF radiation are shown in Fig. 3.7. At small amplitudes of the electromagnetic signal, an increase in the resistance and a decrease in the excess current indicates that weak couplings (Josephson-like contacts) are suppressed in the –Bi2223–LSMO–Bi2223– chains. Thus, the transport characteristics of the 3D nanocomposite are extremely sensitive to the external HF radiation.

Thus, as for the MgB2/LSMO nanocomposite, in the case of the Bi2223/LSMO nanocomposite the proximity effect possesses a few specific peculiarities.
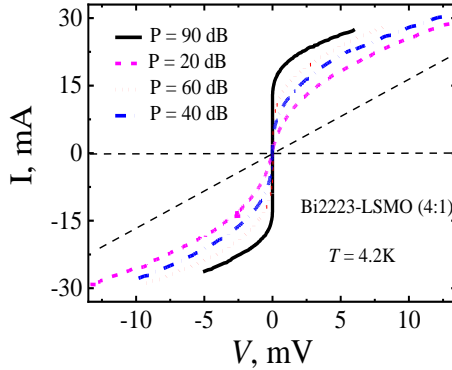
Fig. 3.7 – Effect of the HF radiation ~ 100 MHz on current-voltage characteristics of the nanocomposite with 20 % LSMO. Adapted from Ref. [3.35]

First, because the contacts between Bi2223 grains are in the bulk through the half-metallic LSMO *nano*grains, this causes significant broadening of the nanocomposite transition to a superconducting state. Second, for high-T_C SCs with a *d*-wave Cooper pair symmetry [3.26], theory predicts, and experiment provides evidence that in proximity coupled *d*-wave SC/ferromagnet structures an unconventional (spin-triplet) superconducting state can be generated. This also means that in the nanocomposite a new geometrical length has been generated that characterizes unconventional superconducting state (a mixture of *d*-wave singlet and *p*-wave triplet Cooper pairs) in the proximity-coupled regions.

3.4.3 Discussion

The main physical message of the experimental data shown in Figs. 3.2–3.7 is that the observed Berezinskii–Kosterlitz–Thouless-like behavior of the transport properties of nanocomposites are due to two scales typical for this type of systems. Namely, they are (i) a significant difference between the geometric dimensions of the components and (ii) a *p*-wave superconducting state of the LSMO nanoparticles induced by the proximity effect.

In bulk (three-dimensional, 3D) composite systems superconductivity has been studied within the percolation scenario. It is well established, when the grains of a superconducting material, *d*, are large enough, $d \gg \xi_S$, their basic

intra-granular characteristics (critical temperature, superconducting gap, etc.) are not affected by the proximity of the non-superconducting component and remain close to the bulk value of a quantity both above and below a percolation threshold. For a bulk composite with roughly the *same geometrical size* of components, the lattice percolation model [3.83–3.85] predicts $f_C = 0.16 \pm 0.02$ for the percolation threshold of the volume fraction, f, of a superconducting component (f_C being a percolation threshold of superconducting grains with the linear dimensions $\gtrsim \xi_S$). Thus, according to the conventional lattice percolation model, for the nanocomposite systems under consideration with large grains of the superconducting material, above the percolation threshold of the volume fraction f_C, the macroscopic transition temperature T_C should not be strongly dependent on the contents variation. However, even for the SC/hmF samples with the volume fraction $f \sim 0.6$, *i. e.*, about three times larger than the conventional percolation model predicts, there is no transition into a superconducting state. Moreover, as it follows for the $R(T)$ data [3.33, 3.35] the transition temperature T_C is strongly reduced for the samples with 80, 75, and 70 vol. % of the superconducting component (20, 25, and 30 vol. % of LSMO), *i. e.*, even at concentrations when an infinite percolating cluster of MgB_2 or Bi2223 grains should be formed. Thus, the predictions based on the conventional percolation models fail for the *s-(d-)*-wave SC/hmF nanocomposites most probably due to two factors: (i) essential difference in the components' geometrical size and (ii) unconventional (spin-triplet) superconducting proximity effect.

As is known, below the superconducting transition, an indirect (due to the proximity effect) coupling between constituent components emerges. In SC/hmF heterostructures a long-range proximity effect will be realized effectively, and a triplet component of anomalous correlations should be taken into consideration if there is a spatial variation of the magnetization at the ferromagnet surface [3.23–3.26, 3.37–3.43, 3.86–3.90]. Characteristic coherence length of triplet correlations $\xi_F = (D_F/2\pi T)^{1/2}$ can be as large as ~ 100 nm at low temperatures. In previous works, anomalous superconductivity has been indeed detected in SC/hmF nanostructures [3.30, 3.38] and in SC/hmF junctions [3.23, 3.25, 3.28, 3.39]. It was argued that at low temperatures, manganites are thermodynamically close to a superconducting state with a triplet

p-wave even frequency pairing [3.28–3.30, 3.36]. Being proximity coupled to a singlet SC, the $m = 0$ triplet wave-function component is coupled in the manganite via the boundary condition to the singlet pairing amplitude in the SC counterpart. At the same time, the spin-active boundary leads to coupling of the $m = 0$ triplet component with an equal-spin, $m = 1$, pairing amplitude in the manganite. These couplings yield phase coherency of both $m = 0$ and equal-spin $m = 1$ triplet Cooper pairs in the hmF manganite. Dependence of the scale of superconducting correlations on the intrinsic magnetic field in-homogeneity is a feature of the proximity effect in mesoscopic hmF/SC struc-tures [3.26, 3.43, 3.44, 3.51, 3.86 - 3.90].

Under these specific conditions, the nanocomposite's transition to a super-conducting state, most probably, is followed the next 'evolution scenario'. The onset of superconductivity occurs independently in each SC microgranules at the temperature of superconducting condensate formation in the bulk SC. Magnetic fluxes are caused by the manganite nanoparticles' magnetization and at temperatures $T < T_{C0} < T_{Curie}$ (LSMO) magnetic fluxes are confined to the manganite nanoparticles. That is, in the temperature range $T_{BKT} < T < T_{C0}$, a resistive state emerged in the nanocomposite is featured by a nonzero equilibrium concentration of Cooper pairs in the SC microparticles and frozen magnetic vortices created by the LSMO nanoparticles. A 3D structure is formed in the system. It consists of the superconducting granules covered by the ferromagnetic nanoparticles: –hmF–SC–hmF–SC– 'brickwork' structure. If the temperature decreases further, BKT-like superconducting correlations in the bulk *s-(d-)*-wave SC/LSMO nanocomposite emerge due to the emergence of the effective 2D percolation cluster of a specific superconducting state. Namely, the 2D supercurrent percolation is fulfilled through hmF nanopar-ticles layer following the 'brickwork' scheme. Due to the proximity effect at magnetically inhomogeneous SC-LSMO interfaces, the superconducting state of the percolation layer is a mixture of *s-(d-)*-wave singlet and *p*-wave triplet Cooper pairs.

3.5 Triple-gap superconductivity of MgB₂–(La, Sr)MnO₃ nanocomposite

Another topic of nowadays fundamental interest is a spatial inhomogeneity in the superconducting density of states and the superconducting state, which is governed by quantum phase fluctuations [3.91–3.95]. Most mean-field theories assume that the relation $T_\phi > T_\Delta$ is fulfilled between the temperatures of electron pairing T_Δ and the long-range phase coherency T_ϕ. This means that global phase coherency and the energy gap appear (vanish) at the same temperature, mainly due to the opening (disappearing) of the gap with temperature. However, it has been shown (see, *e. g.*, reviews [3.77, 3.91]) that for systems with low conductivity and small superfluid density (bad metals), the temperature of the global phase coherency T_ϕ is reduced significantly and becomes to be comparable to or even smaller than the pairing temperature T_Δ. In this case, the critical temperature T_C is determined by the global phase coherency, whereas a local pair condensate could exist well above T_C. For high-T_C cuprates diamagnetism due to fluctuating superconducting pairs above the superconducting transition temperature as well as the origin of the so-called pseudogap still remain under discussion (see, *e. g.*, Refs. [3.92–3.95] and references therein). A new stimulus for active debates in this area is motivated by the search for materials with triplet fluctuation superconductivity.

At energies below the superconducting gap, the charge transport through a normal nonmagnetic (N) metal in contact with a SC is possible only due to a specific process called Andreev reflection (AR) [3.49, 3.96–3.98]. This is a two-particle process in which, in the N metal, an incident electron above the Fermi energy E_F and an electron below E_F with the opposite spin are coupled together and transferred across the interface into the SC side, forming a Cooper pair in the condensate. Simultaneously, an evanescent hole with opposite momentum and spin emerges in the N metal. The charge doubling at the interface enhances the sub-gap conductance and this phenomenon has indeed been observed in the case of a perfectly transparent interface. The picture is significantly modified when spin comes into play. If the N metal is a half-metallic ferromagnet, there is full imbalance between spin-up and spin-down populations, which suppresses the AR and reduces the sub-gap conductance to zero.

According to the existing publications [3.99–3.102] the charge carrier polarization for LCMO is large, greater than 75 %. Thus, if a supercurrent in

the composite is unpolarized [an *s*-wave or a *p*-wave ($S = 1$, $m = 0$) component of triplet pairing] the AR will be suppressed, and the sub-gap conductance will be reduced below the normal-state value. On the contrary, if at both sides of the contact the charge current is spin polarized, there is no restriction (because of spin) on the AR and, as in the conventional case [3.96–3.98] an excess current and a doubling of the normal-state conductance are observed.

Figure 3.8 shows representative dynamic conductance spectra $dI/dV = G(V)$ of micro-constrictions between In, Ag, and Nb tips and the sample 3:1 (a configuration commonly called the 'needle anvil') measured at $T = 4.2$ K. At low voltages, conductance peaks corresponding to *three* superconducting gaps with energies $\Delta(\pi) = 2.0 - 2.4$ meV, $\Delta(\sigma) = 8.4 - 11.7$ meV, and $\Delta_{tr} = 19.8 - 22.4$ meV are clearly observed. (In the figure, the position of the dI/dV minimum is denoted by Δ. For PCs with not too large lifetime-broadening effects, this value does not differ much from the proper energy gap [3.103]). Two of the gaps, $\Delta(\pi)$ and $\Delta(\sigma)$, were identified as MgB_2 gaps (to be precise, as ones originating from the $\Delta(\pi)$ and $\Delta(\sigma)$ gaps of MgB_2, respectively). The magnitude of the smallest $\Delta(\pi)$ gap remains in the range of the bulk MgB_2 gap [3.104]; the gap $\Delta(\sigma)$ was recognized as *enhanced* MgB_2 $\Delta(\sigma)$ gap.

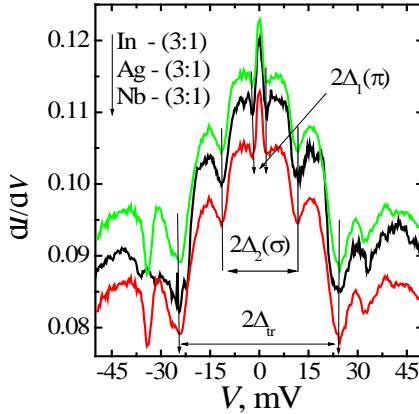Fig. 3.8 – Point-contact Andreev reflection spectra of In, Ag, and Nb tips and $MgB_2/La_{0.67}Sr_{0.33}MnO_3$ (3:1) nanocomposite; $T = 4.2$K. Adapted from Ref. [3.30]

The third gap, Δ_{tr}, the authors [3.30] attributed to the intrinsic super-conducting pairing in the (La, Sr)MnO_3 compound. The absolute value of Δ_{tr} is the same as those also detected in PCs of (La, Sr)MnO_3 and (La,Ca)MnO_3

with Pb or MgB$_2$ [3.28, 3.29, 3.102]. The magnitude of Δ_{tr} is more than *three times larger* than the largest 'parents' $\Delta(\sigma) = 6.8–7.1$ meV MgB$_2$ gap [3.104]. Note that the PCs' resistivity varied by orders of magnitude, while the multiple-gap structure in the quasiparticle density of states, as well as the gap energy values, were robust features and reproduced in all PCs have been prepared.

In Fig. 3.9, we present an experimental temperature dependence of the energy gap $\Delta_{tr}(T)$ [3.30]. For comparison, the conventional Bardeen–Cooper–Schrieffer BCS gap temperature behavior is shown in the figure, too. From the BCS relation $\Delta(0) = 1.76 k_B T_C$, the $\Delta_{tr}(0) = 19.8–22.4$ meV gap would lead to a superconducting state with $T_C \approx 120$ K. Yet, the energy gap $\Delta_{tr}(T)$ vanishes as the temperature increases towards $T_C \approx 39$ K of MgB$_2$. Evidently, the experimental behavior of $\Delta_{tr}(T)$ does not follow the BCS dependence. The temperature dependence of the largest gap detected, $\Delta_{tr}(T)$, directly proves that its emergence is not an 'independent' property but is due to the superconducting state of MgB$_2$, *i. e.*, due to the proximity effect.

The results presented in Figs. 3.8 and 3.9 convincingly show that, at low temperatures, a noncoherent *p*-wave even-frequency spin-triplet superconducting condensate already exists in half-metallic manganites. Being proximity coupled to the singlet SC, the $m = 0$ triplet component in the manganite is coupled via the boundary condition to the singlet pairing amplitude in the SC partner.
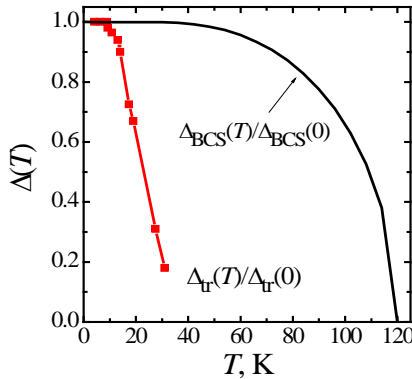

Fig. 3.9 – Experimental (square points) $\Delta_{tr}(T)$ gap temperature behavior (normalized to the zero-temperature gap) of the MgB$_2$/La$_{0.67}$Sr$_{0.33}$MnO$_3$ (3:1) nanocomposite and the BCS gap temperature dependence (black solid line). Adapted from Ref. [3.30]
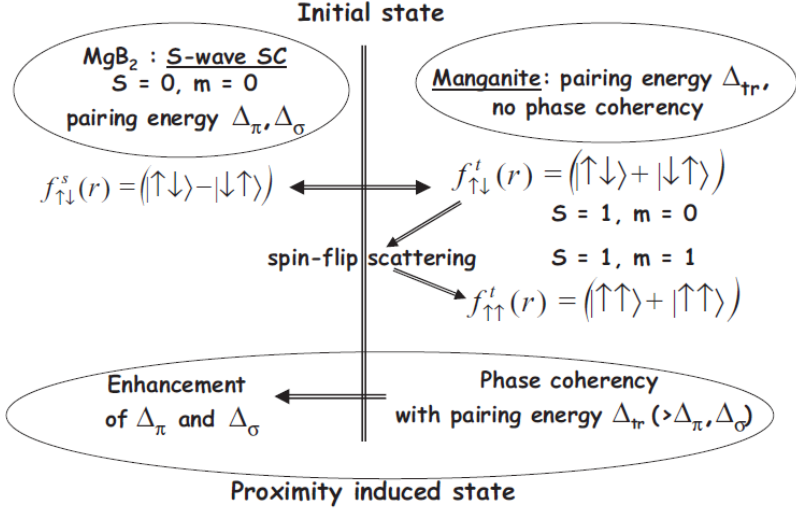
Initial state

Fig. 3.10 – A sketch of the long-range phase coherency due to the proximity effect in the SC/hmF nanostructures. Adapted from Ref. [3.30]

At the same time, the spin-active boundary leads to coupling of the $m = 0$ triplet component with an equal-spin, $m = 1$, pairing amplitude in manganite. These couplings yield phase coherency of both $m = 0$ and equal-spin $m = 1$ triplet Cooper pairs in the HMF with a large quasiparticle gap Δ_{tr} ($> \Delta_\pi$, Δ_σ). As an inverse effect, being proximity linked to the s-wave pairing amplitude, the $m = 0$ amplitude of the triplet superconducting state enhances the quasi-particle gap(s) of a singlet SC. Fig. 3.10 illustrates the described mechanism of the long-range phase coherency due to the proximity effect in the nanocomposite.

3.6 Local triplet superconductivity of half-metallic manganites

As was noted above, the transition to the superconducting state is accompanied and is caused by a rearrangement of the electronic spectrum with the appearance of a gap at the Fermi level. The state is characterized by a complex order parameter (see, e. g., reviews [3.77, 3.91]):

$$\Delta(\mathbf{r}) = |\Delta(\mathbf{r})|\exp\{i\varphi(\mathbf{r})\}, \tag{3.3}$$

where the modulus of the pairing energy, namely $2|\Delta(\mathbf{r})|$, is the gap value in the electronic spectrum. In the mean field theory, temperatures of the electron-pairing effect, T_Δ, and the long-range (global) phase coherency, T_φ, coincide and yield the critical temperature, T_C. This implies that the spatial variations in $|\Delta(\mathbf{r})|$ are small, and that global phase coherence temperature T_φ is larger than (or equal to) T_C.

In a system with a small superfluid density (bad metals with an electron concentration that is substantially less than that characteristic of conventional metals) the spatial variations / fluctuations in the order parameter $\Delta(\mathbf{r})$, *e. g.*, due to thermal effects, become crucial in the regions where pairing energy value $|\Delta(\mathbf{r})|$ is small. As the result, in a bad metal, thermal fluctuations in the global phase coherency of the order parameter are the most important ones. The fluctuations of the order parameter phase $\varphi(\mathbf{r})$ in mesoscopic 'islands' prevent the long-range superconductivity. Therefore, for systems with low conductivity and small superfluid density, the temperature of the system's global phase coherency T_φ can be reduced significantly and could be smaller than the 'islands' pairing temperature T_Δ. Then the superconducting transition temperature T_C is determined by the global phase coherency, whereas the pair condensate could exist well above $T_C = T_\varphi < T_\Delta$ [3.77, 3.91–3.95].

An important consequence of Cooper pairs fluctuation above the transition temperature T_C is the appearance of the so-called pseudo-gap [3.77, 3.92–3.95], *i. e.*, a reduction of the single-electron density of states near the Fermi level. According to the viewpoint expressed in Ref. [3.92], the pseudo-gap state in high-T_C cuprates could be considered as an unconventional metal, i. e., as a SC which has lost its phase stiffness due to phase fluctuations. Doped manganites belong to bad metals, and a large pseudo-gap is detected in numerous experiments on manganites [3.105–3.108]. It may be suggested that at least a part of the observed pseudo-gap value is due to pairing without the global phase coherency. In cuprates, an additional argument for the local pair's condensate existence at $T > T_C$ is a diamagnetism observed just above T_C, i. e., when temperature $T_\varphi < T < T_\Delta$ (see, *e. g.*, Refs. [3.109, 3.110]). For manganites, however, this kind of the superfluid density precursor can be strongly suppressed by a ferromagnetic order of the localized moments and a spin-triplet state of the pair condensate.

As noted above, materials realizing spin-triplet *p*-wave pairing are a subject of special interest. This interest is motivated as systems where specific topologically protected quasiparticle excitations can be realized and as promising materials yielding novel technological applications. Long-range proximity effects interpreted in terms of singlet-to-triplet pairing conversion have been found in various SC/F systems [3.40, 3.41, 3.43, 3.51]. Among these systems, the half-metallic-based SC/F heterostructures, where long-range proximity effect has been experimentally observed, have attracted especial attention [3.24–3.26, 3.51]. As was shown theoretically, for the SC/F systems, long-range proximity effect and singlet-to-triplet pairing conversion can be realized due to interfacial magnetic inhomogeneities. Eschrig *et al.* showed that when normal metal is half-metallic ferromagnet, even frequency pairing would be mostly of the *p*-wave symmetry [3.111].

These results are compelling arguments that proximity induced superconducting transition in doped manganites follows the scenario of a 'latent' high-T_C superconductivity in doped manganites. At low temperatures, incoherent superconducting fluctuations are essentially sustained in half-metallic manganites. Although the local gap amplitude is large, there is no phase stiffness, and the system is incapable of displaying a long-range superconducting response. Nonetheless, a local phase rigidity (a local triplet pairing condensate) survives, and, in a proximity-affected region, the singlet SC establishes phase coherence of the *p*-wave spin-triplet superconducting state of the manganites [3.28–3.30].

3.7 Bosonic scenario of a local triplet superconductivity of half-metallic manganites

Let us make some suggestions concerning the mechanism of coupling spin-polarized conducting electrons in manganites and the origin of the quasiparticle gap Δ_{tr} whose magnitude cannot be explained in terms of the conventional proximity-effect theory.

In the context of manganite's half-metallic conductivity in the ferromagnetic state, a natural question arises about triplet superconductivity due to magnon coupling. The replacement of a phonon by a spin wave should not

lead to a drastic modification of superconducting properties. However, there is an important difference between these couplings [3.112]. Namely, a spin-wave excitation (magnon) carries a spin with the projection opposite to the ferromagnet magnetization direction and in the nonrelativistic approach, the projection of the total spin of both conducting and localized electrons is preserved. This means that if the magnon exchange results in equal-spin triplet pair states $\Delta_\uparrow$ or $\Delta_\downarrow$, neither $\Delta_\uparrow$ state, nor $\Delta_\downarrow$ one can exist without each other since the magnon carries spin $|S| = 1$ and thus the attraction of two electrons with the *same* spins, $+1/2$ (or $-1/2$) due to spin-wave exchange is forbidden by the spin conservation law. As Bulaevskii *et al.* showed [3.112], the spin-wave exchange mechanism leads to equal spin-triplet pairing but the resulting superconducting state is described by the two-component order parameter, $f^{\mathrm{tr}}(r) = g_1(r)|\uparrow\uparrow> + g_2(r)|\downarrow\downarrow>$, and *excludes a singlet $m = 0$ pairing*, $f^{\mathrm{tr}}_{\uparrow\downarrow}(r) = g_0(r)(|\uparrow\downarrow> + |\downarrow\uparrow>)$.

The conclusion that the magnon exchange excludes a singlet pairing is important in the context of the experimental results [3.28–3.31]. Broken a spin-rotation symmetry at *s*-wave SC – half-metallic manganites interface leads to spin-flip processes at the interfaces. Its origin depends on the microscopic magnetic state at the interface, the character of local magnetic moments coupling with itinerant electrons, etc. (see, e. g., [3.26, 3.51] and references therein). Due to spin mixing at the interfaces, a spin triplet ($S = 1$, $m = 0$) amplitude $f^{\mathrm{tr}}_{\uparrow\downarrow}(r) = g_0(r)(|\uparrow\downarrow> + |\downarrow\uparrow>)$ is induced by the singlet component in the *s*-wave SC, $f^{s}_{\uparrow\downarrow}(r) = g_s(r)(|\uparrow\downarrow - |\downarrow\uparrow)$, and extends from the interface for about the magnetic length $\xi_F = (D_F/2\pi H_{\mathrm{exc}})^{1/2}$ into the manganites layer. At the same time, triplet pairing correlations with equal spin pairs: $f^{\mathrm{tr}}_{\uparrow\uparrow}(r) = g_1(r)|\uparrow\uparrow>$, $m = +1$ or $f^{\mathrm{tr}}_{\downarrow\downarrow}(r) = g_2(r)|\downarrow\downarrow> m = -1$, are also induced (due to spin-flip processes) in the half-metallic layer. These components decay on a 'conventional' length scale $\xi_T = (D_F/2\pi T)^{1/2}$ which is much larger than ξ_F because in typical cases the exchange field H_{exc} is much larger than T_C. It is worthy to emphasis that only the $m = 0$ triplet component $f^{\mathrm{tr}}_{\uparrow\downarrow}(r) = g_0(r)(|\uparrow\downarrow> + |\downarrow\uparrow>)$ is coupled via the spin-active boundary condition to the equal-spin $m = 1$ pairing amplitudes in the half-metal. The singlet component in the *s*-wave superconductor, $f^{s}_{\uparrow\downarrow}(r) = g_s(r)(|\uparrow\downarrow - |\downarrow\uparrow)$, being invariant under rotations around any quantization axis, cannot directly involved in the creation of triplet $m = \pm1$ pairing

amplitudes in the half-metal. Taking this into account, the observed *enhancement* of MgB$_2$ *even-frequency singlet* Cooper pair coupling energy $\Delta(\sigma)$ means that in the manganite the $m = 0$ *even-frequency triplet* component exists, *i. e.*, the proximity induced superconducting state is described by the two-component order parameter, $f^{\mathrm{tr}}(r) = g_1(r)|\uparrow\uparrow\rangle + g_2(r)(|\uparrow\downarrow\rangle + |\downarrow\uparrow\rangle)$. The $m = 0$ triplet component $f^{\mathrm{tr}}_{\uparrow\downarrow}(r)$ is coupled via the boundary condition to the singlet pairing amplitude in the SC partner and, in this case, we deal with the 'mutual' proximity effect. As well, this points out that the most realistic coupling mechanism of the *p*-wave triplet superconductivity in half-metallic manganites is that caused by the *phonon* exchange.

As already mentioned, one of the Cooper pairs fluctuation fingerprints is the so-called pseudogap [3.77, 3.91–3.95], the reduction of the single-electron density of state near the Fermi level. At the Fermi level vicinity of manganites, a large pseudogap is observed [3.105, 3.109, 3.113, 3.114]. This experimental fact supports the hypothesis that a noncoherent *p*-wave even-frequency spin-triplet superconducting condensate already exists in half-metallic manganites at low temperatures [3.28–3.31]. Being proximity coupled to a singlet SC, the $m = 0$ triplet component in the manganite is coupled via the boundary condition to the singlet pairing amplitude in the SC counterpart. At the same time, the spin-active boundary leads to coupling of the $m = 0$ triplet component with an equal-spin, $m = 1$, pairing amplitude in manganite. These couplings yield to a phase coherency of both the $m = 0$ and equal-spin $m = 1$ triplet Cooper pairs with a large quasiparticle gap $\Delta_{\mathrm{tr}} > \Delta(\pi), \Delta(\sigma)$. As an inverse effect, being proximity linked to the *s*-wave pairing amplitude, the $m = 0$ amplitude of the triplet superconducting state enhances the quasiparticle gap(s) in a singlet SC. Figure 3.10 illustrates the described mechanism of the long-range phase coherency due to the proximity effect in half-metallic manganites.

3.8 Half-metallic manganites – a perspective platform for high-temperature triplet superconductivity

At the actual stage of the search for topological quasiparticles in condensed matter, it is crucially desirable to identify (i) easy-to-fabricate systems possessing topological states and (ii) a way by which topologically protected

excitations can be distinguished from spurious effects. Specifically, the realization of a topological superconducting phase and Majorana quasiparticles is of the grand interest because of their novelty as well as possible applications in quantum devices. Thereupon, a convincing proof and undoubted detection of Majorana quasiparticles is among the main challenges in the general trend.

There is a variety of proposals for transforming a conventional *s*-wave SC into topological states supporting Majorana fermion excitations. For instance, realizations of Majorana bound states are expected in semiconducting-superconducting hybrid nanostructures, where the interplay between intrinsic spin-orbit coupling, proximity induced superconductivity, and external magnetic field leads to the formation of zero-energy bound states [3.17–3.21, 3.115–3.119]. An isolated zero-energy topological bound state appears in a spinless *p*-wave SC at the transition between strong- and weak-pairing phases. It is expected [3.119–3.123] that one or more Majorana bound states can appear at the opposite ends of a quantum nanoparticle wire proximity coupled to an *s*-wave SC in the presence of an applied Zeeman field. Yet, while the time-reversal symmetry can be readily broken by a magnetic field, a spin-orbit coupling is too weak to effectively break the spin-rotation symmetry and to drive the system into topologically nontrivial phase by this Kitaev scenario [3.124].

In Ref. [3.17] Choy *et. al.* proposed an alternative to Kitaev route to Majorana fermions in *s*-wave SCs that does not at all require materials with spin-orbit coupling and external Zeeman field. The authors considered a system formed by magnetic nanoparticles on a superconducting substrate. The magnetic moments are frozen, without any dynamics of their own. The nanoparticles magnetic moment breaks time-reversal symmetry as well as spin-rotation symmetry, without the need for spin-orbit coupling in the SC. The superconducting substrate induces a pairing energy in the nanoparticles, so that the system's single-band Hamiltonian has the same form as Kitaev spinless *p*-wave superconducting chain. The difference is that here the *p*-wave pairing is obtained from *s*-wave pairing due to the coupling of the electron spin to local magnetic moments (the proximity effect). In the nanoparticles wire, the transition into the topologically nontrivial superconducting phase is governed by the competition of two types of disorder: (i) variation in the

orientation of the magnetic moments on nearby nanoparticles and (ii) disorder in the hopping energies that localizes the states. The zero-energy bound states in the proximity induced p-wave superconducting gap, having a nonzero magnetic moment, should behave as Majorana bound states [3.17].

In the context of Ref. [3.17] conclusions, we can suggest that nanostructures based on the s-wave SC substrate and hmF manganites nanoparticles are the most promising and accessible systems in which Majorana fermions can be generated. Indeed, all prerequisites listed in Ref. [3.17] can be realized in the heterostructures where magnetic nanoparticles are $(La_{1-x}R_x)MnO_3$, R = Ca, Sr, ... ones. Due to the ferromagnetic half-metallic state of the manganites, the needed p-wave superconductivity in the system is induced undoubtedly due to the proximity effect [3.28–3.31]. The key feature of these heterostructures is the magnitude of the proximity induced triplet superconducting gap Δ_{tr}, i. e., *the magnitude of the topological pairing gap*. In manganite nanoparticles, this gap will be more than three times larger than the largest gap among s-wave SCs – the $\Delta(\sigma)$ gap MgB_2 [3.104]. Therefore, we believe that the manganite $(La_{1-x}R_x)MnO_3$ nanoparticles depositing on a s-wave SC are the most promising materials where *high-temperature topological superconducting states* can be realized. However, to our best knowledge, these systems are not yet studied in detail.

3.9 Conclusion

Systematic character and repeatability of the key experimental observations that have been detected by the point-contact Andreev reflection spectroscopy on the superconductor-half-metallic manganite heterostructures identify some general physical phenomena in transport properties of proximity coupled singlet superconductor-half-metallic manganite nanostructures. It was found that superconductor–half-metallic manganite hybrids provide an experimental possibility to accomplish artificial materials where a topologically nontrivial superconducting state and Majorana fermions can be realized. The basic factor of these conclusions is a local (fluctuated) high-temperature triplet superconductivity in half-metallic manganites. Although the local gap amplitude is large, there is no phase stiffness, and the system is incapable of displaying a

long-range superconducting state. Nonetheless, local phase rigidity survives and being proximity coupled to a superconductor, the long-range coherency is restored. The experimental evidence of the latent spin-triplet superconductivity in half-metal manganites allows to design an experimentally accessible way for overcoming bottleneck of spin-triplet pairing induced in proximitized structures of spin-singlet superconductors with time-reversal symmetry breaking counterparts and opens a new framework in topological superconductivity. Further experimental and theoretical works are needed to prove (or disprove) this platform for engineering topological superconductors and Majorana fermions.

3.10 References to chapter 3

3.1 Žutić I., Fabian J., Das Sarma S. Spintronics: Fundamentals and applications. *Rev. Mod. Phys*. 2004. V. 76. P. 323–410.

3.2 Anders S., Blamire M. G., Buchholz F.-Im., Crété D.-G., Cristiano R., Febvre P., Fritzsch L., Herr A., Il'ichev E., Kohlmann J., Kunert J., Meyer H.-G., Niemeyer J., Ortlepp T., Rogalla H., Schurig T., Siegel M., Stolz R., Tarte E., ter Brake H. J. M., Toepferm H., Villegier J.-C., Zagoskin A. M., Zori A. B. European roadmap on superconductive electronics – status and perspectives. *Physica C*. 2010. V. 470. P. 2079–2126.

3.3 Tao Y. C., Hu J. G. Superconducting spintronics: Spin-polarized transport in superconducting junctions with ferromagnetic semiconducting contact. *J. Appl. Phys*. 2010. V. 107. P. 041101.

3.4 Linder J., Robinson J. W. A. Superconducting spintronics. *Nature Phys.* 2015. V. 11. P. 307–315.

3.5 Eschrig M. Spin-polarized supercurrents for spintronics: a review of current progress. *Rep. Prog. Phys*. 2015. V. 78. P. 104501.

3.6 Yang G., Ciccarelli Ch., Robinson W. A. Boosting spintronics with superconductivity. *APL Mater*. 2021. V. 9. P. 050703.

3.7 Golovchanskiy I. A., Abramov N. N., Stolyarov V. S., Bolginov V. V., Ryazanov V. V., Golubov A. A., Ustinov A. U. Ferromagnet / Supercon-

ductor Hybridization for Magnonic Applications. *Adv. Funct. Mater.* 2018. V. 28. P. 1802375.

3.8 Alicea J. New directions in the pursuit of Majorana fermions in solid state systems. *Rep. Prog. Phys.* 2012. V. 75. P. 076501.

3.9 Beenakker C. W. J. Search for Majorana Fermions in Superconductors. *Annu. Rev. Condens. Matter Phys.* 2013. V. 4. P. 113–136.

3.10 Sato M., Ando Y. Topological superconductors: a review. *Rep. Prog. Phys.* 2017. V. 80. P. 076501.

3.11 Balatsky A. V., Vekhter I., Zhu J.-X. Impurity-induced states in conventional and unconventional superconductors. *Rev. Mod. Phys.* 2006. V. 78. P. 373–433.

3.12 Kitaev A. Fault-tolerant quantum computation by anyons. *Ann. Phys.* 2003. V. 303. P. 2–30.

3.13 Freedman M. H., Kitaev A., Larsen M. J., Wang Z. Topological quantum computation. *Bull. Am. Math. Soc.* 2003. V. 40. P. 31–38.

3.14 Knapp C., Zaletel M., Liu D. E., Cheng M., Bonderson P., Nayak C. The nature and correction of diabatic errors in anyon braiding. *Phys. Rev. X.* 2016. V. 6. P. 041003.

3.15 Nayak C., Simon S. H., Stern A., Freedman M., Das Sarma S. Non-Abelian anyons and topological quantum computation. *Rev. Mod. Phys.* 2008. V. 80. P. 1083–1159.

3.16 Plugge S., Rasmussen A., Egger R., Flensberg K. Majorana box qubits. *New J. Phys.* 2017. V. 19. P. 012001.

3.17 Choy T.-P., Edge J. M., Akhmerov A. R., Beenakker C. W. J. Majorana fermions emerging from magnetic nanoparticles on a superconductor without spin-orbit coupling. *Phys. Rev. B.* 2011. V. 84. P. 195442.

3.18 Chung S. B., Zhang H.-J., Qi X.-L., Zhang S.-Ch. Topological superconducting phase and Majorana fermions in half-metal / superconductor heterostructures. *Phys. Rev. B.* 2011. V. 84. P. 060510(R).

3.19 Nadj-Perge S., Drozdov I. K., Bernevig B. A., Yazdani A. Proposal for realizing Majorana fermions in chains of magnetic atoms on a superconductor. *Phys. Rev. B.* 2013. V. 88. P. 020407(R).

3.20 Gorczyca-Goraj A., Domański T., Maśka M. M. Topological superconductivity at finite temperatures in proximitized magnetic nanowires. *Phys. Rev. B.* 2019. V. 99. P. 235430.

3.21 Crawford D., Mascot E., Morr D. K., Rachel S. High-temperature Majorana fermions in magnet-superconductor hybrid systems. *Phys. Rev. B*. 2020. V. 101. P. 174510.

3.22 Kasai M., Ohno T., Kanke Y, Kozono Y., Hanazono M., and Sugita Y. Current-Voltage Characteristics of $YBa_2Cu_3O_y$ $La_{0.7}Ca_{0.3}MnO_z/YBa_2Cu_3O_y$ trailered-type junctions. *Jpn. J. Appl. Phys*. 1990. V. 29. P. L2219–L2222.

3.23 Kasai M., Kanke Y., Ohno T., Kozono Y. Possible mechanism of proximity effect coupled to spin fluctuation in $YBa_2Cu_3O_y$/magnetic manganese oxide/$YBa_2Cu_3O_y$ junctions. *J. Appl. Phys*. 1992. V. 72. P. 5344–5349.

3.24 Kalcheim Y., Kirzhner T., Koren G., Millo O. Long-range proximity effect in $La_{2/3}Ca_{1/3}MnO_3/(100)YBa_2Cu_3O_{7-\delta}$ ferromagnet / superconductor bilayers: Evidence for induced triplet superconductivity in the ferromagnet. *Phys. Rev. B*. 2011. V. 83. P. 064510.

3.25 Visani C., Sefrioui Z., Tornos J., Leon C., Briatico J., Bibes M., Barthélémy A., Santamaría J., Villegas J. E. Equal-spin Andreev reflection and long-range coherent transport in high-temperature superconductor / half-metallic ferromagnet junctions. *Nat. Phys*. 2012. V. 8. P. 539–543.

3.26 Eschrig M., Löfwander T. Triplet supercurrents in clean and disordered half-metallic ferromagnets. *Nat. Phys*. 2008. V. 4. P. 138–143.

3.27 D'yachenko A. I., Krivoruchko V. N., Tarenkov V. Yu. Andreev spectroscopy of point contacts between a low-temperature superconductor and manganite. *Fiz. Nizk. Temp*. 2006. V. 32. P. 1085–1095. [*Low Temp. Phys*. 2006. V. 32. P. 824–831].

3.28 Krivoruchko V. N., Tarenkov V. Yu. Local triplet superconductivity of $La_{0.65}Ca_{0.35}MnO_3$-X point contacts (X = Pb, MgB_2). *Phys. Rev. B*. 2007. V. 75. P. 214508.

3.29 Krivoruchko V. N., Tarenkov V. Yu. Anomalous superconductivity of $Pb/La_{0.7}Sr_{0.3}MnO_3$ point contacts. *Phys. Rev. B*. 2008. V. 78. P. 054522.

3.30 Krivoruchko V. N., Tarenkov V. Yu. Triple-gap superconductivity of MgB_2-(La,Sr)MnO_3 composite. *Phys. Rev. B*. 2012. V. 86. P. 104502.

3.31 Krivoruchko V. N., D'yachenko A. I., Tarenkov V. Yu. Andreev-spectroscopy study of unconventional superconductivity in MgB_2:(La,Sr)MnO_3

nanocomposite. *Fiz. Nizk. Temp.* 2014. V. 40. P. 1147–1154. [*Low Temp. Phys.* 2014. V. 40. P. 895–901].

3.32 Krivoruchko V. N., Dyachenko A. I., Tarenkov V. Y. Point-contact Andreev-reflection spectroscopy of doped manganites: Charge carrier spin-polarization and proximity effects (Review Article). *Fiz. Nizk. Temp.* 2013. V. 39. P. 276–292. [*Low Temp. Phys.* 2013. V. 39. P. 211–224].

3.33 D'yachenko A. I., Tarenkov V. Yu., Krivoruchko V. N. The Berezin-skii–Kosterlitz–Thouless transition in bulk MgB_2:(La,Sr)MnO_3 super-conductor-ferromagnetic nanocomposites. *Fiz. Nizk. Temp.* 2019. V. 45. 1360–1365. [*Low. Temp. Phys.* 2019. V. 45. 1156–1160].

3.34 Krivoruchko V. N., Tarenkov V. Yu. Percolation transitions in d-wave superconductor-half-metallic ferromagnet nanocomposites. *Fiz. Nizk. Temp.* 2019. V. 45. P. 555–561. [*Low. Temp. Phys.* 2019. V. 45. P. 476–481].

3.35 D'yachenko A. I., Krivoruchko V. N., Tarenkov V. Yu. Two-dimensional Berezinskii–Kosterlitz–Thouless topological phase transition in three-dimensional $Bi_2Sr_2Ca_2Cu_3O_{6+x}$:(La,Sr)MnO_3 nanocomposites. *Fiz. Nizk. Temp.* 2021. V. 47. P. 501–508. [*Low Temp. Phys*. 2021. V. 47. P. 466–472].

3.36 Krivoruchko V. N. Local spin-triplet superconductivity in half-metallic manganites: A perspective platform for high-temperature topological superconductivity. *Fiz. Nizk. Temp*. 2021. V. 47. P. 891–988. [*Low Temp. Phys*. 2021. V. 47. P. 901–907].

3.37 Giroud M., Courtois H., Hasselbach K., Mailly D., Pannetier B. Super-conducting proximity effect in a mesoscopic ferromagnetic wire. *Phys. Rev. B.* 1998. V. 58. P. R11872–R11875.

3.38 Petrashov V. T., Sosnin I. A., Cox I., Parsons A., Troadec C. Giant Mutual Proximity Effects in Ferromagnetic / Superconducting Nano-structures. *Phys. Rev. Lett.* 1999. V. 83. P. 3281–3284.

3.39 Lawrence M. D., Giordano N. Proximity effects in superconductor-ferromagnet junctions. *J. Phys.: Condens. Matter*. 1999. V. 11. P. 1089–1084.

3.40 Kalcheim Y., Millo O., Egilmez M., Robinson J. W. A., Blamire M. G. Evidence for anisotropic triplet superconductor order parameter in half-metallic ferromagnetic $La_{0.7}Ca_{0.3}Mn_3O$ proximity coupled to superconducting $Pr_{1.85}Ce_{0.15}CuO_4$. *Phys. Rev. B.* 2012. V. 85. P. 104504.

3.41 Keizer R. S., Goennenwein S. T. B., Klapwijk T. M., Maio G., Xiao G., Gupta A. A spin triplet supercurrent through the half-metallic ferromagnet CrO_2. *Nature (London).* 2006. V. 439. P. 825–827.

3.42 Sosnin I., Cho H., Petrashov V., Volkov A. F. Superconducting Phase Coherent Electron Transport in Proximity Conical Ferromagnets. *Phys. Rev. Lett.* 2006. V. 96. P. 157002.

3.43 Buzdin A. I. Proximity effects in superconductor-ferromagnet heterostructures. *Rev. Mod. Phys.* 2005. V. 77. P. 935–976.

3.44 Kadigrobov A., Skekhter R. I., Jonson M. Quantum spin fluctuations as a source of long-range proximity effects in diffusive ferromagnet-super conductor structures. *Europhys. Lett.* 2001. V. 54. P. 394–400.

3.45 Bergeret F. S., Volkov A. F., Efetov K. B. Odd triplet superconductivity and related phenomena in superconductor-ferromagnet structures. *Rev. Mod. Phys*. 2005. V. 77. P. 1321–1373.

3.46 Deutscher G. Percolation and Superconductivity pp. 95–113. In book: Percolation, Localization and Superconductivity. Ed. Goldman A. B., Wolf S. A. Plenum: New York. 1984.

3.47 Skvortsov M. A., Larkin A. I., Feigel'man M. V. Proximity Action theory of superconductive nanostructures. *Usp. Fiz. Nauk* (Suppl.). 2001. V. 171. P. 76–80.

3.48 Sternfeld I., Shelukhin V., Tsukernik A., Karpovski M., Gerber A., Palevski A. Proximity effect in granular superconductor–normal metal structures. *Phys. Rev. B*. 2005. V. 71. P. 064515.

3.49 Andreev A. F. The Thermal conductivity of the intermediate state in superconductors. *Sov. Phys. JETP.* 1964. V. 19. P. 1228–1231.

3.50 Tokuyasu T., Sauls J. A., Rainer D. Proximity effect of a ferromagnetic insulator in contact with a superconductor. *Phys. Rev. B.* 1988. V. 38. P. 8823–8833.

3.51 Eschrig M. Spin-polarized supercurrents for spintronics. *Phys. Today*. 2011. V. 64. P. 43–49.

3.52 Dagotto E., Hotta T., Moreo A. Colossal magnetoresistant materials: the key role of phase separation. *Phys. Rep.* 2001. V. 344. P. 1–153.

3.53 Ziese M. Extrinsic magnetotransport phenomena in ferromagnetic oxides. *Rep. Prog. Phys.* 2002. V. 65. P. 143–249.

3.54 Krivoruchko V. N. The Griffiths phase and the metal-insulator transition in substituted manganites (Review Article). *Fiz. Nizk. Temp.* 2014. V. 40. P. 756–774. [Low Temp. Phys. 2014. V. 40. P. 586–599].

3.55 Zener C. Interaction between the d-shells in the transition metals. II. Ferromagnetic compounds of manganese with perovskite structure. *Phys. Rev.* 1951. V. 82. P. 403–405.

3.56 de Groot R. A., Mueller F. M., van Engen P. G., Buschow K. H. J. New class of materials: half-metallic ferromagnets. *Phys. Rev. Lett.* 1983. V. 50. P. 2024–2027.

3.57 Bowen M., Bibes M., Barthélémy A., Contour J.-P., Anane A., Lemaître Y., Fert A. Nearly total spin polarization in $La_{2/3}Sr_{1/3}MnO_3$ from tunneling experiments. *Appl. Phys. Lett.* 2003. V. 82. P. 233–235.

3.58 Savosta M. M., Krivoruchko V. N., Danilenko I. A., Tarenkov V. Yu., Konstantinova T. E., Borodin A. V., Varyukhin V. N. Nuclear spin dynamics and magnetic structure of nanosized particles of $La_{0.7}Sr_{0.3}MnO_3$. *Phys. Rev. B.* 2004. V. 69. P. 024413.

3.59 Krivoruchko V., Konstantinova T., Mazur A., Prokhorov A., Varyukhin V. Magnetic resonances spectroscopy of nanosize particles $La_{0.7}Sr_{0.3}MnO_3$. *J. Magn. Magn. Mater.* 2006. V. 300. P. e122–e125.

3.60 Ulyanov A. N., Yang D. S., Mazur A. S., Krivoruchko V. N., Levchenko G. G., Danilenko I. A., Konstantinova T. E. Local structure and magnetic inhomogeneity of nano-sized $La_{0.7}Sr_{0.3}MnO_3$ manganites. *J. Appl. Phys.* 2011. V. 109. P. 123928.

3.61 Liu X., Panguluri R. P., Huang Z.-F., Nadgorny B. Double percolation transition in superconductor-ferromagnet nanocomposites. *Phys. Rev. Lett.* 2010. V. 104. P. 035701.

3.62 Acharya S., Biswal A. K., Ray J., Vishwakarma P. N. Study of $Bi_2Sr_2CaCu_2O_8$/ $BiFeO_3$ nano-composite for electrical transport applications. *J. Appl. Phys.* 2012. V. 112. P. 053916.

3.63 Strelniker Y. M., Frydman A., Havlin S. Percolation model for the superconductor-insulator transition in granular films. *Phys. Rev. B.* 2007. V. 76. P. 224528.

3.64 Sternfeld I., Shelukhin V., Tsukernik A., Karpovski M., Gerber A., Palevski A. Proximity effect in granular superconductor–normal metal structures. *Phys. Rev. B.* 2005. V. 71. P. 064515.

3.65 Ruiz-Valdepeñas L., Vélez M., Valdés-Bango F., Álvarez-Prado L. M., Martín J. I., Navarro E., Alameda J. M., Vicent J. L. Double percolation effects and fractal behavior in magnetic / superconducting hybrids. *New J. Phys.* 2013. V. 15. P. 103025.

3.66 Berezinsky V. L. Destruction of long-range order in one-dimensional and two-dimensional systems having a continuous symmetry group. I. Classical systems. *JETP.* 1971. V. 59. P. 907–920. [*Sov. Phys. JETP.* 1971. V. 32. P. 493–500].

3.67 Kosterlitz J. M., Thouless D. J. Ordering, metastability and phase transitions in two-dimensional systems. *J. Phys. C.* 1973. V. 6. P. 1181–1203.

3.68 Kosterlitz J. M. The critical properties of the two-dimensional xy model. *J. Phys. C.* V. 7. P. 1046–1060.

3.69 Blatter G., Feigel'man M. V., Geshkenbein V. B., Larkin A. I., Vinokur V. M. Vortices in high-temperature superconductors. *Rev. Mod. Phys.* 1994. V. 66. P. 1125–1388.

3.70 Goldman A. M. The Berezinskii–Kosterlitz–Thouless transition in superconductors. in 40 Years of Berezinskii–Koste–Rlitz–Thouless Theory. Ed. José J. V. World Scientific: Singapore. 2013.

3.71 Costa B. V., Lima A. B. Dynamical behavior of vortices in thin film magnetic systems. *J. Magn. Magn. Mater.* 2012. V. 324. P. 1999–2005.

3.72 Tutsch U., Wolf B., Wessel S., Postulka L., Tsui Y., Jeschke H. O., Opahle I., Saha-Dasgupta T., Valentí R., Brühl A., Remović-Langer K., Kretz T., Lerner H.-W., Wagner M., Lang M. Evidence of a field-induced Berezinskii–Kosterlitz–Thouless scenario in a two-dimensional spin–dimer system. *Nat. Commun.* 2014. V. 5. P. 5169.

3.73 Minnhagen P. The two-dimensional Coulomb gas, vortex unbinding, and superfluid-superconducting films. *Rev. Mod. Phys.* 1987. V. 59. P. 1001–1066.

3.74 Ashoka A., Bhagyashree K. S., Bhat S. V. Signatures of field-induced Berezinskii–Kosterlitz–Thouless correlations in the three-dimensional manganite $Bi_{0.5}Sr_{0.5}Mn_{0.9}Cr_{0.1}O_3$. *Phys. Rev. B.* 2020. V. 102. P. 024429.

3.75 Benfatto L., Castellani C., Giamarchi T. Doping dependence of the vortex-core energy in bilayer films of cuprates. *Phys. Rev. B.* 2008. V. 77. P. 100506(R).

3.76 Benfatto L., Castellani C., Giamarchi T. Broadening of the Berezinskii–Kosterlitz–Thouless superconducting transition by inhomogeneity and finite-size effects. *Phys. Rev. B.* 2009. V. 80. P. 214506.

3.77 Gantmakher V. F. Localized superconducting pairs. *Fiz. Nizk. Temp.* 2011. V. 37. P. 71–83. [*Low Temp. Phys.* 2011. V. 37. P. 59–68].

3.78 Resnick D. J., Garland J. C., Boyd J. T., Shoemaker S., Newrock R. S. Kosterlitz-Thouless transition in proximity-coupled superconducting arrays. *Phys. Rev. Lett.* 1981. V. 47. 1542–1545.

3.79 Halperin B. I., Nelson D. R. Resistive transition in superconducting films. *J. Low Temp. Phys*. 1979. V. 36. P. 599–616.

3.80 Doniach S., Huberman B. A. Topological Excitations in Two-dimensional superconductors. *Phys. Rev. Lett.* 1979. V. 42. P. 1169–1172.

3.81 Bergeret F. S., Virtanen P., Ozaeta A., Heikkilä T. T., Cuevas J. C. Supercurrent and Andreev bound state dynamics in superconducting quantum point contacts under microwave irradiation. *Phys. Rev. B.* 2011. V. 84. P. 054504.

3.82 Semenov A. V., Devyatov I. A., de Visser P. J., Klapwijk T. M. Coherent excited states in superconductors due to a microwave field. *Phys. Rev. Lett*. 2016. V. 117. P. 047002.

3.83 Kirkpartrick S. Percolation and conduction. *Rev. Mod. Phys.* 1973. V. 45. P. 574–588.

3.84 Bunde A., Dieterich W. Percolation in composites. *J. Electroceram.* 2000. V. 5. P. 81–92.

3.85 Balberg I. Tunnelling and percolation in lattices and the continuum. *J. Phys. D: Appl. Phys.* 2009. V. 42. P. 064003.

3.86 Niu Z. P., Xing D. Y. Spin-triplet pairing states in ferromagnet / ferromagnet / d-Wave superconductor heterojunctions with noncollinear magnetizations. *Phys. Rev. Lett.* 2007. V. 98. P. 057005.

3.87 Hu T., Xiao H., Visani C., Sefrioui Z., Santamaria J., Almasan C. C. Evidence from magnetoresistance measurements for an induced triplet superconducting state in $La_{0.7}Ca_{0.3}MnO_3/YBa_2Cu_3O_{7-\delta}$ multilayers. *Phys. Rev. B*. 2009. V. 80. P. 060506(R).

3.88 Dybko K., Werner-Malento K., Aleshkevych P., Wojcik M., Sawicki M., Przyslupski P. Possible spin-triplet superconducting phase in the $La_{0.7}Sr_{0.3}MnO_3/YBa_2Cu_3O_7/La_{0.7}Sr_{0.3}MnO_3$ trilayer. *Phys. Rev. B*. 2009. V. 80. P. 144504.

3.89 Kalcheim Yo., Kirzhner T., Koren G., Millo O. Long-range proximity effect in $La_{2/3}Ca_{1/3}MnO_3/(100)YBa_2Cu_3O_{7-\delta}$ ferromagnet / superconductor bilayers: Evidence for induced triplet superconductivity in the ferromagnet. *Phys. Rev. B*. 2011. V. 83. P. 064510.

3.90 Wang W., Shao D. F., Xiao R. C., Lu W. J., Wu H. Y. Long-range spin-triplet superconductivity induced by magnetic field in d wave superconductor / ferromagnet hybrid system. *J. Supercond. Nov. Magn*. 2016. V. 29. P. 1741–1746.

3.91 Loktev V. M., Quick R. M., Sharapov S. G. Phase fluctuations and pseudogap phenomena. *Phys. Rep.* 2001. V. 349. P. 1–123.

3.92 Emery J. V., Kivelson S. A. Superconductivity in bad metals. *Phys. Rev. Lett.* 1995. V. 74. P. 3253–3256.

3.93 Berg E., Orgad D., Kivelson S. A. Route to high-temperature superconductivity in composite systems. *Phys. Rev. B*. 2008. V. 78. P. 094509.

3.94 Mondal M., Kamlapure A., Chand M., Saraswat G., Kumar S., Jesudasan J., Benfatto L., Tripathi V., Raychaudhuri P. Phase fluctuations in a strongly disordered s-wave NbN superconductor close to the metal-insulator transition. *Phys. Rev. Lett*. 2011. V. 106. P. 047001.

3.95 Sacépé B., Dubouchet T., Chapelier C., Sanquer M., Ovadia M., Shahar D., Feigel'man M., Ioffe L. Localization of preformed Cooper pairs in disordered superconductors. *Nature Phys*. 2011. V. 7. P. 239–244.

3.96 Blonder G. E., Tinkham M., Klapwijk T. M. Transition from metallic to tunneling regimes in superconducting microconstrictions: Excess current, charge imbalance, and supercurrent conversion. *Phys. Rev. B*. 1982. V. 25. P. 4515–4532.

3.97 Daghero D., Gonnelli R. S. Probing multiband superconductivity by point-contact spectroscopy. *Supercond. Sci. Technol.* 2010. V. 23. P. 043001.

3.98 Naidyuk Yu. G., Yanson I. K. Point-contact spectroscopy. Springer. 2005.

3.99 Pickett W. E., Singh D. J. Electronic structure and half-metallic transport in the $La_{1-x}Ca_xMnO_3$ system. *Phys. Rev. B.* 1996. V. 53. P. 1146–1160.

3.100 Wei J. Y. T., Yeh N.-C., Vasquez R. P. Tunneling evidence of half-metallic ferromagnetism in $La_{0.7}Ca_{0.3}MnO_3$. *Phys. Rev. Lett.* 1997. V. 79. P. 5150–5153.

3.101 Jo M.-H., Mathur N. D., Todd N. K., Blamire M. G. Very large magneto-resistance and coherent switching in half-metallic manganite tunnel junctions. *Phys. Rev. B.* 2000. V. 61. P. R14905–R15908.

3.102 D'yachenko A. I., D'yachenko V. A., Tarenkov V. Yu., Krivoruch-ko V. N. Spin polarization of charge carriers and Andreev reflection in (LaCa)MnO / superconductor point contacts. *Fiz. Tverd. Tela.* 2006. V. 48. P. 407–414. [*Phys. Solid State.* 2006. V. 48. P. 432–440].

3.103 Dynes R. C., Narayanamurti V., Garno J. P. Direct Measurement of quasiparticle-lifetime broadening in a strong-coupled superconductor. *Phys. Rev. Lett.* 1978. V. 41. P. 1509–1512.

3.104 Xi X. X. Two-band superconductor magnesium diboride. *Rep. Prog. Phys.* 2008. V. 71. P. 116501.

3.105 Mitra J., Raychaudhuri A. K., Mukovskii Ya. M., Shulyatev D., Toku-ra Y., Hamada N. Depletion of the density of states at the Fermi level in metallic colossal magnetoresistive manganites. *Phys. Rev. B.* 2003. V. 68. P. 134428.

3.106 Saitoh T., Dessau D. S., Moritomo Y., Kimura T., Tokura Y., Hama-da N. Temperature-dependent pseudogaps in colossal magnetoresistive oxides. *Phys. Rev. B.* 2000. V. 62. P. 1039–1043.

3.107 Tarenkov V. Yu., D'yachenko A. I., Krivoruchko V. N. Pressure-induced variation of the magnetic structure of the surface of $La_{0.6}Sr_{0.4}MnO_3$ granules. *Zh. Éksp. Teor. Fiz.* 2001. V. 120. P. 205–213. [*JETP.* 2001. V. 93. P. 180–187].

3.108 Edwards M. Ferromagnetism and electron-phonon coupling in the manganites. *Adv. Phys.* 2002. V. 51. P. 1259–1318.

3.109 Iguchi I., Yamaguchi T., Sugimoto A. Diamagnetic activity above Tc as a precursor to superconductivity in $La_{2-x}Sr_xCuO_4$ thin films. *Nature*. 2001. V. 412. P. 420–423.

3.110 González J. L., de Mello E. V. L. Theory of the diamagnetism above the critical temperature for cuprates. *Phys. Rev. B*. 2004. V. 69. P. 134510.

3.111 Eschrig M., Kopu J., Cuevas J. C., Schön G. Theory of half-metal / superconductor heterostructures. *Phys. Rev. Lett*. 2003. V. 90. P. 137003.

3.112 Bulaevskii L., Eneias R., Ferraz A. Triplet superconductivity in ferromagnets due to magnon exchange. *Phys. Rev. B*. 2019. V. 99. P. 064506.

3.113 Saitoh T., Dessau D. S., Moritomo Y., Kimura T. Temperature-dependent pseudogaps in colossal magnetoresistive oxides. *Phys. Rev. B*. 2000. V. 62. P. 1039.

3.114 Sau J. D., Tewari S., Lutchyn R. M., Stanescu T. D., das Sarma S. Non-Abelian quantum order in spin-orbit-coupled semiconductors: Search for topological Majorana particles in solid-state systems. *Phys. Rev. B*. 2010. V. 82. P. 214509.

3.115 Wimmer M., Akhmerov A. R., Dahlhaus J. P., Beenakker C. W. J. Quantum point contact as a probe of a topological superconductor. *New J. Phys*. 2011. V. 13. P. 053016.

3.116 Nakosai S., Tanaka Y., Nagaosa N. Two-dimensional p-wave superconducting states with magnetic moments on a conventional s-wave superconductor. *Phys. Rev. B*. 2013. V. 88. P. 180503(R).

3.117 Mourik V., Zuo K., Frolov S. M., Plissard S. R., Bakkers E. P. A. M., Kouwenhoven L. P. Signatures of Majorana fermions in hybrid superconductor-semiconductor nanowire devices. *Science*. 2012. V. 336. P. 1003–1007.

3.118 Das A., Ronen Y., Most Y., Oreg Y., Heiblum M., Shtrikman H. Zero-bias peaks and splitting in an Al–InAs nanowire topological superconductor as a signature of Majorana fermions. *Nat. Phys*. 2012. V. 8. P. 887–895.

3.119 Deng M. T., Yu C. L., Huang G. Y., Larsson M., Caroff P., Xu H. Q. Zero-bias peaks and splitting in an Al–InAs nanowire topological superconductor as a signature of Majorana fermions. *Nano Lett*. 2012. V. 12. P. 6414–6419.

3.120 Liu J., Potter A. C., Law K. T., Lee P. A. Zero-bias peaks in the tunneling conductance of spin-orbit-coupled superconducting wires with and without Majorana end-states. *Phys. Rev. Lett.* 2012. V. 109. P. 267002.

3.121 Pikulin D. I., Dahlhaus J. P., Wimmer M., Schomerus H., Beenakker C. W. J. A zero-voltage conductance peak from weak antilocalization in a Majorana nanowire. *New J. Phys.* 2012. V. 14. P. 125011.

3.122 Bagrets D., Altland A. Class D Spectral Peak in Majorana Quantum Wires. *Phys. Rev. Lett.* 2012. V. 109. P. 227005.

3.123 Liu C.-X., Sau J. D., Stanescu T. D., das Sarma S. Andreev bound states versus Majorana bound states in quantum dot-nanowire-superconductor hybrid structures: Trivial versus topological zero-bias conductance peaks. *Phys. Rev. B.* 2017. V. 96. P. 075161.

3.124 Kitaev A. Yu. Unpaired Majorana fermions in quantum wires. *Phys.-Usp.* 2001. V. 44. P. 131–136.

4. REENTRANT INDUCED SUPERCONDUCTIVITY IN HYBRID STRUCTURE WITH HIGH BARRIER TRANSPARENCY

E. Zubov[1, 2]

Abstract

Within the framework of the self-consistent effective field approximation of the time dependent perturbation theory, an influence of the electron tunneling on spontaneously induced order parameters in a hybrid structure «normal metal-superconductor» is considered. For a normal-metal model that does not take into account electron-electron scattering as well as electron-phonon coupling, it has been obtained a critical barrier transparency corresponding to the disappearance of superconductivity in the ground state. The presence of incoherent excitations leads to a complex relationship between the effects of ordering, thermal fluctuations, and tunneling. Near the critical barrier transparency, this can stabilize a superconducting state in the certain temperature regions. As a result, a reentrant superconductivity phenomenon is observed. The studied spectral properties of the hybrid structure reflect existence of both coherent and incoherent elementary excitations.

✉ Eduard Zubov
eezubov@ukr.net

[1] Kyiv Academic University, Vernadsky blvd. 36, 03142 Kyiv, Ukraine
[2] Vasyl' Stus Donetsk National University, 600-richchia vul. 21, 21021 Vinnytsia, Ukraine

4.1 Introduction

Despite a long history of the transport properties studies of the «normal metal-superconductor» hybrid structures, the problem of a rigorous quantum-mechanical consideration of proximity effect in such systems has not yet lost its relevance. This is especially evident in recent years in connection with the search and realization of Majorana fermions based on the proximity effect in the system of a superconductor with an s-symmetry gap and topological insulator with surface states [4.1]. This type of fermions is protected from decoherence and is of promising importance in the formation of qubit states for quantum computers. The problem of superconductivity as a quantum effect is rather complicated from the point of view of subsequent accounting for the correlation effects and influence of barriers in inhomogeneous structures. To date, to analyze a huge array of experimental data on electron tunneling, a wide range of theoretical methods for studying the observed phenomena in hybrid structures have been developed, which are based on the well-known equations of Gor'kov [4.2], Bogolyubov, P. de Gennes [4.3], McMillan [4.4] and their semiclassical approximations [4.5, 4.6]. It should be noted that in the study of critical temperatures, spectral and transport properties of hybrid structures consisting of a superconductor and normal magnetic or nonmagnetic metals, as a rule, a linear integral relationship is used for the coordinate dependence of the gap function using a nonlocal kernel [4.7–4.9]. However, in the case of sufficiently transparent barriers, when a perturbation in the form of tunnel Hamiltonian is significant, it is no longer possible to consider a linear approximation, since the contribution of electron correlations and scattering may turn out to be significant. In particular, the appearance of reentrant super-conductivity, found in the $Nb/Cu_{1-x}Ni_x$ bilayers [4.10], can be associated not only with the ferromagnetism of a normal metal but also with the effect of electron tunneling through a transparent barrier.

Earlier, we presented an effective field approximation in the framework of the diagrammatic method of perturbation theory for solving a wide range of problems in condensed matter physics [4.11]. In particular, in the zeroth approximation over an inverse effective radius of electron interactions, it is possible to build a quantum nonlinear theory of the proximity effect in a hybrid structure "normal metal-superconductor" with a tunnel barrier [4.12], in which

there are no the phenomenological parameters. Since electron-electron scattering is not taken into account in the Hamiltonian, this model corresponds to ballistic limit, when a mean free path is substantially greater than the film thickness. Such parameters of superconductivity as the coherence length or the penetration depth of superconducting correlations into a normal metal are derivatives of the theory and can be expressed in terms of the introduced microscopic parameters of the Hamiltonian and temperature.

The structure of the chapter is as follows. In Section 4.2, the tunneling Hamiltonian of the hybrid structure «normal metal-superconductor» (FMM-SC) with the main microscopic parameters of interactions is presented. The presence of ferromagnetism (FM) in the normal metal (N-metal) is also assumed. Further, the main goal of this work is to study the proximity effect for given model Hamiltonian, which is expressed in the site representation. It is possible if the Bloch electronic functions are replaced by localized Wannier functions for matrix elements. Thus, the unperturbed Hamiltonian with the energy of chemical potential allows us to easily average the arising correlators in any order of the time perturbation theory, and also to use graphical methods for summing diagrams in a wave space to determine the effective propagator lines. Section 4.3 gives a detailed calculation of the contributions to Green's functions taking into account the adiabatic switching on the interactions caused by the tunneling Hamiltonian, as well as the appearance of imaginary parts responsible for electron scattering, magnitude, and phase of the spontaneous order parameter. The results of numerical calculations of phase diagrams for the inverse proximity effect and spectral characteristics of SC are presented. In Section 4.4, it is studied an influence the tunnel SC electrons on order parameter, excitation spectrum, and spectral density of the FMM part in the hybrid structure. In Section 4.5, the main conclusions of the article are formulated.

4.2 Hamiltonian of the «normal metal-superconductor» electron system and the self- consistent order parameter

In a general case, the Hamiltonian for considered hybrid structure can be written as the sum of Hamiltonians $\hat{H}_N$, $\hat{H}_S$ for N-metal and SC, respectively, as well as the tunnel contribution $\hat{H}_T$:

$$\hat{H} = \hat{H}_N + \hat{H}_S + \hat{H}_T, \qquad (4.1)$$

where for a N-metal in the site representation for the second quantized electron creation (annihilation) operators $c_{\sigma i}^+ (c_{\sigma i})$ with a spin σ

$$\hat{H}_N = \sum_{i,j,\sigma} t_{1ij} c_{\sigma i}^+ c_{\sigma j} - \sum_{i\sigma} \mu_\sigma c_{\sigma i}^+ c_{\sigma i}. \qquad (4.2)$$

Here, t_{1ij} is the hopping integral, which determines the electron band energy, $\mu_\sigma = \mu_1 + \sigma J_0$, μ_1 is the chemical potential for N-metal, J_0 is the parameter of electron exchange interactions and $J_0 > 0$ for a ferromagnet. Also, $\sigma = \pm 1$ for saturated state and $\sigma = \pm 2 < \sigma_z >$ for magnet with a mean spin $< \sigma_z >$. For the superconducting part of this structure, we write in a general case the interaction Hamiltonian

$$\hat{H}_S = \sum_{i,j,\sigma} t_{2ij} a_{\sigma i}^+ a_{\sigma j} + \sum_{ij} \left(\sum_{\sigma\sigma'} V_{ij,ji}^C n_{i\sigma} n_{j\sigma'} - \sum_q \frac{\left|M_q\right|^2}{\omega_q} e^{iq(R_i - R_j)} n_i n_j \right) - \mu_2 \sum_{i\sigma} a_{\sigma i}^+ a_{\sigma i}, \qquad (4.3)$$

where μ_2, t_{2ij} and $V_{ij,ji}^C$ are the SC chemical potential, electron band energy and energy of the Coulomb electron repulsion in the sites with occupancies $n_{i\sigma}$ and $n_{i\sigma'}$, $n_i = n_{i\sigma} + n_{i-\sigma}$, respectively. $\left|M_q\right|^2 / \omega_q$ is the constant of electron-phonon interaction [4.13] with phonon frequency ω_q and matrix element M_q. It is known that near the Fermi level with a width of the order of the Debye energy, the attraction of electrons prevails over their Coulomb repulsion [4.14]. Therefore, the second term in (4.3) can be written in the form:

$$\hat{H}_{El,-ph} = -\sum_{ij\sigma\sigma'} V_{ij}^{el.-ph} n_{i\sigma} n_{j\sigma'} \qquad (4.4)$$

Spontaneous breaking of the Hamiltonian (4.4) symmetry is possible only in a fixed narrow energy area. Let us extract from (4.4) the order parameters corresponding to the superconducting phase in the form of anomalous correlators $< a_{i\sigma}^+ a_{j\sigma'}^+ >$ and $< a_{j\sigma'} a_{i\sigma} >$, where the symbol $<...>$ denotes the statistical averaging over the total Hamiltonian (4.1). For this, we write (4.4) as follows:

$$\hat{H}_{El.-ph} = -\sum_{ij\sigma\sigma'} V_{ij}^{el.-ph} a_{i\sigma}^+ a_{i\sigma} a_{j\sigma'}^+ a_{j\sigma'} = -\sum_{ij\sigma\sigma'} V_{ij}^{el.-ph} a_{i\sigma}^+ a_{j\sigma'}^+ a_{j\sigma'} a_{i\sigma} =$$
$$-\sum_{ij\sigma\sigma'} V_{ij}^{el.-ph} \left(\{ a_{i\sigma}^+ a_{j\sigma'}^+ - <a_{i\sigma}^+ a_{j\sigma'}^+> \} + <a_{i\sigma}^+ a_{j\sigma'}^+> \right) \left(\{ a_{j\sigma'} a_{i\sigma} - <a_{j\sigma'} a_{i\sigma}> \} + <a_{j\sigma'} a_{i\sigma}> \right). \tag{4.5}$$

The product of the terms in curly brackets describes the fluctuation effects of superconductivity, which are not considered here. Leaving only the operator terms in (4.5), we obtain the Hamiltonian in the molecular field approximation

$$\hat{H}_{El,-ph}^{MF} = -\sum_{ij\sigma} V_{ij}^{el.-ph} \left(a_{i\sigma}^+ a_{j-\sigma}^+ <a_{j-\sigma} a_{i\sigma}> + a_{j-\sigma} a_{i\sigma} <a_{i\sigma}^+ a_{j-\sigma}^+> \right), \tag{4.6}$$

where $\sigma' = -\sigma$ for singlet Cooper pairing (s-superconductivity). Let us enter a gap function

$$\Delta_{ij\sigma} = V_{ij}^{el.-ph} <a_{j-\sigma} a_{i\sigma}>. \tag{4.7}$$

Then the Hamiltonian (4.7) takes the form:

$$\hat{H}_{El,-ph}^{MF} = -\sum_{ij\sigma} \left(\Delta_{ij\sigma} a_{i\sigma}^+ a_{j-\sigma}^+ + \Delta_{ij\sigma}^* a_{j-\sigma} a_{i\sigma} \right). \tag{4.8}$$

Now let us consider the Fourier transform for gap function (4.7), taking into account that $a_{i\sigma} = \frac{1}{\sqrt{N}} \sum_k e^{ikR_i} a_{k\sigma}$ and $V_{k_1}^{el.-ph}$ is the Fourier transform of the electron-phonon coupling parameter, where N is the number of SC sites. Then we have

$$\Delta_{ij\sigma} = V_{ij}^{el.-ph} <a_{j-\sigma} a_{i\sigma}> =$$
$$= \frac{1}{N^2} \sum_{k_1 q q_1} V_{k_1}^{el.-ph} e^{ik_1(R_i - R_j)} e^{iqR_j} e^{iq_1 R_i} <a_{q-\sigma} a_{q_1\sigma}> \delta_{q_1,-q} = \tag{4.9}$$
$$= \frac{1}{N} \sum_k e^{ik(R_i - R_j)} \sum_q V_{k-q}^{el.-ph} <a_{-q-\sigma} a_{q\sigma}>,$$

where the sum over k_1 is replaced by the sum over $k = k_1 + q$ and the Kronecker symbol determines the gap homogeneity. Thus, from (4.9) we obtain an expression for the Fourier transform of the gap function

$$\Delta_{k\sigma} = \sum_q V_{k-q}^{el.-ph} <a_{-q-\sigma} a_{q\,\sigma}> \tag{4.10}$$

The expression (4.10) defines a self-consistent equation for the gap function, since the abnormal means according to Eq. (4.8) are also expressed in terms of $\Delta_{ij\sigma}$. Standard methods for solving the problem of finding the gap are based on the diagonalization of Hamiltonian (4.8) in a wave space (BCS Hamiltonian) using the Bogolyubov transformation. Unfortunately, such diagonalization does not work for hybrid structures. As a rule, the Gor'kov equations for the coordinate Green's functions are considered, which in the general case are inhomogeneous. It causes considerable difficulties in calculating the nonlinear contributions. In [4.11], we described a method based on averaging over the unperturbed site Hamiltonians

$$\hat{H}_{0N} = -\sum_{i\sigma} \mu_\sigma c_{\sigma i}^+ c_{\sigma i} \,, \qquad (4.11)$$

$$\hat{H}_{0S} = -\mu_2 \sum_{i\sigma} a_{\sigma i}^+ a_{\sigma i} \qquad (4.12)$$

for N-metal and SC, respectively. In this case, the calculation of correlators in a site representation for series of the time perturbation theory with perturbations $V_N = \hat{H}_N - \hat{H}_{0N}$, $V_S = \hat{H}_S - \hat{H}_{0S}$ and $\hat{H}_T$ for FMM, SC and tunnel Hamiltonian $\hat{H}_T$, respectively, do not present any difficulties. Also, $\hat{H}_T$ is written in a site representation as

$$\hat{H}_T = \sum_{il\sigma} \left\{ T_{il} c_{i\sigma}^+ a_{l\sigma} + T_{il}^* a_{l\sigma}^+ c_{i\sigma} \right\}, \qquad (4.13)$$

where T_{il} is an interstitial tunnel matrix element. Thus, it is possible to form infinite series of expansions for the Green's functions using the scattering matrix. After the Fourier transform of both the Matsubara unperturbed Green's functions and interaction parameters, the integration over time and site summation is easily performed. This ultimately gives an infinite series of algebraic expressions for the complete Green's functions easily summed for a certain type of diagrams. In particular, in the zeroth approximation over the inverse effective interaction radius, when loop diagrams are not taken into account, it is easy to summarize diagrams of the same type graphically within the framework of the well-known Dyson equation.

4.3 Equations for Green's functions and order parameters of a superconductor

In accordance with Hamiltonians (4.11)–(4.12), Fourier transforms of the unperturbed Matsubara causal Green's functions for N-metal and a super-conductor have the form:

$$\tilde{G}_{1\sigma}(i\omega_n) = - <T_\tau c_{p\sigma}(\tau)c^+_{p\sigma}(0)>_{0,i\omega_n} = \frac{1}{\beta(i\omega_n + \mu_\sigma)} = -\tilde{G}_{2\sigma}(-i\omega_n)$$

$$G_{1\sigma}(i\omega_n) = - <T_\tau a_{q\sigma}(\tau)a^+_{q\sigma}(0)>_{0,i\omega_n} = \frac{1}{\beta(i\omega_n + \mu_2)} = -G_{2\sigma}(-i\omega_n) \quad , \tag{4.14}$$

where the symbol $<....>_0$ denotes an averaging with Hamiltonians (4.11) or (4.12). The imaginary frequency $i\omega_n = i\pi(2n+1)/\beta$ and $1/\beta = T$ is the temperature.

To find the abnormal correlator $<a_{-q-\sigma}a_{q\sigma}>$, which determines the spontaneous order parameter in an SC, it is necessary to enter the total causal Green's functions:

$$Z^{--}_{-q-\sigma}(\tau) = - <Ta_{-q-\sigma}(\tau)a_{q\sigma}(0)>, \; Z^{+-}_{q\sigma}(\tau) = - <Ta^+_{q\sigma}(\tau)a_{q\sigma}(0)>,$$

$$Y^{--}_{-pq-\sigma}(\tau) = - <Tc_{-p-\sigma}(\tau)a_{q\sigma}(0)>, \; Y^{+-}_{pq\sigma}(\tau) = - <Tc^+_{p\sigma}(\tau)a_{q\sigma}(0)>, \tag{4.15}$$

In the zero approximation for a self-consistent field, the above Green's functions are interconnected by means of graphical equations in the Fourier space as shown in Fig. 4.1 where the wave lines correspond to interactions according to (4.1), and thin and bold straight lines reflect the frequency dependent Green's functions (4.14) and (4.15) [4.11], respectively. Bold dots represent sums over the inner momenta of the diagram. In the analytical form, these equations are written as follows:

$$Z^{--}_{-q-\sigma}(i\omega_n) = \beta G_1(i\omega_n)\left(\varepsilon_{2-q}Z^{--}_{-q-\sigma}(i\omega_n) + \Delta_{q\sigma}Z^{+-}_{q\sigma}(i\omega_n) + \sum_p T^*_{-p-q}Y^{--}_{-pq-\sigma}(i\omega_n) \right)$$

$$Z^{+-}_{q\sigma}(i\omega_n) = G_2(i\omega_n) - \beta G_2(i\omega_n)\left(\varepsilon_{2q}Z^{+-}_{q\sigma}(i\omega_n) - \Delta^*_{q\sigma}Z^{--}_{-q-\sigma}(i\omega_n) + \sum_p T_{pq}Y^{+-}_{pq\sigma}(i\omega_n) \right)$$

$$Y^{--}_{-pq-\sigma}(i\omega_n) = \beta\tilde{G}_{1-\sigma}(i\omega_n)\left(\varepsilon_{1-p}Y^{--}_{-pq-\sigma}(i\omega_n) + T_{-p-q}Z^{--}_{-q-\sigma}(i\omega_n) \right)$$

$$Y^{+-}_{pq\sigma}(i\omega_n) = \beta\tilde{G}_{2\sigma}(i\omega_n)\left(-\varepsilon_{1p}Y^{+-}_{pq\sigma}(i\omega_n) - T^*_{pq}Z^{+-}_{q\sigma}(i\omega_n) \right),$$

$$\tag{4.16}$$

where $\varepsilon_{1p} = \varepsilon_{1-p}$, $\varepsilon_{2q} = \varepsilon_{2-q}$ and T_{pq} are Fourier transforms of the hopping integrals t_{1ij} and t_{2ij} for N-metal, SC and tunnel matrix element, respectively. Note that the momentum $\mathbf{p}$ always refers to a N-metal, and $\mathbf{q}$ to SC.
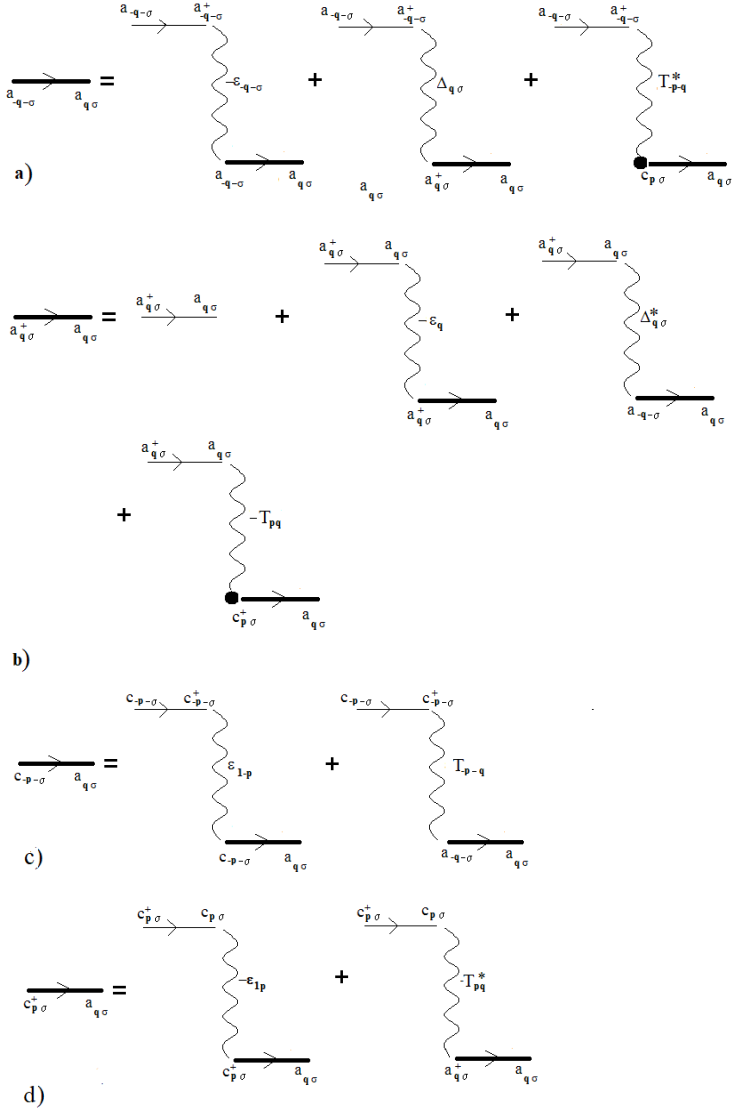

Fig. 4.1 – Graphic system of equations for total causal Green's functions $Z^{--}_{-q-\sigma}(i\omega_n)$, $Z^{+-}_{q\sigma}(i\omega_n)$, $Y^{--}_{-pq-\sigma}(i\omega_n)$ and $Y^{+-}_{pq\sigma}(i\omega_n)$, which determine the spontaneous order parameter $<a_{-q-\sigma}a_{q\sigma}>$ of the superconductor

From the system of Eqs. (4.16), in the absence of tunneling, when $T_{il} = 0$, the trivial solutions $Y_{-pq-\sigma}^{--}(i\omega_n) = 0$ and $Y_{pq\sigma}^{+-}(i\omega_n) = 0$, and the first two equations coincide with the Gor'kov equations. Taking tunneling into account, the system becomes integral and describes nonlinear proximity effects, since it includes infinite series of contributions to the Green's functions from the tunneling matrix element. Despite the integral character of the system in Eqs. (4.16), it can be easily solved. To do this, from the 3-rd and 4-th equations we find the unknown $Y_{-pq-\sigma}^{--}(i\omega_n)$ and $Y_{pq\sigma}^{+-}(i\omega_n)$ and substitute them into the first two equations of the above system, that gives us

$$Z_{-q-\sigma}^{--}(i\omega_n) = \frac{\Delta_{q\sigma}/\beta}{\left[i\omega_n - \xi_q - \tilde{\varphi}_{1-\sigma}(i\omega_n)\right]\left[i\omega_n + \xi_q - \tilde{\varphi}_{2\sigma}(i\omega_n)\right] - \left|\Delta_{q\sigma}\right|^2},$$

$$Z_{q\sigma}^{+-}(i\omega_n) = \frac{\left[i\omega_n - \xi_q - \tilde{\varphi}_{1-\sigma}(i\omega_n)\right]/\beta}{\left[i\omega_n - \xi_q - \tilde{\varphi}_{1-\sigma}(i\omega_n)\right]\left[i\omega_n + \xi_q - \tilde{\varphi}_{2\sigma}(i\omega_n)\right] - \left|\Delta_{q\sigma}\right|^2} \tag{4.17}$$

where $\xi_q = \varepsilon_{2q} - \mu_2$ is the band energy of electrons relatively the Fermi level of the SC.

It is easy to see from expressions (4.17) for the Green's functions that the excitation spectrum of a superconductor in a hybrid structure is incoherent, since $\tilde{\varphi}_{1-\sigma}(\omega)$ and $\tilde{\varphi}_{2\sigma}(\omega)$ contain the finite imaginary parts (see below), determined by the tunnel matrix element.

The functions $\tilde{\varphi}_{1-\sigma}(i\omega_n)$ and $\tilde{\varphi}_{2\sigma}(i\omega_n)$, which determine an FMM effect on a superconductor, are as follows:

$$\tilde{\varphi}_{1-\sigma}(i\omega_n) = \sum_p \frac{\left|T_{pq}\right|^2}{i\omega_n + (\mu_{-\sigma} - \varepsilon_{1p})}$$

$$\tilde{\varphi}_{2\sigma}(i\omega_n) = \sum_p \frac{\left|T_{pq}\right|^2}{i\omega_n - (\mu_\sigma - \varepsilon_{1p})} \tag{4.18}$$

Using the Green's functions (4.17), one can find spontaneous SC gap function by Eq. (4.11)

$$< a_{-q-\sigma} a_{q\sigma} > = -\beta \sum_i \text{Res}\left[Z_{-q-\sigma}^{--}(\omega)(f(\omega)-1)\right]\Big|_i. \tag{4.19}$$

138

Here the symbol Res[…] denotes the residues of the Green's function $Z_{-q-\sigma}^{--}(\omega)$ with a factor $f(\omega)-1$, $f(\omega)=1/(\exp(\omega/T)+1)$ is the Fermi distribution function. The analytical continuation $i\omega_n \to \omega+i\delta$ for $Z_{q\sigma}^{+-}(i\omega_n)=-Z_{q\sigma}^{-+}(-i\omega_n)$ allows us to find a spectrum and a spectral density of electron-hole excitations of the Cooper pair's condensate:

$$R_\sigma(q,\omega)=-2\beta \operatorname{Im} Z_{q\sigma}^{-+}(\omega+i\delta), \qquad (4.20)$$

the coherence degree is controlled by the imaginary part of its poles. Obviously, the scattering of electrons depends only on the tunnel barrier.

Note that the remaining Green's functions describe hoppings of the condensate electrons and holes from SC to N-metal. Indeed, from Eq. (4.16) it follows

$$Y_{pq-\sigma}^{--}(i\omega_n)=\frac{\beta T_{-p-q}\tilde{G}_{1-\sigma}(i\omega_n)}{1-\beta \varepsilon_{1p}\tilde{G}_{1-\sigma}(i\omega_n)} Z_{-q-\sigma}^{--}(i\omega_n)$$

$$Y_{pq\sigma}^{+-}(i\omega_n)=-\frac{\beta T_{pq}^*\tilde{G}_{2\sigma}(i\omega_n)}{1+\beta \varepsilon_{1p}\tilde{G}_{2\sigma}(i\omega_n)} Z_{q\sigma}^{+-}(i\omega_n)$$

$$\qquad (4.21)$$

It can be seen from (4.21) that the indicated Green's functions are proportional to the tunnel matrix elements. The coherent spectrum of electron and hole excitations in an N-metal is expressed as $\omega_{p\sigma}=\pm(\varepsilon_{1p}-\mu_{-\sigma})$ with a quasiparticle peak to be determined by electron tunneling. These excitations correspond to the well-known Andreev reflection process, since they are realized for an arbitrary direction of the electron momentum. It turns out to be the excitations of Andreev reflections in SC are also coherent, since the corresponding Fourier component of the Green's function $Z_{qp\sigma}^{+-}(\tau)=-<Ta_{q\sigma}^+(\tau)c_{p\sigma}(0)>$ has poles determined by zeros of the function [4.11]:

$$d_{q\sigma}(\omega)=\frac{(\omega-E_{q\sigma})(\omega+E_{q\sigma})}{\omega^2-\mu_2^2}, \qquad (4.22)$$

where $E_{q\sigma}=\sqrt{(\varepsilon_q-\mu_2)^2+|\Delta_{q\sigma}|^2}$ is the spectrum of electron excitations with Cooper pairing, which do not depend on the tunnel matrix element.

To determine the spontaneous gap accordingly to Eq. (4.19), after the analytic continuation $\omega \to \omega + i\delta$, it is necessary to calculate the functions $\tilde{\varphi}_{1-\sigma}(\omega)$ and $\tilde{\varphi}_{2\sigma}(\omega)$. Obviously, these functions are connected by the relation

$$\tilde{\varphi}_{1-\sigma}(\omega) = -\tilde{\varphi}_{2-\sigma}(-\omega) \tag{4.23}$$

Next, we consider the simplest case $|T_{pq}|^2 = |B|^2$, when the tunnel matrix element does not depend on the wave vectors. The frequency ω is supposed to be complex valued and $|\omega/\mu_1| \ll 1$. Taking into account that the electron density of states $\rho_S(\varepsilon) = C_S\sqrt{\varepsilon}$ with the constant C_S proportional to the volume V_N of the N-metal, the calculation of integrals (4.18) is elementary and we obtain:

$$\begin{aligned} \tilde{\varphi}_{1-\sigma}(\omega) &= \varphi_0(\omega, \Gamma_N) = -\Gamma_N\left(2 + \ln\left(\frac{\omega}{4\mu_1}\right)\right) \\ \tilde{\varphi}_{2\sigma}(\omega) &= \Gamma_N\left(2 + \ln\left(\frac{-\omega}{4\mu_1}\right)\right) \end{aligned}, \tag{4.24}$$

where the value $\Gamma_N = |B|^2\rho_N(\mu_1)$ determines the barrier transparency for FMM electrons. It is also clear that the contribution from magnetism under the sign of the logarithm is infinitesimal of a higher order than $|\omega/\mu_1|$. Therefore, an influence of the N-metal magnetic ordering on SC can be neglected and spin indices in Eq. (4.24) may be disregarded. Since the branch cut of complex functions (4.24) lies on the negative frequency axis ω, it is necessary to take into account the following relation:

$$\ln(\omega) - \ln(-\omega) = i\pi \, sign(\arg \omega) \tag{4.25}$$

One can write an equation for pole singularities of the Green's functions (4.17) and find the gap in SC:

$$\omega^2 - \omega\left[\tilde{\varphi}_1(\omega) + \tilde{\varphi}_2(\omega)\right] + \xi_q\left[\tilde{\varphi}_2(\omega) - \tilde{\varphi}_1(\omega)\right] + \tilde{\varphi}_1(\omega)\tilde{\varphi}_2(\omega) - \xi_q^2 - |\Delta_{q\sigma}|^2 = 0, \tag{4.26}$$

where $\tilde{\varphi}_{1-\sigma}(\omega) = \tilde{\varphi}_1(\omega)$ and $\tilde{\varphi}_{2\sigma}(\omega) = \tilde{\varphi}_2(\omega)$ in accordance with aforesaid. Formally, this equation can be considered as quadratic with respect to the complex frequency ω. It allows to write the implicit solution in the form

$$\omega_{q\sigma}^{\pm} = -\frac{1}{2}i\pi\Gamma_N sign(\arg \omega_{q\sigma}^{\pm}) \pm \sqrt{\left(\xi_q - \Gamma_N\left(2 + \ln\left[\frac{\omega_{q\sigma}^{\pm}}{4\mu_1}\right]\right) + \frac{1}{2}i\pi\Gamma_N sign(\arg \omega_{q\sigma}^{\pm})\right)^2 + \left|\Delta_{q\sigma}\right|^2} \quad (4.27)$$

Unfortunately, Eq. (4.27) is transcendental relative to the unknown $\omega_{q\sigma}^{\pm}$. However, it is easy to obtain solutions for both electron and hole excitations by the iteration procedure. As a start, it is necessary to set $\omega_{q\sigma} = E_{q\sigma} + i\delta$ that corresponds to the analytic continuation of the Green's functions to the complex upper half-plane. The iterative procedure for calculating the roots determines solutions with imaginary parts of the opposite sign for each root. This uncertainty for the roots appears due to the replacement $\omega \rightarrow \omega + i\delta$ at the analytic continuation of Green's functions (4.17) for each iteration step in Eq. (4.27) because logarithm gives roots on opposite edges of the branch cut. It is clear that the first step of the iteration determines the sign of the imaginary part of the pole, and the next step of the opposite sign is associated with the violation of the selected condition for interaction adiabatic switching on. It is interesting to note that in [4.12] only the 1-st iteration step was applied to Eq. (4.27). As will be shown below, the rigorous self-consistency over frequencies $\omega_{q\sigma}^{\pm}$ drastically changes the order parameters pointing out on a significant contribution $\ln\left[\omega_{q\sigma}^{\pm}/4\mu_1\right]$ to the proximity effect in the FMM-SC structure.
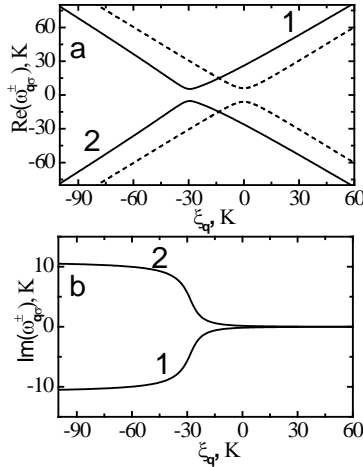

Fig. 4.2 – Real (a) and imaginary (b) parts of the electron and hole excitations spectrum $\omega_{q\sigma}^{+}$ and $\omega_{q\sigma}^{-}$ (solid curves 1 and 2, respectively) for the FMM-SC hybrid structure, $\Delta = 6$ K, $\Gamma_N = 3.495$ K and $\mu = 6$ eV, as well as the corresponding coherent BCS spectrum (dashed curves)

Fig. 4.2 shows real and imaginary parts of the poles as a function of the electron energy ξ_q relative to the Fermi energy level for the gap $\Delta = 6$ K, barrier transparency $\Gamma_N = 3.49$ K and $\mu_1 = 6$ eV (solid lines). The BCS spectrum (dashed line) is demonstrated for comparison.

To find the solution $\Delta_{q\sigma}$ from Eq. (4.10) after finding the self-consistent solutions $\omega_{q\sigma}^+ = \omega_{q\sigma}$ and $\omega_{q\sigma}^- = -\omega_{q\sigma}$ for the poles $Z_{-q-\sigma}^{--}(\omega)$ from Eq. (4.19), it is necessary to make an obvious replacement $\tilde{\varphi}_1(\omega) = \tilde{\varphi}_1(\omega_{q\sigma}^+)$ and $\tilde{\varphi}_2(\omega) = \tilde{\varphi}_2(\omega_{q\sigma}^+)$ in Eq. (4.26). Note that Eq. (4.26) is invariant under the substitution $\omega_{q\sigma}^+ \to \omega_{q\sigma}^-$ (see Eq. (4.23)). Thus, the anomalous Green's function takes the simplest form

$$Z_{-q-\sigma}^{--}(i\omega_n) = \frac{\Delta_{q\sigma} / \beta}{\left(i\omega_n - \omega_{q\sigma}\right)\left(i\omega_n + \omega_{q\sigma}\right)}, \tag{4.28}$$

that gives the order parameter

$$< a_{-q-\sigma} a_{q\sigma} > = \frac{\Delta_{q\sigma}}{2\omega_{q\sigma}} \tanh\left(\frac{\omega_{q\sigma}}{2T}\right). \tag{4.29}$$

The gap function is a complex value for $\Gamma_N \neq 0$, and for $\Gamma_N = 0$ it coincides with the BCS theory result. Then, according to Eq. (4.10), we obtain a self-consistent equation for the complex gap $\Delta_{q\sigma}$:

$$\Delta_{k\sigma} = \sum_q V_{k-q}^{el-ph} \frac{\Delta_{q\sigma}}{2\omega_{q\sigma}} \tanh\left(\frac{\omega_{q\sigma}}{2T}\right) \tag{4.30}$$

Assuming that the electron-phonon interaction parameter $V_{k-q}^{el-ph} = U$ is nonzero near the Fermi level in a narrow energy region of the order of $\pm \omega_D$, where ω_D is the Debye frequency, let us denote the electron-phonon coupling constant for SC by $\lambda = \rho_F(\mu_2)U$. Here $\rho_F(\mu_2)$ is the electron density of states at the Fermi surface. Obviously, $\rho_F(\mu_2)$ does not depend on the sample volume. Then one can obtain the integral complex equation for the spontaneous gap

$$\Delta_{k\sigma} = \lambda \int_{-\omega_D}^{\omega_D} \frac{\Delta_{q\sigma}}{2\omega_{q\sigma}} \tanh\left(\frac{\omega_{q\sigma}}{2T}\right) d\xi_q \tag{4.31}$$

In the simple case of the s-wave gap with a spatially homogeneous phase, $\Delta_{k\sigma} = \Delta = \Delta_S e^{i\varphi}$, where $\Delta_S = |\Delta_{k\sigma}|$, and φ is determined by the rest of the integrand

in Eq. (4.31), which depends on Γ_N. In the approximation $\varphi = $ const and at $\Gamma_N = 0$, this phase is equal to zero. For a gap under the integral one can put $\Delta_{q\sigma} = \Delta_S e^{i0}$. Taking the modulus from both sides of Eq. (4.31) with account for the indicated replacement, we obtain the equation for the gap modulus:

$$1 = \lambda \left| \int_{-\omega_D}^{\omega_D} \frac{1}{2\omega_{q\sigma}} \tanh\left(\frac{\omega_{q\sigma}}{2T}\right) d\xi_q \right|, \qquad (4.32)$$

Since the modulus of the right-hand side of Eq. (4.32) is equal to 1, it can be assumed that the corresponding complex number also determines the gap phase φ that makes it possible to write

$$\varphi = \arg\left(\lambda \int_{-\omega_D}^{\omega_D} \frac{1}{2\omega_{q\sigma}} \tanh\left(\frac{\omega_{q\sigma}}{2T}\right) d\xi_q \right) \qquad (4.33)$$

Thus, using Eqs. (4.32)–(4.33), it is able to calculate an absolute value of the spontaneous gap Δ_S of SC, its phase φ, and the critical temperature T_C of the phase transition, taking into account an influence of the effects of incoherent electrons tunneling in a normal metal.
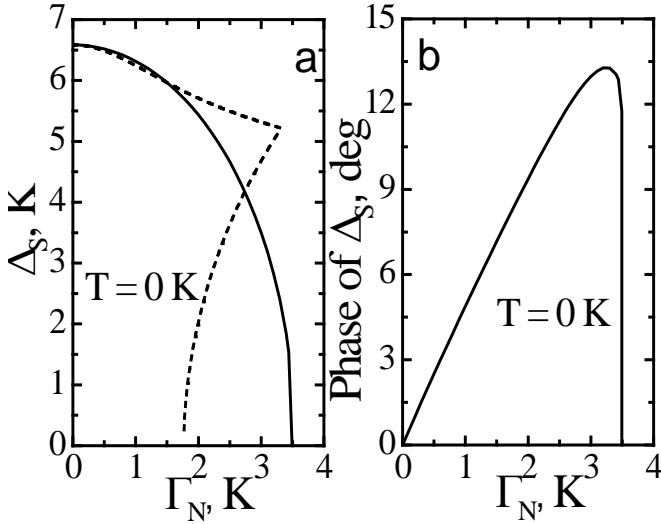
In Fig. 4.3a, the dependence of the spontaneous gap Δ_S of the Sn superconductor on the barrier transparency Γ_N at the temperature $T = 0$ (solid curve), which describes an inverse proximity effect, is shown. The dashed curve was obtained for the poles in Eq. (4.27) obtained at the first step of the iteration [4.12].

The critical value of transparency $\Gamma_N = \Gamma_N^{cr} = 3.495$ K, above which the superconductivity is destroyed, is determined from the equation for T_C at $\tanh\left(\frac{\omega_1(\xi_q)}{2T}\right) = 1$:

$$F(T, \Gamma_N) = \lambda \left| \int_{-\omega_D}^{\omega_D} \frac{1}{2\omega_1(\xi_q)} \tanh\left(\frac{\omega_1(\xi_q)}{2T}\right) d\xi_q \right| - 1 = 0, \qquad (4.34)$$

where the frequency $\mathrm{Re}(\omega_1(\xi_q)) > 0$ and $\omega_1(\xi_q)$ is the self-consistent solution of Eq. (4.27) at $|\Delta_{q\sigma}| = 0$. Near the high transparency a role of cooperative phenomena associated with electron-hole scattering by a barrier increases significantly, that is indicated by the order parameter phase (see Fig. 4.3b). On

the other hand, the temperature fluctuations partially stabilize the superconducting state, since high-energy electrons from the normal metal are more strongly dissipated. Therefore, with decreasing temperature, an area of the ordered phase for a highly transparent barrier narrows. In general, the state of itinerant electrons itself is rather complex, that is reflected in the form of a nonmonotonic behavior of the phase transition critical temperature T_C, as well as an appearance of the reentrant superconductivity in certain temperature areas.

Fig. 4.3 – Dependence of the spontaneous gap Δ_S (a) and its phase (b) of superconductor Sn on the barrier transparency Γ_N at the temperature $T = 0$ (solid curve).
The dashed curve reflects the same dependence but without self-consistency over the poles from Eq. (4.27) (the first iteration step in Eq. (4.27) [4.12]).
The parameters values for tin are as follows: $\lambda = 0.245$, $\omega_D = 195$ K, $\mu_1 = 6$ eV

Fig. 4.4 shows that the critical temperature T_C at $\Gamma_N \sim \Gamma_N^{cr}$ for FMM-Sn and FMM-Pb hybrid structures is the multiple-valued function of Γ_N. Also, T_C strongly fluctuates relative to small changes in Γ_N, when approaches the zero temperature. With further growth Γ_N, T_C even increases but in this case, superconductivity at low temperatures disappears, and the high-temperature area of the nonzero order parameter gradually narrows to zero.
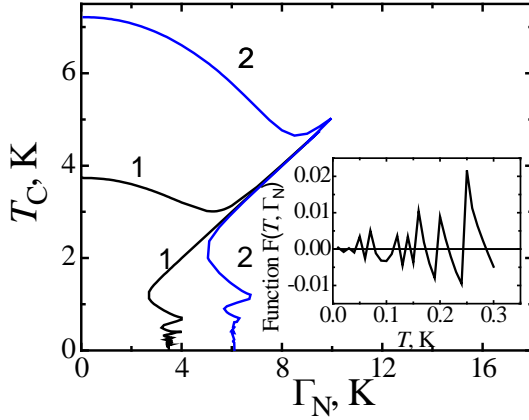
Fig. 4.4 – Phase diagram of FMM-Sn and FMM-Pb structures (curves 1 and 2, respectively). For Pb, the values $\mu_2 = 9.9$ eV, $\lambda = 0.39$, $\Gamma_N^{cr} = 6.105$ K and $\omega_D = 96$ K are taken. The inset shows the function $F(T, \Gamma_N)$ from Eq. (4.34) at $\Gamma_N = \Gamma_N^{cr} = 3.495$ and low T, the zeros of which determine T_C of the superconductor
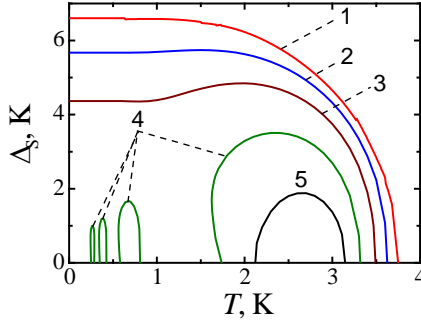

Fig. 4.5 – Temperature dependences of the spontaneous gap Δ_S of the normal metal-tin structure at barrier transparency values $\Gamma_N = 0$, 1.8, 2.65, 3.495, and 4.25 K (curves 1–5, respectively) with the parameter values from Fig. 4.3

In Fig. 4.5, temperature dependences of the gap Δ_S of tin in N-metal-Sn hybrid structure are shown for different values of the barrier transparency Γ_N. It can be seen from the figure that at $\Gamma_N \sim \Gamma_N^{cr}$ the order parameter exists in certain temperature regions, $i.\ e.$, in this case an emergence of reentrant super-conductivity is possible. With decreasing temperature, as well as with in-creasing Γ_N, the area of the superconductivity existence narrows. Also, near one of the critical temperatures, a two-gap state is possible, that may indicate a first-order phase transition. Since the phase of the gap is directly related to

the incoherent scattering of tunnel electrons by the barrier, its temperature dependences for different transparencies Γ_N are of interest.

Figure 4.6 shows temperature dependences of phases for gap functions from Fig. 4.5. It can be seen that the phase near the "left" critical temperature, increases sharply while near the "right" one, it decreases monotonically until abruptly disappearing when $\Delta_S = 0$. Thus, the presented dependences T_C and Δ_S reflect complex nature of the relationship between incoherent tunneling electron scattering, thermal fluctuations, and coherent Cooper pairing.
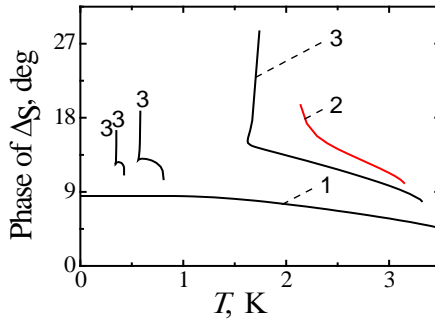
Fig. 4.6 – Temperature dependences of the gap phase φ with moduli Δ_S from Fig. 4.5 for transparencies Γ_N = 1.8, 3.495 and 4.25 K (curves 1–3, respectively) and with the parameter values from Fig. 4.3
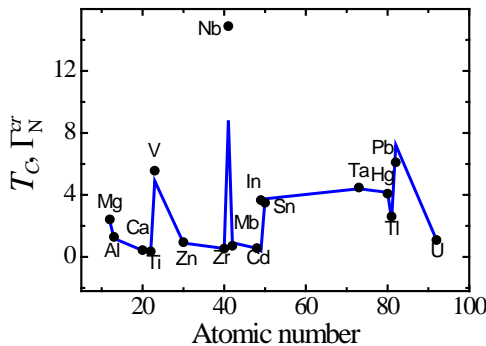

Fig. 4.7 – Critical barrier transparencies Γ_N^{cr} (points) and temperatures T_C (top of the broken line) [4.15] for various metals

In Fig. 4.7, critical temperatures (according to the data of Ref. [4.15]) and the calculated transparencies Γ_N^{cr} for series of superconductors are shown. It can be seen that with the exception of Nb, the values of T_C and Γ_N^{cr} differ

insignificantly. Thus, one can say that the critical barrier transparency is mainly determined by the value of T_C, and the reentrant superconductivity is possible with such a high transparency.

The expression for the spectral density of states $R_\sigma(\boldsymbol{q},\omega)$ from Eq. (4.20) takes the form:

$$R_\sigma(\boldsymbol{q},\omega) = -2\pi\Gamma_N \frac{\theta(\omega)\left[\omega^2 - \tilde{E}_q^2\right] - (\omega + \tilde{\xi}_q)(\omega - sign(\omega)\tilde{\xi}_q)}{\left[\omega^2 - \tilde{E}_q^2\right]^2 + \pi^2\Gamma_N^2(\omega - sign(\omega)\tilde{\xi}_q)^2}, \tag{4.35}$$

where $\tilde{E}_q(\omega) = \sqrt{\tilde{\xi}_q^2(\omega) + \Delta_s^2}$, $\tilde{\xi}_q(\omega) = \xi_q + \varphi_0(|\omega|, \Gamma_N)$, $\theta(\omega)$ is the Heaviside step function, and $\varphi_0(\omega, \Gamma_N)$ is the function from Eqs. (4.24). Let us define the homogeneous spectral density as

$$R_U^s(\omega) = \sum_{\boldsymbol{q}} R_\sigma(\boldsymbol{q},\omega) = \rho_S(\mu_2) \int_{-\omega_D}^{\omega_D} d\xi_q R_\sigma(\boldsymbol{q},\omega), \tag{4.36}$$

where $\rho_S(\mu_2)$ is the bulk electron density of states of a SC metal at the Fermi level.
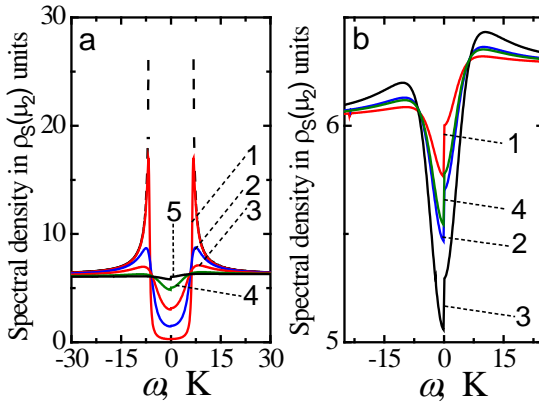

Fig. 4.8 – Frequency dependences of the homogeneous spectral density $\tilde{R}(\omega)$ from Eq. (4.35) in units $\rho_S(\mu_2)$ for the superconductor in a hybrid structure "normal metal-Sn": a) at the temperature $T = 0$ and $\Gamma_N = 0$ ($\Delta_S = 6.6$ K, dashed line), 0.2, 1.0, 2.0, 3.0 and 3.44 K ($\Delta_S = 6.57$, 6.32, 5.44, 3.50, 1.54, solid lines 1–5, respectively); b) at the critical transparency $\Gamma_N = \Gamma_N^{cr} = 3.495$ K and $T = 1.625$, 1.7, 2.4, 3.1 ($\Delta_S = 1.7$, 2.53, 3.51, 2.34, curves 1–4, respectively)

In Fig. 4.8 the frequency dependences of a homogeneous spectral density of the superconductor Sn at the temperature $T = 0$ K for different Γ_N values and at critical transparency $\Gamma_N = \Gamma_N^{cr} = 3.495$ K in the temperature area from 1.6 to 3.1 K, where the reentrant superconductivity is realized, are shown. It can be seen from Fig. 4.8a that for small Γ_N the $R_U^S(\omega)$ is close to the conventional $R_\sigma^S(\omega)$ for a homogeneous superconductor:

$$R_\sigma^S(\omega) = \frac{2\pi\rho_s(\mu_2)|\omega|}{\sqrt{\omega^2 - \Delta_s^2}} \tag{4.37}$$

With increasing Γ_N, the spectral density $\tilde{R}(\omega)$ approaches the value of $2\pi\rho_s(\mu_2)$ that corresponds to N-metal and reflects the inverse proximity effect. In Fig. 4.7b, $\tilde{R}(\omega)$ is shown at the critical transparency $\Gamma_N^{cr} = 3.495$ K, and in the temperature area of the reentrant superconductivity appearance. It can be seen from the figure that in this case, due to a high barrier transparency, an influence of the N-metal on the spontaneous order parameter is quite significant. Also, due to the jump at the singular point $\omega = 0$, $\tilde{R}(\omega)$ is asymmetric near the origin. The presented dependences are in a good agreement with the known experimental data [4.16].

4.4 Proximity effect in a ferromagnetic metal

In this subsection, we will consider an influence of SC on a FMM, *i. e.*, a proximity effect associated with the emergence of an induced gap in the specified metal. It was shown above, that the magnetic order of an N-metal has a negligible effect on the SC. It turns out that the SC significantly affects both transport in a metal due to the proximity effect and its spectral properties. In a similar way, we can obtain expressions for corresponding electron Green's functions of a metal using the induced order parameter $< c_{-p-\sigma} c_{p\sigma} >$, spectrum of excitations, and their damping. The details are presented in the work [4.11]. Therefore, we can write down the expressions for the Fourier transforms of the retarded anomalous $Y_{p\sigma}^{--}(\tau) = - < Tc_{-p-\sigma}(\tau)c_{p\sigma}(0) >$ and conventional $Y_{p\sigma}^{-+}(\tau) = - < Tc_{p\sigma}(\tau)c_{p\sigma}^{+}(0) >$ Green's functions of the N-metal:

$$Y_{p\sigma}^{--}(\omega+i\delta) = -\frac{1}{\beta}\frac{\tilde{\beta}\ (\omega+i\delta)}{\Omega_{p\sigma}(\omega+i\delta)}$$

$$Y_{p\sigma}^{-+}(\omega+i\delta) = \frac{1}{\beta}\frac{\omega+i\delta+\xi_p+J_0\sigma-\tilde{\gamma}\ (\omega+i\delta)}{\Omega_{p\sigma}(\omega+i\delta)}, \qquad (4.38)$$

where

$$\Omega_{p\sigma}(\omega+i\delta) = (\omega+i\delta+\xi_p-J_0\sigma-\tilde{\gamma}\ (\omega+i\delta))(\omega+i\delta-\xi_p-J_0\sigma-\tilde{\alpha}\ (\omega+i\delta))-\left|\tilde{\beta}\ (\omega+i\delta)\right|^2, \ (4.39)$$

$\xi_p = \varepsilon_{1p} - \mu_1$, $\Gamma_S = \rho_S(\mu_2)B^2$ is the barrier transparency for SC condensate electrons. Also, we have the following equations

$$\tilde{\alpha}(\omega) = -\Gamma_S\left\{2+\ln\frac{b(\omega)}{4\mu_2}+\frac{1}{2}i\pi\left[\frac{\omega}{b(\omega)}sign(\arg(b(\omega)))+sign(\arg(-b(\omega)))\right]\right\}$$

$$\tilde{\beta}(\omega) = -\Delta\Gamma_S\frac{i\pi}{2b(\omega)}sign(\arg(b(\omega))) \qquad , \qquad (4.40)$$

$$\tilde{\gamma}(\omega) = \Gamma_S\left\{2+\ln\frac{b(\omega)}{4\mu_2}-\frac{1}{2}i\pi\left[\frac{\omega}{b(\omega)}sign(\arg(b(\omega)))-sign(\arg(-b(\omega)))\right]\right\}$$

where $b(\omega) = \sqrt{\omega^2-|\Delta|^2}$. The spectrum of excitations is found from pole singularities of the indicated Green's functions, *i. e.*, at the condition $\Omega_{p\sigma}(\omega+i\delta)=0$ that gives an equation for the resonance frequencies ω with account for the analytical continuation $\omega > \omega + i\delta$:

$$\omega-J_0\sigma = -\frac{1}{2}i\pi\Gamma_S\frac{\omega}{b(\omega)}sign\left(\arg\left[b(\omega)\right]\right)\pm$$

$$\pm\sqrt{\left(\xi_p-\Gamma_S\left(2+\ln\left[\frac{b(\omega)}{4\mu_2}\right]\right)-i\pi\Gamma_S sign\left(\arg\left[-b(\omega)\right]\right)\right)^2-\pi^2\Gamma_S^2\frac{|\Delta|^2}{4b^2(\omega)}} \qquad (4.41)$$

The transcendental Eq. (4.41) has complex roots $\omega_{1\sigma p}$ and $\omega_{2\sigma p}$, which are determined numerically by the iteration procedure.
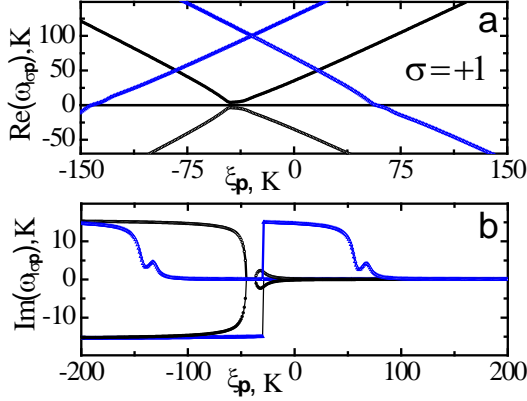
Fig. 4.9 – Real (a) and imaginary (b) parts of the excitation electron frequencies $\omega_{1\sigma p}$
(dark circles and triangles) and $\omega_{2\sigma p}$ (open circles and triangles) as functions
of the electron energy ξ_p with the barrier transparency $\Gamma_S = 5$ K, the gap $\Delta_S = 6.6$ K
and the ferromagnetic exchange $J_0 = 0$ and 100 K (circles and triangles, respectively)

Fig. 4.9 shows results of the calculations for $\omega_{1\sigma p}$ and $\omega_{2\sigma p}$ as a function of energy ξ_p for both paramagnetic and ferromagnetic N-metals. It can be seen that for a paramagnet in a certain range of values ξ_p and at frequencies $|\omega| < |\Delta|$, the gap is induced in the N-metal as a realization of the proximity effect with a nonzero anomalous order parameter $< c_{-p-\sigma} c_{p\sigma} >$, which is suppressed by the ferromagnetic exchange. Note that the correlator $< c_{-p-\sigma} c_{p\sigma} >$ does not depend on the electron-phonon coupling constant in the N-metal and is proportional to the gap Δ, since the N-metal is not a superconductor. On the whole, the spectrum is incoherent for nonzero Γ_S. At the same time, electron excitations with frequencies $|\omega| < |\Delta|$ are coherent. Let us consider this issue in more detail, since it is necessary for the correct calculation of the corresponding spectral density.

Indeed, it is easy to see that at $|\omega| < |\Delta|$ the tunnel functions (4.40) are real. The equation $\Omega_{p\sigma}(\omega) = 0$ is quadratic relatively unknown ξ_p for the integrand pole singularities of the homogeneous spectral density $R_U^N(\omega)$:

$$R_U^N(\omega) = \sum_p \tilde{R}_\sigma(\boldsymbol{p}, \omega) = \rho_N(\mu_1) \int_{-\tilde{\omega}_D}^{\tilde{\omega}_D} d\xi_p \tilde{R}_\sigma(\boldsymbol{p}, \omega), \tag{4.42}$$

150

where $\tilde{R}_\sigma(\boldsymbol{p},\omega)=-2\beta\operatorname{Im}Y_{p\sigma}^{-+}(\omega+i\delta)$ and $\tilde{\omega}_D$ is Debye frequency for N-metal. That is why one can write its solutions $\xi_1(\omega)$ and $\xi_2(\omega)$ in the form:

$$\xi_{1,2}(\omega)=\Gamma_S\left(2+\ln\frac{\tilde{b}(\omega)}{4\mu_2}\right)\pm\sqrt{\left(\omega+J_0\sigma\right)\left(\omega+J_0\sigma+\Gamma_S\frac{\pi\omega}{\tilde{b}(\omega)}\right)-\frac{1}{4}\pi^2\Gamma_S^2},\qquad(4.43)$$

where $\tilde{b}(\omega)=\sqrt{\Delta_S^2-\omega^2}$. Evidently, Eq. (4.43) gives poles on the real frequency axis if the radical expression is non-negative. Consider the simplest case $J_0=0$. Then at

$$\Gamma_S\le\frac{2|\omega|\{|\omega|+\Delta_S\}}{\pi\sqrt{\Delta_S^2-\omega^2}}=g(\omega)\qquad(4.44)$$

we have the coherent spectrum, if $|\omega|<\Delta_S$ and $|\omega|>g^{-1}(\Gamma_S)=\omega_0(\Gamma_S)$, where $g^{-1}(x)$ is the inverse function from Eq. (4.44). The numerical analysis with analytical continuation $\omega\to\omega+i\delta$ shows that $sign(\operatorname{Im}(\xi_1(\omega+i\delta)))=sign(\omega)$ and $sign(\operatorname{Im}(\xi_2(\omega+i\delta)))=-sign(\omega)$. In accordance with the Landau bypass rule, it is easy to find the spectral density of coherent electron excitations in N-metal for frequencies $|\omega|<\Delta_S$.

$$R_U^N(\omega)=\frac{2\pi sign(\omega)\theta(|\omega|-\omega_0(\Gamma_S))\theta(\Delta_S-|\omega|)\rho_N(\mu_1)}{\sqrt{\omega\left(\omega+\Gamma_S\frac{\pi\omega}{\tilde{b}(\omega)}\right)-\frac{1}{4}\pi^2\Gamma_S^2}}\left\{\omega+\Gamma_S\frac{\pi\omega}{\tilde{b}(\omega)}\right\}.\qquad(4.45)$$

Fig. 4.10 shows the spectrum of coherent electronic excitations $\omega_{1,res}$ and $\omega_{2,res}$ from Eq. (4.43) in a paramagnetic N-metal at $\Delta_S=6.6$ K, $\Gamma_S=0.5$ and 5 K in the frequency region $|\omega_{i,res}|<\Delta_S$, as well as the corresponding homogeneous spectral densities of coherent and incoherent excitations from Eq. (4.41) at $|\omega_{i\sigma p}|>\Delta_S$. In Fig. 4.10a one can see that at $|\omega|<\Delta_S$ in the N-metal, a forbidden band is also formed. Its width depends both on the barrier transparency and on the SC gap. Also, in this case, the induced gap does not depend on the electron-phonon coupling constant in the N-metal. The main energy interval of electrons scattered by the barrier is assumed to be near the Fermi level with a width of the order of twice the Debye frequency. The spectral density in Fig. 4.10b reflects the coherence of the indicated excitations

with an increase in the quasiparticle peak as one approaches the boundaries of the forbidden band of the SC and N-metal. It is interesting to note that in the forbidden zone of the N-metal, *i. e.*, at $|\omega| < \omega_0(\Gamma_S)$, in contrast to the SC, there are purely complex poles of the Green's function $Y_{p\sigma}^{-+}(\omega + i\delta)$ that point out on strong electrons scattering. It can be shown that the corresponding spectral density is identically equal zero, as in the SC.
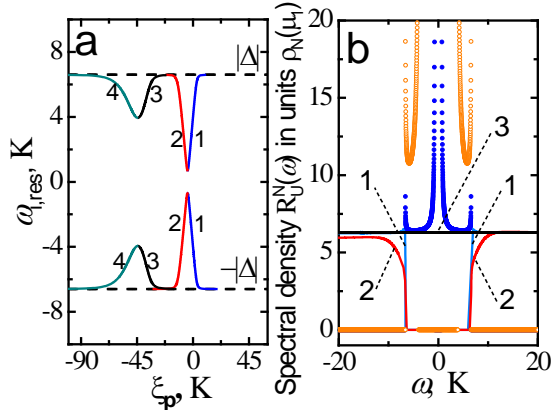

Fig. 4.10 – (a) Spectrum of coherent electron excitations $\omega_{1,res}$ and $\omega_{2,res}$ in a paramagnetic N-metal at $|\Delta| = \Delta_S = 6.6$ K and $\Gamma_S = 0.5$ (curves 1 and 2, respectively) and 5 K (curves 3 and 4, respectively) at frequencies $|\omega_{i\sigma p}| > \Delta_S$; (b) corresponding homogeneous spectral densities of incoherent excitations in the area $|\omega_{i\sigma p}| > \Delta_S$ at $\Gamma_S = 0.5$ and 5 K (solid curves 1 and 2, respectively) and of coherent excitations from Fig. 4.10a at $\Gamma_S = 0.5$ and 5 K (dark and light points, respectively). The straight line 3 corresponds to the spectral density value 2π in units $\rho_N(\mu_1)$ for an N-metal with a coherent spectrum

The problem considered above corresponds to the simplest case when there is no electron-phonon interaction in the N-metal. Here, it is necessary to take into account an effective field in the N-metal formed by the order parameter $<c_{-p-\sigma}c_{p\sigma}>$ with a corresponding energy gap function

$$\tilde{\Delta}_{k\sigma} = \sum_q \tilde{V}_{k\text{-}p}^{el.-ph} <c_{-p-\sigma}c_{p\sigma}>, \tag{4.46}$$

despite $\tilde{\Delta}_{k\sigma}$ being induced by the effective field of the SC. However, it can be assumed that the induced effective field in the N-metal weakly affects the

self-consistent SC order parameter, especially for highly transparent barriers. Indeed, the induced homogeneous gap function $\Delta_N = \left|\tilde{\Delta}_{k\sigma}\right|$ is represented in the form:

$$\Delta_N = \left| \begin{array}{l} -\dfrac{1}{2}\tilde{\lambda}i\pi\Gamma_S\Delta \times \\ \displaystyle\int\limits_{-\tilde{\omega}_D}^{\tilde{\omega}_D} d\xi_p \dfrac{1}{\omega_{1\sigma p} - \omega_{2\sigma p}} \left\{ \dfrac{\left[f(\omega_{1\sigma p})-1\right]sign\left(\arg\left[b(\omega_{1\sigma p})\right]\right)}{b(\omega_{1\sigma p})} - \dfrac{\left[f(\omega_{2\sigma p})-1\right]sign\left(\arg\left[b(\omega_{2\sigma p})\right]\right)}{b(\omega_{2\sigma p})} \right\} \end{array} \right|, \quad (4.47)$$

where $\omega_{1\sigma p}$ and $\omega_{2\sigma p}$ are the roots of Eq. (4.41). Fig. 4.11 shows the dependences of the gap Δ_N on the SC transparency Γ_S at temperature $T = 0$ for various values of Γ_N in the "Al–Sn" hybrid structure where the values $\tilde{\lambda} = 0.175$ and $\tilde{\omega}_D = 423$ K are taken for Al [4.17]. It can be seen that with increasing Γ_S the induced Δ_N increases and then decreases to a value which then weakly depends on electron tunneling. Also, with increasing Γ_N, there is a decrease in Δ_N. Note that the value of the spontaneous gap Δ_S in the absence of tunneling is equal to 6.6 K, *i. e.*, significantly exceeds Δ_N.
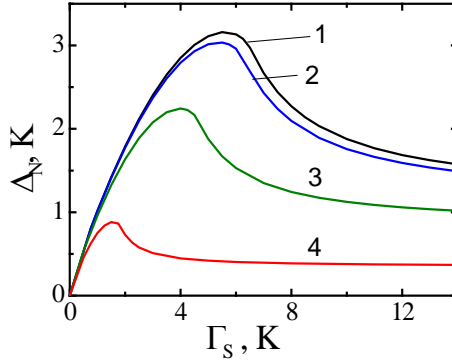

Fig. 4.11 – Gap function Δ_N as a function of the SC transparency Γ_S at the temperature $T = 0$ for different values of the barrier transparencies Γ_N of the N-metal equal to 0.2, 1, 2.5, and 3.4 K (curves 1–4, respectively)

In Fig. 4.12, temperature dependences of the induced in Al gap function with $\Gamma_N = 2.65$ (a) and $\Gamma_N = \Gamma_N^{cr} = 3.495$ K (b) are presented. It can be seen from Fig. 4.12a that with increasing Γ_S the gap Δ_N increases and then decreases in accordance with Fig. 4.11. In this case, only for large transparencies Γ_S a nonmonotonic temperature dependence of Δ_N is observed, and for small Γ_S the

induced gap function decreases monotonically with increasing T. Fig. 4.12b shows the temperature dependences of reentrant induced superconductivity at the critical value Γ_N, reflecting a rather complex process of the proximity effect realization in the given hybrid structure.
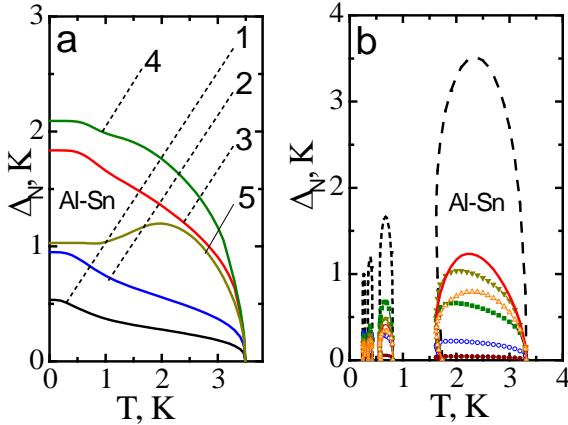

Fig. 4.12 – Temperature dependences of the induced in aluminum gap function Δ_N with $\Gamma_N = 2.65$ (a) and 3.495 K (b) for different barrier transparencies Γ_S of tin: a) 0.5, 1, 2.5, 3.5, and 10 K (curves 1–5, respectively); b) 0.1 (dark points), 0.5 (light points), 1.5 (dark squares), 2.5 (dark triangles), 3.5 (solid line) and 10 K (light triangles). The dotted curve corresponds to spontaneous reentrant superconductivity at the critical transparency $\Gamma_N = 3.495$ in Fig. 4.5
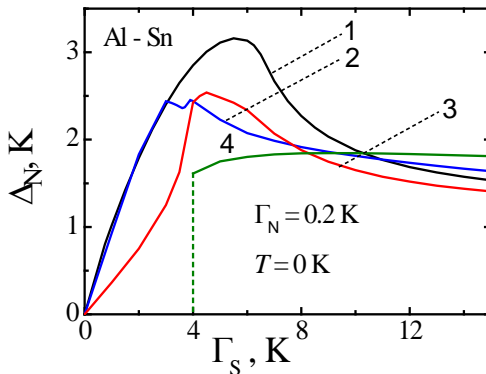

Fig. 4.13 – Induced gap Δ_N as a function of the barrier transparency Γ_S in the ground state for exchange values J_0 equal to 0 (curve 1) and 6 K (curves 2 and 3 at $\sigma = 1, -1$, respectively). Curve 4 corresponds to $J_0 = 10$ K and $\sigma = 1$

At the end, let us study the FM exchange effect on the gap in the N-metal. As mentioned above, the exchange interaction shifts energy bands up and down, depending on the sign of the spin parameter σ, and decreases the gap as well (see Fig. 4.9). Fig. 4.13 shows the gap function Δ_N as a function of the transparency of SC Γ_S at temperature $T = 0$ for various values of the exchange interaction parameter J_0 and spin indices σ equal to 0 (curve 1) and 6 K (curves 2 and 3 at $\sigma = 1, -1$, respectively). It can be seen that at $J_0 < \Delta_S$ in area of the gap maximum for FM the exchange suppresses Δ_N, although for high transparencies the decrease in Δ_N is not so significant. Also, the gaps for the spins $\sigma = 1$ and $\sigma = -1$ differ significantly, that is caused by the asymmetric exchange shift of the electron energy bands with corresponding spins. For $J_0 > \Delta_S$ the difficulties arise in calculating Δ_N at low transparencies Γ_S due to oscillations of the integrand in Eq. (4.47). Therefore, curve 4 at $J_0 = 10$ K in Fig. 4.13 ends abruptly at $\Gamma_S = 4$ K.

4.5 Conclusions

In this chapter, the application of time perturbation theory to a model, in which a self-consistent uniform effective field formed by the electron-phonon coupling of SC induces an order parameter in a N-metal due to electron tunneling, has been considered. Electron-electron scattering has not been taken into account that is true for tunnel areas with linear sizes, which do not exceed an electron mean free path.

It was found that at the critical transparency Γ_N values of the order of the SC critical temperature T_C, tunneling electrons of the N-metal destroy the spontaneous superconductivity in the ground state. The presence of incoherent excitations leads to a complex relationship between the ordering effects, thermal fluctuations, and tunneling, which in the vicinity of $\Gamma_N \sim \Gamma_N^{cr}$ can stabilize the superconducting state in certain temperature ranges. Thus, the phenomenon of the reentrant superconductivity is realized. The study of the direct proximity effect showed that a dimensionless order parameter is induced in the N-metal in the form of an anomalous correlator ,which determines a gap in the spectrum of electron excitations independently of the N-metal effective field.

This field automatically exists when the electron-phonon interaction in this subsystem is taken into account.

The performed numerical calculations for Al showed that the induced energy gap function is significantly smaller than a gap without electron-phonon coupling. It was found that the induced gap first increases and then saturates at high transparency Γ_s values. This means that a further growth in the volume of the superconducting part of the hybrid structure has a small impact on the proximity effect. Also, in the area of the gap Δ_N growth as a function of Γ_s, the FM exchange decreases Δ_N value. The gaps for spin indices $\sigma = 1$ and $\sigma = -1$ differ significantly, that is related to the asymmetric exchange shift of the electron energy bands with corresponding spins. Studied spectral properties of the hybrid structure are in a good agreement with experimental data and also reflect the existence of both coherent and incoherent elementary excitations in certain frequency ranges.

4.6 References to chapter 4

4.1 Kitaev A. Yu. Unpaired Majorana fermions in quantum wires. *Phys.-Usp.* 2001. V. 44. P. s131–s136.

4.2 Gor'kov L. P. On the energy spectrum of superconductors. *Sov. Phys. JETP*. 1958. V. 34. P. 505–508.

4.3 Gennes P. G. Boundary effects in superconductors. *Rev. Mod. Phys.* 1964. V. 36. P. 225–237.

4.4. McMillan W. L. Tunneling model of the superconducting proximity effect. *Phys. Rev.* 1968. V. 175. P. 537–542.

4.5 Eilenberger G. Transformation of Gorkov's equations for type II super-conductors into transport-like. *Z. Phys.* 1968. V. 214. P. 195–213.

4.6 Usadel K. D. Generalized diffusion equation for superconducting alloys. 1970. *Phys. Rev. Lett.* V. 25. P. 507–509.

4.7 Golubov A. A., Kupriyanov M. Yu., Lukichev V. F., Orlikovskiy A. Influence of the proximity effect in the electrodes on the stationary properties of SN-N-NS variable-thickness bridges. *Russ. Microelectron.* 1983. V. 12. P. 355–362.

4.8 Bergeret F. S., Volkov A. F., Efetov K. B. Odd triplet superconductivity and related phenomena in superconductor-ferromagnet structures. *Rev. Mod. Phys.* 2005. V. 77. P. 1321–1373.

4.9 Buzdin A. I. Proximity effects in superconductor-ferromagnet hetero-structures. *Rev. Mod. Phys.* 2005. V. 77. P. 935–975.

4.10 Zdravkov V., Sidorenko A., Obermeier G., Gsell S., Schreck M., Muller C., Horn S., Tidecks R., Tagirov L. R. Reentrant Superconductivity in Nb/Cu$_{1-x}$Ni$_x$ Bilayers. *Phys. Rev. Lett.* 2006. V. 97. P. 057004.

4.11 Zubov E. E., Zhitlukhina E. S. Effective field approach to transition-metal oxide systems: Magnetism, transport and spectral properties. Vasyl' Stus – DonNU: Vinnytsia, 2019.

4.12 Zubov E. E. Nonlinear proximity effect in a hybrid normal metal-super-conductor structure. *IEEE 10th International Conference Nanomaterials: Applications & Properties*. 2020.

4.13. Mahan G. D. Many particle physics. Plenum: New York. 1990.

4.14. Bardeen J. Handbuch der Physik, Springer-Heidelberg. 1956. V. 15. P. 274.

4.15. Meservey R., Schwartz B. B. Equilibrium properties: comparison of experimental results with prediction of the BCS theory. In "Superconductivity". V. I. Ed. Parks R. D. Marcel Dekker: Inc-New York. 1969.

4.16. Guéron S., Pothier H., Birge N. O., Esteve D., Devoret M. H. Superconductivity proximity effect probed on a mesoscopic length scale. *Phys. Rev. Lett.* 1996. V. 77. P. 3025–3028.

4.17. Gladstone G., Jensen M. A. Schrieffer J. R. Superconductivity in the Transition Metals: Theory and Experiment. In "Superconductivity". V. II. Ed. Parks R. D. Marcel Dekker: Inc-New York. 1969.

НОВІ РУБЕЖІ МАТЕРІАЛОЗНАВСТВА: ІННОВАЦІЙНІ КОМПОНЕНТИ ДЛЯ НАСТУПНОГО ПОКОЛІННЯ НАДПРОВІДНИКОВИХ ТЕХНОЛОГІЙ

Монографія

(Англійською мовою)

За загальною редакцією професора М. О. Білоголовського

Технічний редактор О. К. Гомон